Theses and Dissertations

Spring 2011

Iterative reconstruction method for three-dimensional non-Cartesian parallel MRI

Xuguang Jiang
University of Iowa

Recommended Citation

ITERATIVE RECONSTRUCTION METHOD FOR THREE-DIMENSIONAL

NON-CARTESIAN PARALLEL MRI

by

Xuguang Jiang

<u>An Abstract</u>

Of a thesis submitted in partial fulfillment of the
requirements for the Doctor of Philosophy
degree in Electrical and Computer Engineering
in the Graduate College of
The University of Iowa

May 2011

Thesis Supervisor: Professor Gary E Christensen

ABSTRACT

Parallel magnetic resonance imaging (MRI) with non-Cartesian sampling pattern is a promising technique that increases the scan speed using multiple receiver coils with reduced samples. However, reconstruction is challenging due to the increased complexity.

Three reconstruction methods were evaluated: gridding, blocked uniform resampling (BURS) and non-uniform FFT (NUFFT). Computer simulations of parallel reconstruction were performed. Root mean square error (RMSE) of the reconstructed images to the simulated phantom were used as image quality criterion. Gridding method showed best RMSE performance.

Two type of a priori constraints to reduce noise and artifacts were evaluated: edge preserving penalty, which suppresses noise and aliasing artifact in image while preventing over-smoothness, and object support penalty, which reduces background noise amplification. A trust region based step-ratio method that iteratively calculates the penalty coefficient was proposed for the penalty functions. Two methods to alleviate computation burden were evaluated: smaller over sampling ratio, and interpolation coefficient matrix compression. The performance were individually tested using computer simulations. Edge preserving penalty and object support penalty were shown to have consistent improvement on RMSE. The performance of calculated penalty coefficients on the two penalties were close to the best RMSE. Oversampling ratio as low as 1.125 was shown to have impact of less than one percent on RMSE for

the radial sampling pattern reconstruction. The value reduced the three dimensional data requirement to less than 1/5 of what the conventional 2x grid needed. Interpolation matrix compression with compression ratio up to 50 percent showed small impact on RMSE.

The proposed method was validated on 25 MR data set from a GE MR scanner. Six image quality metrics were used to evaluate the performance. RMSE, normalized mutual information (NMI) and joint entropy (JE) relative to a reference image from a separate body coil scan were used to verify the fidelity of reconstruction to the reference. Region of interest (ROI) signal to noise ratio (SNR), two-data SNR and background noise were used to validate the quality of the reconstruction. The proposed method showed higher ROI SNR, two-data SNR, and lower background noise over conventional method with comparable RMSE, NMI and JE to the reference image at reduced computer resource requirement.

Abstract Approved: _____
                    Thesis Supervisor

                    _____
                    Title and Department

                    _____
                    Date

ITERATIVE RECONSTRUCTION METHOD FOR THREE-DIMENSIONAL

NON-CARTESIAN PARALLEL MRI

by

Xuguang Jiang

A thesis submitted in partial fulfillment of the
requirements for the Doctor of Philosophy
degree in Electrical and Computer Engineering
in the Graduate College of
The University of Iowa

May 2011

Thesis Supervisor: Professor Gary E Christensen

Graduate College
The University of Iowa
Iowa City, Iowa

CERTIFICATE OF APPROVAL

PH.D. THESIS

This is to certify that the Ph.D. thesis of

Xuguang Jiang

has been approved by the Examining Committee for the thesis requirement for the Doctor of Philosophy degree in Electrical and Computer Engineering at the May 2011 graduation.

Thesis Committee: _____
Gary E Christensen, Thesis Supervisor

_____
Daniel R Thedens

_____
Steve M Collins

_____
Milan Sonka

_____
Vincent A Magnotta

ACKNOWLEDGEMENTS

ABSTRACT

Parallel magnetic resonance imaging (MRI) with non-Cartesian sampling pattern is a promising technique that increases the scan speed using multiple receiver coils with reduced samples. However, reconstruction is challenging due to the increased complexity.

Three reconstruction methods were evaluated: gridding, blocked uniform resampling (BURS) and non-uniform FFT (NUFFT). Computer simulations of parallel reconstruction were performed. Root mean square error (RMSE) of the reconstructed images to the simulated phantom were used as image quality criterion. Gridding method showed best RMSE performance.

Two type of a priori constraints to reduce noise and artifacts were evaluated: edge preserving penalty, which suppresses noise and aliasing artifact in image while preventing over-smoothness, and object support penalty, which reduces background noise amplification. A trust region based step-ratio method that iteratively calculates the penalty coefficient was proposed for the penalty functions. Two methods to alleviate computation burden were evaluated: smaller over sampling ratio, and interpolation coefficient matrix compression. The performance were individually tested using computer simulations. Edge preserving penalty and object support penalty were shown to have consistent improvement on RMSE. The performance of calculated penalty coefficients on the two penalties were close to the best RMSE. Oversampling ratio as low as 1.125 was shown to have impact of less than one percent on RMSE for

the radial sampling pattern reconstruction. The value reduced the three dimensional data requirement to less than 1/5 of what the conventional 2x grid needed. Interpolation matrix compression with compression ratio up to 50 percent showed small impact on RMSE.

The proposed method was validated on 25 MR data set from a GE MR scanner. Six image quality metrics were used to evaluate the performance. RMSE, normalized mutual information (NMI) and joint entropy (JE) relative to a reference image from a separate body coil scan were used to verify the fidelity of reconstruction to the reference. Region of interest (ROI) signal to noise ratio (SNR), two-data SNR and background noise were used to validate the quality of the reconstruction. The proposed method showed higher ROI SNR, two-data SNR, and lower background noise over conventional method with comparable RMSE, NMI and JE to the reference image at reduced computer resource requirement.

TABLE OF CONTENTS

LIST OF TABLES

Table

LIST OF FIGURES

Figure

CHAPTER 1
INTRODUCTION

Magnetic resonance imaging (MRI) is a kind of tomographic imaging technique that creates images of the internal characteristics of the object from externally measured signals based on nuclear magnetic resonance (NMR). MRI has developed into one of the most popular medical imaging techniques. It has been widely used in imaging of cardiac, brain, spinal cord, and so on.

1.1   Nuclear Magnetic Resonance

NMR phenomenon was first independently observed by Felix Bloch and Edward Purcell in 1946. NMR is based on the fact that a nucleus that has odd atomic weights and/or odd atomic numbers possess an angular momentum, called a spin. A hydrogen atom is one example of this kind of nucleus which has only one proton. The spin creates a magnetic field around the nucleus. Since the direction of the spins are random, the bulk magnetism is zero [1].

If the nuclei are exposed to a strong external magnetic field B_0, with its direction denoted as $\vec{z}$, they will begin to align with B_0, either parallel or antiparallel, and precess around the direction of B_0. The angular frequency ω_0, known as Larmor frequency, of the precession is

$$\omega_0 = \gamma B_0 \tag{1.1}$$

where γ is called gyromagnetic ratio, which is a physical constant for certain nuclei. For example, $\gamma = 2.675 \times 10^8 rad/s/T$ for ^{1}H, $\gamma = 7.075 \times 10^7 rad/s/T$ for ^{31}P. B_0 is typically between 0.2 and 3T in most clinical MRI systems. The number of spins in the two alignments with B_0 are not equal, with a small number more of spins in the parallel alignment mode which corresponds to a low energy state. Thus a bulk macroscopic magnetization $\vec{M}$ is generated, whose direction is exactly along the direction of B_0 at equilibrium. The bulk transverse component is still zero because of the randomness of the spin in this plane [1].

If another oscillating magnetic field $B_1(t)$ with the oscillating frequency the same as Larmor frequency is applied on the transverse plane, some spins in the low energy state will absorb energy and transit to the high energy state. The bulk magnetism will be flipped away from the B_0 direction, creating a non-zero transverse plane component. The angle α between the new direction and B_0 is called the flip angle, which depends on the shape and duration of $B_1(t)$. $B_1(t)$ also has a frequency selectivity property that affects the kind of nuclei spins to be excited. After the RF pulse $B_1(t)$ is over, the nuclear spin system is in the free induction decay (FID) mode. These spins will return to the low energy state follow an exponential function. The behavior of $\vec{M}$ under this circumstance is described by the Bloch equation [1]:

$$\frac{d\vec{M}}{dt} = \gamma \vec{M} \times \vec{B} - \frac{M_x\vec{i} + M_y\vec{j}}{T_2} - \frac{(M_z - M_z^0)\vec{k}}{T_1} \tag{1.2}$$

where M_z^0 is the equilibrium value of M when only B_0 is present.

There are two time constants related to the relaxation: T_1, which relates to the recovery of magnetism along the longitudinal direction of B_0, and T_2, which relates to the diminishing of transverse plane magnetism. This is called relaxation. The bulk magnetism will vary in this period. This means the signal is generated by free precession of the bulk magnetization, it can be detected by a receiver coil based on Faraday's law of electromagnetic induction and the signal strength is decreasing over time [1]. This is the raw signal that the MRI system produce. $B_1(t)$ field is also called RF pulse because it lasts in a short time and oscillates int the radio-frequency range [1].

1.2 Magnetic Resonance Imaging

Paul Lauterbur proposed an spatial information encoding principle so that an image can be generated using the NMR signal in 1972 [2]. A typical MRI system contains three hardware components: a main magnet B_0, a magnet field gradient system G and a RF system $B_1(t)$.

1.2.1 Magnetic Gradient Systems

B_0 and $B_1(t)$ have been discussed in the previous section. The gradient system typically consists of three orthogonal gradient coils to produce time varying magnetic field along $\vec{x}$, $\vec{y}$ and $\vec{z}$ directions. The direction of the gradients are all along $\vec{z}$, only the magnitude varies along different directions. For example, $\vec{G}_x = G_x(x)\vec{z}$. The shapes and forms of these gradients can be adjusted independently to satisfy different requirements. They are essential for signal localization.

With a gradient $\vec{G}$, equation 1.1 becomes

$$\omega_0 = \gamma(B_0 + \vec{G} \cdot \vec{r}) \tag{1.3}$$

where $\vec{r}$ denotes an spatial location. Now the Larmor frequency at different spatial locations are different.

1.2.2 Signal Encoding

The gradient systems have two main functions: slice selection and spatial encoding. Slice selection is the result of both the gradients, which make the Larmor frequency depend on spatial location, and RF pulse, which has a frequency selection function.

The spatial information encoding can be done in two ways: frequency encoding, which makes the oscillation frequency of the MR signal linearly dependent on spatial location, and phase encoding, which makes the initial phase of the MR signal linearly dependent on location. For example, if $\vec{G}_{fe} = [G_x G_y G_z]$ is applied, the Larmor frequency with respect to position $\vec{r} = [r_x r_y r_z]$ is

$$\omega(\vec{r}) = \omega_0 + \gamma \vec{G}_{fe} \cdot \vec{r} \tag{1.4}$$

where $[\cdot]$ denotes inner produce. The received signal is

$$S(t) = \left[\int_{object} \rho(\vec{r}) e^{-i\gamma \vec{G}_{fe} \cdot \vec{r} t} d\vec{r} \right] e^{-i\omega_0 t} \tag{1.5}$$

where $\rho(\vec{r})$ is the spin density at position $\vec{r}$ [1]. After signal demodulation (this is done in signal detection), the signal becomes

$$S(t) = \int_{object} \rho(\vec{r}) e^{-i\gamma \vec{G}_{fe} \cdot \vec{r} t} d\vec{r} \tag{1.6}$$

For phase encoding, $\vec{G}_{pe}$ is turned on for a short interval T_{pe} and then turned off. The signal is

$$S(t) = \int_{object} \rho(\vec{r}) e^{-i\gamma \vec{G}_{pe} \cdot \vec{r} T_{pe}} d\vec{r} \tag{1.7}$$

The signal expression can be simplified using the popular k-space notation. k-space is the spatial-frequency domain. The parameters are defined as follows [1]:

$$k_x = \gamma G_x t \tag{1.8}$$

$$k_y = \gamma G_y t \tag{1.9}$$

$$k_z = \gamma G_z t \tag{1.10}$$

or in the general expression:

$$k = \gamma \int_0^t G(\tau)d\tau \tag{1.11}$$

where k represents the location in k-space. Figure 1.1 illustrates some examples of the relationship of G and k.

(a) G_x and G_y.   (b) k_x and k_y.
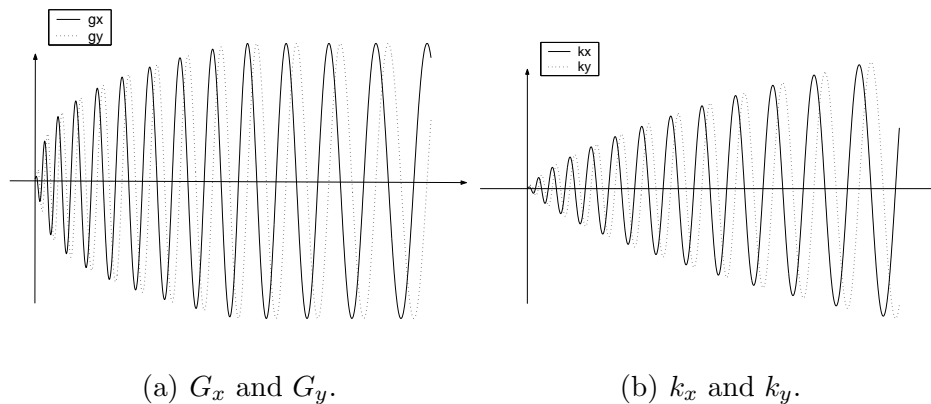
Figure 1.1: Gradient and k-space locations.

In this way, the frequency encoded signal is

$$S(\vec{k}) = \int_{object} \rho(\vec{r})e^{-i\vec{k}\cdot\vec{r}}d\vec{r} \tag{1.12}$$

Equation 1.12 is exactly the same form as the Fourier transformation of $\rho(\vec{r})$ [1]. This means the spatial domain and the k-space are a Fourier transformations pair. This property is very useful in image reconstruction from k-space samples. An example of

two dimensional image and its k-space samples are illustrated in figure 1.2.
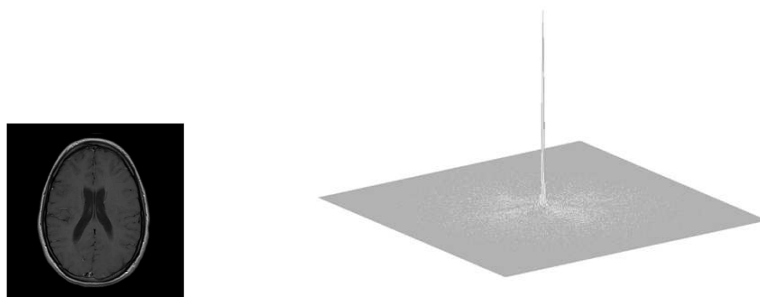
(a) 2D image.   (b) 2D k-space samples.

Figure 1.2: Two dimensional image and k-space samples.

1.2.3   Signal Detection

Signal detection starts after the RF pulse $B_1(t)$ is over. If the magnetic field is homogeneous, the FID signal can provide enough information to form the detected signal. However, the homogeneousness is not always true. The FID signal decays much faster in the inhomogeneous magnetic field. To overcome this fast decay problem, a new MR signal called echo is used. There are two ways to generate this echo signal. One is to used multiple RF pulses. The signal is called RF echoes or spin echoes. The other is to used magnetic gradients. The signal is called gradient echoes [1].

1.2.4 Fast Imaging Techniques

With the development of MRI systems, the scan speed is increased by varies fast imaging techniques. These methods include fast spin echo (FSE) [3–5], fast gradient echo such as fast low angle shot (FLASH) [6].

Echo-planar imaging (EPI) is the first ultra high speed imaging method [7]. This method can collect a complete set of two dimensional k-space data by one RF pulse. Later this term is broadened to refer to single-shot imaging. Multi-shot EPI is also included in this term. The k-space data lie in a zig-zag trajectory, as illustrated in Figure 1.3(a).

Some other trajectories are also used in EPI, such as rectilinear trajectory [8], spiral [9, 10], etc. shown in Figure 1.3(b) and 1.3(c), respectively. Spiral trajectory has been widely used due to its intrinsic advantages. Its sampling trajectory always starts at the k-space origin. This means the strongest signal is obtained. It also has a moment-nulling motion compensation property, reducing artifacts caused by patient motion. Besides, it can efficiently use the power of the gradient system [10, 11]. A drawback of spiral trajectory imaging, and also the non-Cartesian grid imaging, is the need of an extra regridding step. Details will be discussed in later chapters.

Partial k-space sampling is another kind of method. The speed is enhanced by reducing the number of scanned samples. The missing samples are restored later by estimation. Two main problems are related with these methods: loss of resolution and introduction of extra artifacts [1].

Parallel imaging, or multi-coil imaging, is a promising fast imaging method

(a) Zigzag   (b) Rectilinear   (c) Spiral
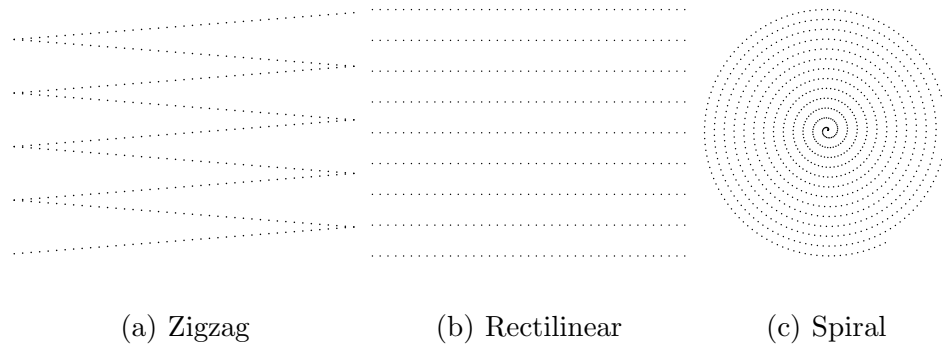
Figure 1.3: k-space trajectories.

which was proposed recently [12, 13]. It utilizes a number of receiver coils to sample k-space. The sampling trajectory can be any of those used in previous fast imaging ones. But there is additional information resides in the non-uniform coil sensitivity. Each coil obtains a reduced number of frequency encoded samples. The image can then be obtained using both frequency encoding and the coil sensitivity information.

1.2.5   Image Reconstruction

The measured signal from MRI scanner need to be postprocessed, or reconstructed, to convert to an image.

If the k-space samples are equally spaced, the reconstruction is simply an inverse Fourier operation. This can be efficiently computed via Fast Fourier Transformation (FFT). A parameter called the field of view, or FOV, which represents the largest object that can be reconstructed without aliasing, is defined by the distance Δk between the lines in k-space:

$$FOV = \frac{1}{\Delta k} \qquad (1.13)$$

In fast imaging situations, a more complicated reconstruction technique need to be implemented. For non-Cartesian samples, an interpolation step need to be performed before FFT to convert the samples onto a regular Cartesian grid. Several methods have been proposed, such as gridding [10, 14, 15], nonuniform FFT (NUFFT) [16–19], blocked uniform resampling (BURS) [20], etc. These methods will be discussed in detail in later chapters.

In parallel imaging, the reconstruction is even more complicated and involves an extra step of combining the coil sensitivity information with the usual spatial encoding information. Two popular parallel imaging methods are SiMultaneous Acquisition of Spatial Harmonics (SMASH), which utilizes coil sensitivity information in k-space, and SENSitivity Encoding (SENSE) which derives a sensitivity map in the image domain [12, 13].

The specific aims of this work are:

1. Evaluate MRI image reconstruction methods from non-Cartesian k-space samples. Compare the similarities and differences of the methods.

2. Apply the reconstruction methods in parallel imaging strategies in MRI. Compare their performances.

3. Develop an efficient three-dimensional parallel MRI image reconstruction algorithm from non-Cartesian samples.

4. Evaluate the performance of the new method using 3D simulations and *in vivo* MR data.

The rest of the chapters are arranged as follows. In chapter 2 several reconstruction method from non-Cartesian samples are reviewed. The application of non-Cartesian method with parallel MRI reconstruction are evaluated in chapter 3. Methods for image qualify improvement and computation burden alleviation are proposed and evaluated using computer simulations in chapter 4. In chapter 5 the proposed method are evaluated using three-dimensional non-Cartesian data from MR scanner. Several image quality metrics are calculated and compared with conventional method. Chapter 6 summarizes this thesis.

CHAPTER 2
MRI IMAGE RECONSTRUCTION

For non-Cartesian k-space samples, FFT cannot be directly applied to reconstruct the image. Discrete Fourier transformation is a possible method with a much heavier computation burden. Currently the widely used method is to first regrid the samples onto regular Cartesian grid and then apply inverse FFT. These methods include gridding [10, 14, 15], blocked uniform resampling (BURS) [20, 21], non-uniform FFT (NUFFT) [16–19], etc.

2.1   Gridding Reconstruction Algorithm

The most general and currently widely used method of reconstruction in MRI is the gridding reconstruction algorithm [10, 14, 15]. Gridding is an interpolation operation from non-Cartesian samples onto grid points. As illustrated in figure 2.1, all the non-Cartesian points in a certain distance (window width) Δ interpolate on the Cartesian grid point in the center. It generally contains four steps.

- The first step is to perform density compensation to compensate for the non-uniformity of the k-space sample points.

- The samples are convolved with an interpolation kernel and resampled onto Cartesian grid.

- Image is obtained by an inverse FFT.
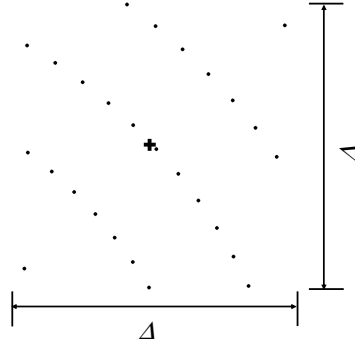
Figure 2.1: Gridding interpolation. The "+" denotes a Cartesian grid point which value is unknown. The "·" represent the surrounding non-Cartesian samples which contribute to the interpolation on "+". Δ is the width of the convolution kernel.

- Divide the image by the inverse Fourier transformation of the interpolation kernel to compensate for the roll-off effect of its main lobe.

This process is illustrated in Fig. 2.2 [15].
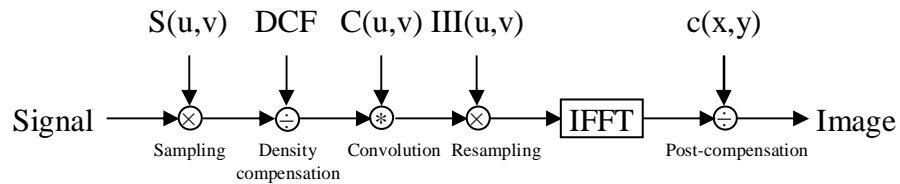
Figure 2.2: Gridding method

The expression of image x is shown in equation 2.1

$$x = F^{-1}((\frac{S}{D} * C) \cdot III) \cdot \frac{1}{c} \tag{2.1}$$

where S is k-space samples, D is density compensation, C is the convolution kernel in k-space, "*" denotes convolution operation, III represents Cartesian grid resampling, c is post-compensation, F^{-1} represents inverse FFT.

In the first step, the nonuniform sampling density is usually corrected by a density compensation function, or DCF. The DCF can be defined and computed in a variety of ways. This step is important in reducing the reconstruction error in the image. Jackson *et al.* introduced a numerical method called the area density function, or ADF, as density compensation [15]. An iterative method which extends the ADF was provided by Pipe *et al.* [22]. Meyer *et al.* introduced an analytic function as the DCF for spiral sampling trajectory [10]. Hoge *et al.* described another analytic DCF for spiral trajectory which is based on the Jacobian determinant for the transformation between the Cartesian grid and the spiral trajectory parameters of time and interleaf rotation angle [23]. Rasche *et al.* proposed a Voronoi-diagram method to compute DCF [24]. The DCF is the inverse of the area of the Voronoi cell around each sample. An example of Voronoi-diagram for 2D spiral trajectory is shown in figure 2.3. The Voronoi-diagram approach is a powerful method to compute the local density. It can be used on both 2D and 3d problems. The result depends only on the sampling pattern, not on the acquiring order. The drawback is that its computation complexity is relatively high. And since the computation of the Voronoi cell requires the existence of neighboring points, there may be problems when dealing with the points at the outmost of the sampling area. These points need to be treated with additional assumptions and computations besides the Voronoi-diagram.
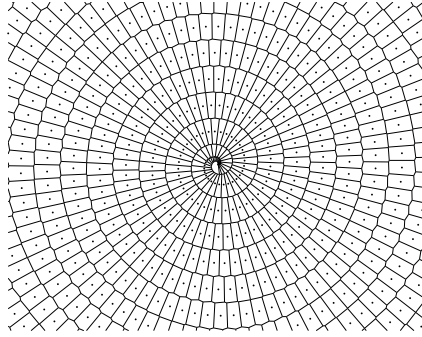
Figure 2.3: Example of Voronoi-diagram

O'Sullivan analyzed the gridding operation and showed that the optimal gridding method is to first convolve with an infinite *sinc* function and then perform resampling [14]. For practice reasons, this infinite function need to be replaced by a finite convolving function. This finite convolution kernel will contribute two artifact into the reconstructed image. Firstly, the inverse of the Fourier transform of this kernel has side lobes, which will be aliased back to the image causing artifact. Also, the central lobe is typically not flat. It shows a rolloff effect. Thus the intensity of the image is changed. This can be corrected by a post-compensation step, which requires dividing the image by this central lobe. Jackson *et al.* compared the performance of several kinds of kernels including two-term cosine (Hamming window, Hanning windows), three-term cosine (Blackman window), Gaussian window and Kaiser-Bessel kernel, and concluded that in the sense of minimum aliasing energy in the reconstructed image, Kaiser-Bessel kernel with optimal parameter is the best choice [15].

To reduce the artifact in the reconstructed image, an over-sampling ratio is applied to the reconstruction. Gridding is usually applied on a larger (denser) grid

in k-space, and then keep only the center region of the image after inverse FFT [15, 20, 25]. Typically a double sized (2x) grid, which corresponds to over-sampling ratio of 2, is used. Using larger grid generates a better image with the cost of computation time. A recent research showed that smaller values of 1.125x or 1.375x grid are also possible with comparable image errors [26].

Gridding is widely used due to its simpleness and easiness to implement. The kernel width is typically small, 2-4 according to Jackson *et al.* [15], making it still a fast algorithm to implement. However, one drawback of the gridding method is the definition and computation of the density compensation. This is typically a time-consuming part.

2.2   Blocked Uniform Resampling

Rosenfeld introduced the Uniform ReSampling (URS) algorithm to solve the regridding problem [20]. URS constructs a set of linear equations based on interpolations from Cartesian grid to non-Cartesian k-space samples. Then the equations are solved using singular value decomposition (SVD). A more computationally feasible version called Blocked URS (BURS) was also provided [20]. Similar algorithms was also proposed by Kadah [27].

According to sampling theory [28], an interpolation from regular Cartesian grid points k to any point κ can be expressed as

$$f(\kappa) = \sum_{n=-\infty}^{\infty} f(k_n) K(\kappa - k_n) \qquad (2.2)$$

where $K(\cdot)$ is the interpolation kernel, which is the *sinc* function for the ideal case.

The relationship between the values on the Cartesian grid y and those on the sampling trajectory b can be expressed in a matrix form as

$$Ay = b \tag{2.3}$$

where

$$y = (y_1, y_2, \cdots, y_N)^T, \; b = (b_1, b_2, \cdots, b_M)^T \tag{2.4}$$

y and b are vectors with length N and M respectively. "T" denotes transpose operation. A is the interpolation coefficient matrix with dimension of M-by-N. Its element a_{ji} on the j-th row and i-th column is defined according to equation 2.2

$$a_{ji} = K(\kappa_j - k_i) \tag{2.5}$$

Equation 2.3 is then solved using pseudoinverse of A in the minimum norm least square sense given by

$$
\begin{aligned}
y &= (A^H A)^{-1} A^H b \\
&= A^\dagger b
\end{aligned}
\tag{2.6}
$$

where $A^\dagger = (A^H A)^{-1} A^H$ is the Moore-Penrose pseudoinverse. A^H denotes the complex conjugate transpose of A. The pseudoinverse can be computed efficiently using the singular value decomposition (SVD) [29].

For an $M \times N$ matrix A with rank r, there exists orthogonal $M \times M$ matrix U and $N \times N$ matrix V and a diagonal matrix Σ satisfy the following equation

$$A = U\Sigma V^T \tag{2.7}$$

where $\Sigma = diag(\sigma_1, \sigma_2, \ldots, \sigma_n)$ with $\sigma_1 \geq \sigma_2 \geq \cdots \geq \sigma_r > 0, r \leq n$. The numbers σ_i are the singular values of A. The columns of matrix U and V are the left and right singular vectors of A, respectively. The pseudoinverse of A can then be expressed as

$$A^\dagger = V\Sigma^\dagger U^T \qquad (2.8)$$

where $\Sigma^\dagger$ is a zero matrix except the first r main diagonal elements are $\sigma_1^{-1}, \sigma_2^{-1}, \cdots, \sigma_r^{-1}$.

The solution y minimizes the cost function

$$\psi(y) = ||Ay - b|| \qquad (2.9)$$

and whose norm is the minimum of all that minimize equation 2.9.

A typical size of a two dimension image is 256×256. The number of k-space samples is of the same magnitude. So the dimension of matrix A will be $2^{16} \times 2^{16}$, i.e. the total number of elements in A is around 4×10^9. This makes the SVD computation practically infeasible.

For interpolation problems, a sample that is far away from the point to be interpolated has little impact on the interpolation result. This can also be seen from the definition that $sinc(x) = \sin(x)/x$, which means the interpolation effect decreases with the distance following an envelope function of $\pm 1/x$. The griding algorithm uses this property to limit the width of interpolation kernel [15]. Thus only limited values around the point are used. Similarly, the number of non-zero interpolation kernel coefficients in URS method can be limited. For each k-space sample point, the interpolation is limited to those Cartesian grid within a certain radius of distance. For a Cartesian grid point k_i, only those Cartesian points with a radius of Δk and

k-space sample points with a radius of $\delta\kappa$ are considered. Suppose the number of these points are N_i and M_i respectively. It is sufficient to use these N_i Cartesian points vector $\overline{y}$ and M_i sample points vector $\overline{b}$ to estimate the value at k_i using the following equation

$$\overline{A}\,\overline{y} = \overline{b} \tag{2.10}$$

where $\overline{A}$ is an $M_i \times N_i$ interpolation coefficient matrix. It is a submatrix of the full interpolation coefficient matrix A as in equation 2.3. But now the dimension of the problem to be solved is only $M_i \times N_i$, which is much smaller than $M \times N$. So the pseudoinverse computation is feasible. This is called the Blocked Uniform ReSampling algorithm, or BURS. In summary, the BURS algorithm for 2D image reconstruction is [20]

1. Choose the radii Δk and $\delta\kappa$ (with $\delta\kappa \leq \Delta k$).

2. Initialize a zero $N \times M$ matrix $A^\dagger$.

3. For every Cartesian grid point $k_i (i = 1, 2, ..., N)$ perform the following operation:

   (a) Select M_i non-uniform samples $\overline{b}$ within distance $\delta\kappa$ of k_i.

   (b) Select N_i Cartesian grid points $\overline{x}$ within distance Δk of the k_i.

   (c) Calculate the $M_i \times N_i$ interpolation matrix $\overline{A}$.

   (d) Compute $\overline{A}^\dagger$ using SVD.

(e) Isolate the row in $\overline{A}^\dagger$ corresponding to the position of k_i and save them in the appropriate positions in $A^\dagger$.

4. The values on the Cartesian grid points are obtained by $y = A^\dagger b$.

5. Perform inverse Fourier transformation of y, which can be efficiently calculated with FFT, to generate the reconstructed image.

6. Perform post-compensation.

The Δk and $\delta\kappa$ are two free parameters that will affect the reconstructed image and also the computation complexity. Larger Δk and $\delta\kappa$ can reconstruct a better image, but the computation time will also be increased [20].

A possible improvement on the computation burden in BURS is to divide the Cartesian grids into many small blocks with block size $B \geq 1$. Then in the above algorithm, the computation for every Cartesian grid points is replaced by computation for every block [30].

In general, BURS can produce similar or better images compared with the gridding algorithm [21]. Several applications of BURS showed that it is an accurate algorithm, but the reconstruction is also sensitive to noise and measuring errors [21, 25, 31]. As a result, the reconstructed image may be contaminated even the noise level is not high [21, 25]. The reason of noise amplification lies in the pseudoinverse of the interpolation matrix. It is an inverse problem whose result is often unstable. In equation 2.8, the reverse of the singular values σ_i^{-1} are involved in the pseudoinverse. A small σ_i corresponds to a very large σ_i^{-1}. This means an arbitrarily

small perturbation of the input data can cause an arbitrarily large perturbation in the image.

The solution of this problem is to add some kind of regularization, i.e. incorporate further information of the desired solution to stabilize the problem and single out the desired stable one. Several types of regularization techniques can be applied. The main part of which is to replace σ_i^{-1} with a filter function $F(\sigma_i)$ such that $F(\sigma_i) \approx \sigma_i^{-1}$ for larger σ_i and $F(\sigma_i) \approx 0$ for small σ_i.

The most famous method is the Tikhonov regularization [32, 33], where

$$F(\sigma_i) = \frac{\sigma_i}{\sigma_i^2 + \mu} \tag{2.11}$$

μ is the regularization parameter to be determined based on the specific problem. Another popular method is the truncated SVD (TSVD) [29, 34], where

$$F(\sigma_i) = \begin{cases} \sigma_i^{-1} & 1 \leq i \leq \mu \\ 0 & \text{other} \end{cases} \tag{2.12}$$

μ is the position to truncate the singular values.

These regularization techniques successfully improved the BURS reconstruction with noisy data [21, 25]. At the same time, the computation complexity does not change too much. But how to obtain the optimal regularization parameter still remains to be an open problem. In practice empirical values are typically used [21, 25].

2.3 Non-Uniform FFT

Reconstruction Algorithm

Non-uniform FFT, or NUFFT, is a method to approximating the Fourier trans-formation from image to non-uniform (non-Cartesian) k-space samples by interpolat-ing an oversampled FFT [16–19].

Suppose $x_n, n = 1, 2, \ldots, N - 1$ is an equally spaced 1D signal sequence. The Fourier transformation of x_n, $X(\omega)$ is given by

$$X(\omega) = \sum_{n=0}^{N-1} x_n e^{-i\omega n} \tag{2.13}$$

This computation can be efficiently obtained by FFT if $X(\omega)$ is also equally spaced. For a collection of M non-uniformly spaced frequency locations $\{\omega_m\}$, the Fourier transformation is defined as

$$X_m = \sum_{n=0}^{N-1} x_n e^{-i\omega_m n} \tag{2.14}$$

Directly evaluating equation 2.14 requires $O(MN)$ operations. This would be con-siderably slow when M and N are large (as in most imaging applications). Fast computation of equation 2.14 generally contains two steps [19]. The first step is to choose a number $K \geq N$ and compute a weighted K-point FFT over $\{x_n\}$:

$$Y_k = \sum_{n=0}^{N-1} s_n x_n e^{-i\frac{2\pi}{K}kn} \tag{2.15}$$

where $\{s_n\}$ is a scaling vector, which is an algorithm design parameter to pre-compensate for imperfections in the following frequency domain interpolation [18]. This is similar to the post-compensation operation in the gridding method. The second step is to approximate $\{X_m\}$ by interpolation using some neighbor points in

$\{Y_k\}$.

$$\hat{X}(\omega_m) = \sum_{k=0}^{K-1} Y_k v_{mk}^H \qquad (2.16)$$

where v_{mk} denotes the interpolation coefficients.

The are many ways to choose the interpolation function, which controls the scaling parameter s_n and interpolation coefficients v_{mk}. Dutt *et al.* [16] introduced a Gaussian based interpolation. Starty *et al.* [35] proposed a generalized FFT (GFFT) and demonstrated that a Gaussian kernel can provide a more accurate reconstruction compared to the Kaiser-Bessel based griding method. Beylkin [36] used the B-spline based interpolation. Anderson *et al.* [37] took the Taylor series expansion method. Fessler *et al.* [19] introduced a min-max interpolation, which is a fixed-width interpolator that minimizes the worst case approximation error of all signals with unit norm. Sha *et al.* [38] used a similar criterion by using a kernel matrix that fit for the k-space trajectory in the sense of least square approximation error. The performance of the NUFFT method with min-max interpolation was shown to be more accurate than other interpolation methods [19].

The image x and k-space samples b can be related using a general form as

$$b = Ex + n = AFx + n \qquad (2.17)$$

where $E = AF$ is an encoding matrix that maps x onto b, F denotes FFT, A is an interpolation matrix similar to that in BURS method, and n is white Gaussian noise. In MRI with non-Cartesian samples, E is the NUFFT operation of x. Conjugate gradient method (CGM) is a popular iterative method to solve equation 2.17 in the

least square sense [39, 40]. Its objective function is

$$\psi(x) = ||Ex - b||^2 \tag{2.18}$$

Among all the possible solutions, CGM chooses the one with minimal norm [39].

There are several user defined parameters in CGM. Firstly, an initial estimation of x need to be provided as a starting value in CGM. All possible estimations, such as prior information or a rough reconstruction, can be used. It can also be set to zero in the simplest situation. A good starting value can speed up the convergence of CGM. Another parameter is the total number of iterations. In theory, if the dimension of E is $N \times N$, then the maximum iteration for the solution to converge is N [39]. However, in practice x can converge to a fairly good result in a small number of iterations, with only minor improvements from then on. So there is a trade-off between the solution quality and the computation time. Typically the number of iterations can be set to a number much smaller than N.

In conventional gridding reconstruction method, the operation is on k-space samples and evenly-spaced k-space grid points. While in iterative NUFFT reconstruction, the manipulation is done directly between the image and the k-space samples. Thus it is easy to incorporate regularizations based on image processing techniques such as smoothing, edge-preserving, etc. [40]

The iterative reconstruction method using NUFFT yields a better image compared to gridding [19]. The image artifacts are greatly reduced. The incorporation of edge-preserving regularization further enhances the image quality. On the other hand, however, the iterative reconstruction method requires longer computation time

compared with gridding.

2.4 Relationships of Gridding,

BURS and NUFFT

BURS, which is a least square algorithm, and gridding method are derived in two different approaches. But they are the closely related [20,31].

The gridding operation is a method to interpolate the grid data based on the non-equally spaced samples. The k-space operation includes a density compensation, convolution and resampling. This can be expressed as

$$\hat{f}(k_j) = \sum_{i=1}^{M} K(k_j - \kappa_i) f(\kappa_i) d(\kappa_i) \tag{2.19}$$

where $f(\kappa_i)$ denotes the value at the i-th sample point κ_i, $d(\kappa_i)$ represents the density compensation at κ_i, $K(\cdot)$ denotes the convolution kernel, M is the total number of samples and $\hat{f}(k_j)$ is the estimated value at the j-th Cartesian grid point k_j. Let $x = [\hat{f}(k_j)]$ denote the $N \times 1$ vector of grid points and $b = [f(\kappa_i)]$ denote the $M \times 1$ sample vector, equation 2.19 can be rewrite as

$$y = A^H D b \tag{2.20}$$

where A is the $N \times M$ coefficient matrix with its element $A_{ij} = K(k_j - \kappa_i)$. Since all A_{ij}s are real-valued, $A^H = A^T$. D is an $M \times M$ diagonal matrix with its main diagonal value $D_{ii} = d(\kappa_i)$. To make a similar form, equation 2.6 in BURS can be rewrite as [31]

$$\begin{aligned} y &= A^H A (A^H A)^{-2} A^H b \\ &= A^H \left[A (A^H A)^{-2} A^H \right] b \end{aligned} \tag{2.21}$$

Obviously equation 2.20 and 2.21 have a very similar form. The matrices manipulation $A(A^H A)^{-2} A^H$ in BURS in equation 2.21 is approximated by the density function D in gridding in equation 2.20 [31]. One can consider that gridding is a special form of the least square method. Since there is no matrix inversion in gridding, it is more stable compared with BURS.

Gridding and BURS operations are in k-space only. The entire reconstruction process contains an "interpolation" step followed by inverse FFT. NUFFT reconstruction directly relates the image and the k-space samples, making the Fourier transformation an embedded step. The reconstruction procedure is a loop of FFT, interpolation and image updating.

The total number of multiplications in gridding is JM, where M is the total number of k-space samples and $J = J_x \times J_y \times J_z$ is the product of the interpolation kernel size along all directions. The density compensation requires extra computations. In BURS, if $\Delta k_i = \delta \kappa_i = J_i$ for $i = x, y, z$ and assuming $\bar{N}_i = \bar{M}_i$ for every grid point i, then the total number of multiplications is around JM after SVD is done. In NUFFT, the total number of operations is $O(nK \log K) + O(nJM)$ [19], where K is the larger grid size, n is the number of iterations. Typically $K \approx 2N, J \leq 10$ and $M \approx N$ [19].

In all the methods there are some coefficients or intermediate results that can be pre-computed. In gridding, the DCF is typically pre-computed, the memory requirement is only M. The interpolation coefficients, i.e. the A matrix in equation 2.20 can also be precomputed. But this is not always required because the computation

burden is not high. In BURS, the SVD requires $O(\bar{N}^3)$ operations, where $\bar{N} = J$ is the dimension of each of the small matrix $\bar{A}$. The SVD result $A^\dagger$ can be pre-computed, which requires total memory of around JM. In NUFFT since iterative method is used, the image needs to be computed several times for the same k-space locations. It is convenient to pre-compute and store all the interpolation coefficients to save computation time. The total number of these coefficients is also JM. The comparison of gridding, BURS and NUFFT are summarized in table 2.1.

	gridding	BURS	NUFFT
number of operations	JM	JM	$O(nK \log K) + O(nJM)$
memory requirement	M or $M + JM$	JM	JM

Table 2.1: Comparison of gridding, URS and NUFFT.

CHAPTER 3
PARALLEL IMAGING RECONSTRUCTION

3.1 Parallel Imaging

Parallel imaging uses an array of receiver coils (for example, a four channel phased array coil) to increase the sampling speed [12, 13]. Each of the coils in the array has a different spatial sensitivity profile. These sensitivities contain spatial encoding information, which is different from the information in k-space locations. The sensitivities are not the property of the object under examination, but of the array coils. This additional information can be used for image generation, thus reducing the k-space location encoding is possible. This will in turn reduce the total scan time.

Currently there are two popular reconstruction methods for parallel imaging that utilize the coil sensitivity information in k-space and image domain respectively. One is SMASH, which is the short for SiMultaneous Acquisition of Spatial Harmonics [12]. It is the first successful in vivo parallel MRI implementation. The other is SENSE, which means SENSitivity Encoding [13]. Many optimizations, extensions and applications of these methods were reported later on.

3.2 SMASH and SENSE

3.2.1 SMASH

3.2.1.1 Theory of SMASH

SMASH is first applied on Cartesian sampling trajectories. It uses linear combinations of simultaneously acquired signals from different coils with different

sensitivity profiles to generate other data points at different k-space locations. This means some data lines can be omitted at the time of scanning and can be recovered later using the coil sensitivity information.

Using 2D imaging as an example, the MR signal at k-space position (k_x, k_y) can be expressed as

$$S(k_x, k_y) = \iint C(x, y)\rho(x, y)e^{-ik_x x - ik_y y} dx dy \tag{3.1}$$

where $\rho(x, y)$ is spin density, $C(x, y)$ is receiver coil sensitivity.

SMASH uses a linear array of surface coils to synthesize multiple sinusoidal sensitivities [12]. For an array of N_c coils, the composite sensitivity needs to be the following form:

$$C^{comp}(x, y) = \sum_j^{N_c} n_j C_j(x, y) = e^{im\Delta k_y y} \tag{3.2}$$

where n_j is the weight for coil j, m is an integer and $\Delta k_y = 2\pi/FOV$. The composite sensitivities are arranged to be spatial harmonics of the image field of view [12]. The effect of the composite sensitivity is to shift the k-space data by $-m\Delta k_y$.

$$
\begin{aligned}
S(k_x, k_y) &= \iint C^{comp}(x, y)\rho(x, y)e^{-ik_x x - ik_y y} dx dy \\
&= \iint \rho(x, y)e^{-ik_x x - i(k_y - m\Delta k_y)y} dx dy \\
&= S(k_x, k_y - m\Delta k_y) \tag{3.3}
\end{aligned}
$$

The imaging speed of SMASH is faster than conventional sequential imaging sequences. If M spatial harmonics can be generated using linear combination, the full k-space signal can then be generated with only a fraction of $1/M$ of the phase encoding steps. Thus the scanning time is reduced by a factor of $1/M$. A factor of

two times savings was implemented in ref.[12] using three and four element array coils for phantom and in vivo images.

Reconstruction of SMASH imaging includes two parts, the computation of coil sensitivities and weighted sums. If the coil sensitivity information is known in advance, then the SMASH reconstruction only consists of several weighted sums followed by inverse FFT. Thus additional reconstruction burden is small. In fact the weighted sum could even possibly be done at the same time of scanning. A correct SMASH image depends on correct measurement coil sensitivities. Errors in sensitivities lead to errors in spatial harmonics. This in turn leads to aliasing artifacts [12]. The aliasing may be avoided by using larger coil arrays. The results in ref.[12] showed that SMASH reconstruction does not sacrifice signal to noise ratio compared with the reference image generated using a sum-of-squares combination of coils.

SMASH has some restrictions in choosing the image planes due to the placement and the direction of the receiver coils. In its original form, a very structured array of coils is required [12]. The requirement of measuring the component coil sensitivities may be another time and computation burden.

There are many improved and extended methods based on SMASH. Such as AUTO-SMASH [41] and variable-density (VD)-AUTO-SMASH [42] which use additional autocalibration signals (ACS) to determine the weights in SMASH automatically. The advantage is that no extra coil sensitivities need to be acquired.

3.2.1.2 GRAPPA

Griswold *et al.* proposed a further extension named GeneRalized Autocal-ibrating Partially Parallel Acquisitions (GRAPPA) [43]. It extends the fitting by using data from multiple lines from all coils to fit an ACS line in a single coil. Better quality and higher SNR images can be obtained [43]. Non-Cartesian k-space samples such as spiral was also used with GRAPPA [44]. The missing spirals are estimated using the weighed averages of the neighbor points in a similar way as in Cartesian GRAPPA.

3.2.2   SENSE

Compared with SMASH, SENSE makes no assumptions on the coil configu-ration and k-space sampling pattern (recent GRAPPA method also eliminates this limit [44]). The method was applied to Cartesian k-space samples when it was first proposed [13]. Later it was generalized to arbitrary k-space trajectories [45].

3.2.2.1   SENSE with Cartesian Samples

In two dimensional Fourier image, SENSE reduces the total sampling time by reducing the number of phase encoding steps. This is achieved by increase the dis-tance between two phase encoding lines while maintain the same maximum k-space value. The factor that describes the reduced number of k-space samples compared to the fully sampled on is referred to as reduction factor R [13]. In standard Fourier imaging, reducing the k-space sampling density will cause a reduced FOV and thus alias artifact in image domain. This aliasing cannot be undone in that case. SENSE

made the recovering from the aliased image possible by incorporating the coil sensitivity information.

SENSE reconstruction includes two steps. Firstly, a reduced-FOV image is created for each of the array coils. When the k-space is sampled on the Cartesian grid, the aliasing artifact is simply the superposition of the parts of the image that fall out of the reduced FOV. The second step is to undo the fold-over effect to create a full-FOV image. Figure 3.1 shows the flow of these steps. The key lies in the non-uniform-valued coil sensitivity maps. For each single coil image, the superposition is the sum of different weighted pixel values. For a specific pixel in the reduced-FOV image, let n_p be the number of pixels in the full-FOV image superposed at that position. Then the values of the n_p corresponding full-FOV image pixels superposed at that position v can be recovered by

$$v = Ua \tag{3.4}$$

where a is a length n_c vector, with n_c the number of coils, containing the complex pixel values in the reduced-FOV images. U is an $n_p \times n_c$ matrix called the unfolding matrix [13].

$$U = (S^H S)^{-1} S^H \tag{3.5}$$

where S is a $n_c \times n_p$ sensitivity matrix. There is a noise term in the expression of U, but it is typically very small such that is always omitted [13]. The elements in S is expressed as

$$S_{\gamma,\rho} = s_\gamma(r_\rho). \tag{3.6}$$
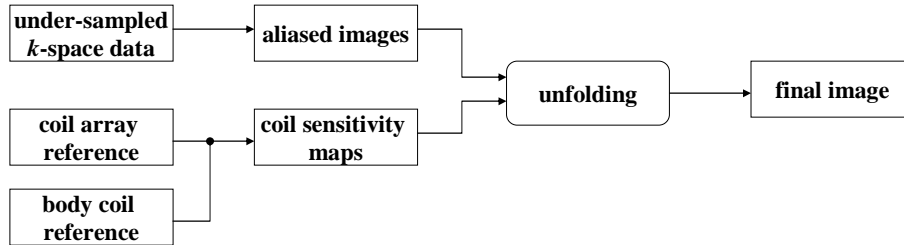
Figure 3.1: SENSE reconstruction.

where s_γ is the sensitivity of coil γ and r_ρ is the position of th pixel ρ.

Solving equation 3.4 requires $n_p \leq n_c$, i.e. the reduction factor is bounded by the number of coils [13]. Solving for each pixel in the reduced-FOV image, a full-FOV image can be obtained. The entire procedure is illustrated in figure 3.1.

SENSE can be generalized to 3D MRI, where aliasing in two phase-encoding dimensions are obtained. This is referred as 2D SENSE [46]. The total reduction factor is the product of the two reduction factors in those two dimension.

3.2.2.2 Coil Sensitivity Map

In SENSE, coil sensitivity map is often obtained from reference scans. Since the purpose of SENSE is to reduce the sampling time, these reference scans should be low resolution acquisitions such that the scan time of these data will not affect the total sampling time. Pruessmann *et al.* proposed a standard method, which is based on interpolation and extrapolation (polynomial fitting and region growing) of the raw maps obtained by division of the thresholded reference images from surface coil and body coil [13].

There are other methods to compute sensitivity map such as using adaptive matched filter [47] and wavelet smoothing [48]. Auto-calibration is also possible by extracting sensitivity information from the densely sampled k-space center [49].

The sensitivity maps have smooth, slow varying profile. With adequate smoothing during computation, the error in sensitivity maps is typically negligible [13].

3.2.2.3 Non-Cartesian Samples

As mentioned in the previous chapters, non-Cartesian sampling patterns such as spiral has many advantages over Cartesian samples. However, extending the SENSE method into non-Cartesian trajectories is not straight forward. Spiral trajectory, for example, generates continuous, ring-shaped aliasing artifact rather than simple superposition. This makes it unusable to apply the unfolding method. Iterative method is used to solve this kind of problem [45].

The method uses a generalized encoding matrix notation. The MR encoding can be represented using a matrix formula

$$Ex = b \tag{3.7}$$

where x is the object (image) vector, b is the k-space samples vector and E is the encoding matrix. x is obtained by iteratively solve the following equation

$$(E^H E)x = E^H b \tag{3.8}$$

In parallel imaging, where there are multiple coils, each coil has its own encoding function and k-space samples. The encoding matrix E becomes a large matrix that

contains all the coil encoding matrices $E = [E_1 E_2 \cdots E_{n_c}]^T, E_i, i = 1, 2, \ldots, n_c$ are the encoding matrix for coil i, n_c is the number of coils. Similarly, the sample vector $b = [b_1 b_2 \cdots b_{n_c}]^T$. Thus, equation 3.8 can be expressed in a blocked matrix format as:

$$[E_1^H E_2^H \cdots E_c^H] \begin{bmatrix} E_1 \\ E_2 \\ \vdots \\ E_c \end{bmatrix} x = [E_1^H E_2^H \cdots E_c^H] \begin{bmatrix} b_1 \\ b_2 \\ \vdots \\ b_c \end{bmatrix} \tag{3.9}$$

Gridding algorithm have already been successfully used in SENSE reconstruction to construct E and E^H [45].

There are possible improvements on the Non-Cartesian SENSE method. Reconstruction method other than gridding, such as NUFFT, has been incorporated into SENSE [50]. *A priori* information has also be used for image quality improvement, such as POCSENSE [51].

3.2.3 Summary on Parallel Imaging

Parallel imaging techniques are commercially available now. In clinical routines nearly all MRI methods can be achieved by parallel MRI to increase scan speed with out the need of upgrade the gradient system. Parallel imaging technique can also improve the image quality and SNR ratio.

For non-Cartesian sampling patterns, k-space based method GRAPPA utilizes sensitivity information to perform k-space interpolation. Full FOV images from each coil are reconstructed, which are then combined using sum of square method. There

is no explicit sensitivity map computations. SENSE uses sensitivity information in image domain. It adopts an iterative method, simulating the frequency encoding and coil sensitivity encoding from image domain to k-space.

Numerical comparison showed that SENSE has lower artifacts than SMASH [52]. GRAPPA has better image quality than SMASH and VD-AUTO-SMASH [53]. When high quality coil sensitivity maps are available, SENSE will produce a better image. When this information is not available, then GRAPPA is a better choice [53].

In the parallel imaging applications used in this thesis, such as phantom, fruit, brain, cartilage, etc. the sensitivity map is obtainable. So this work is based on the SENSE method.

3.3   Evaluation of SENSE with
Gridding, BURS and NUFFT

Besides gridding, BURS and NUFFT can be incorporated in SENSE. A recent research showed that reconstruction from least square (LS)_NUFFT in SENSE has smaller image error compared with using gridding [38, 50]. BURS has been applied in k-space based parallel reconstructions such as PARS [54, 55]. In this section, we will compare the similarities and differences of these methods. Then in the next section we will show reconstruction from simulations and *in vivo* reconstructions.

In the above iterative SENSE framework, the construction of E and E^H can use any available methods. The equations from different methods discussed in previous sections are re-write here in a similar matrix-vector operation format, followed by

comparison and performance evaluation.

3.3.1 Gridding

It has been shown that SENSE with gridding can efficiently reconstruct image from arbitrary k-space samples [45]. Gridding defines a decoding procedure which recovers image x directly from k-space samples b as

$$x = PF^H TDb \tag{3.10}$$

where P is an N-by-N diagonal matrix used for post-compensation, N is the total number of pixels in x, F is FFT operation and F^H is equivalent to inverse FFT operation with a different scaling factor, T is a sparse N-by-M interpolation coefficients matrix which performs interpolation from density compensated non-Cartesian samples to Cartesian grid points, M represents the number of k-space samples, and D is an M-by-M diagonal matrix with sampling density compensation values on its main diagonal. P, T and D are all real-valued matrices. The coefficients in T are computed using the convolution-resampling method as defined in gridding [15]. T is sparse because of the finite length of convolution kernel. That is, for a given Cartesian grid point, which corresponds to one row in T, the interpolation coefficients from most of the non-Cartesian samples are 0 except those fall into the neighboring region within the interpolation kernel.

Because encoding and decoding operations are complex conjugate of each other [45], the encoding matrix in gridding method is defined as

$$E = T^H FP^H = T^H FP \tag{3.11}$$

The DCF matrix D is not necessary in the encoding step because of the uniform density of Cartesian grid. For parallel imaging, taking the coil sensitivity into account, the encoding matrix for one coil is

$$E_i = T^H FPC_i \tag{3.12}$$

where C_i is a complex-valued diagonal matrix of dimension N-by-N, with sensitivity values of the i-th coil on its main diagonal.

The overall parallel reconstruction problem using gridding is

$$\sum_{i=1}^{n_c}(C_i^H PF^H TDT^H FPC_i)x = \sum_{i=1}^{n_c}(C_i^H PF^H TDb_i) \tag{3.13}$$

where n_c is the total number of coils. D in equation 3.13 serves for preconditioning purpose, which can improve the convergence speed of the iterations [45].

The iterative SENSE reconstruction with gridding is illustrated in figure 3.2. Only one coil channel is shown. The operation order of C_i and P are interchangeable because they are both diagonal matrices.

3.3.2   BURS

In a matrix format, blocked uniform resampling (BURS) can be written as

$$Ay = b \tag{3.14}$$

where $y = Fx$ is the Fourier transformation of image x, and A is an interpolation coefficient matrix with dimension of M-by-N. y is determined by

$$y = (A^H A)^{-1} A^H b = A^\dagger b \tag{3.15}$$
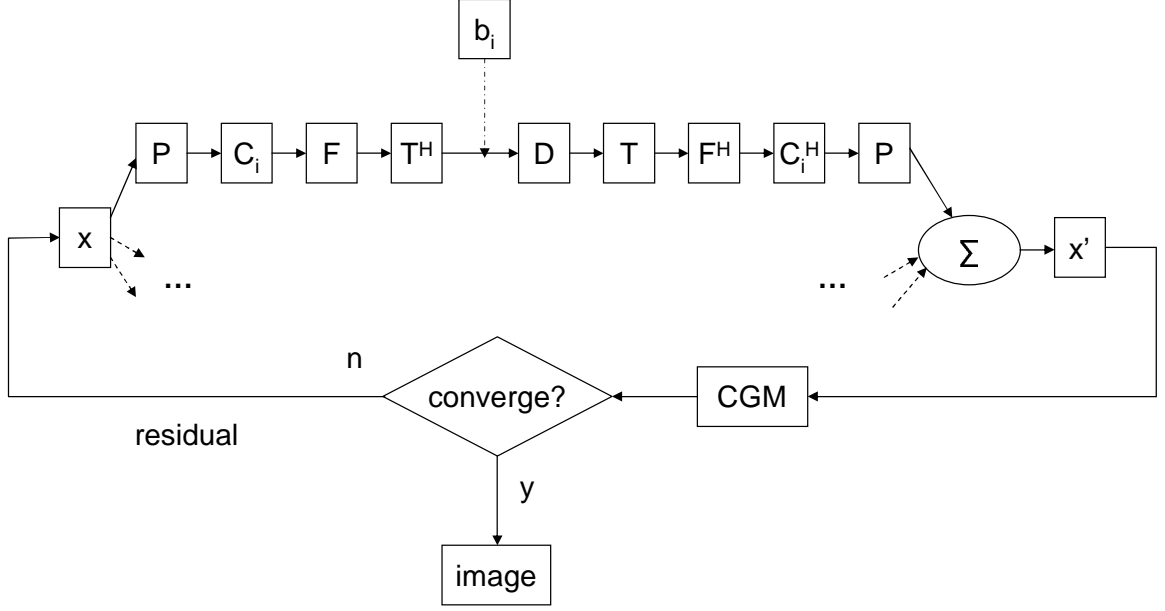
Figure 3.2: Iterative SENSE reconstruction.

using SVD. The image x is then obtained by directly performing an inverse FFT on y.

BURS can also be incorporated in the iterative SENSE reconstructions. Because only a few Cartesian grid points are used to interpolate each non-Cartesian sample, A in equation 3.14 is in sparse format. In fact we have

$$A = T^H \tag{3.16}$$

where T is the interpolation matrix in equation 3.10 in the gridding method. Constructing and storing A is not difficult with sparse matrix techniques. However, SVD computation of $A^\dagger$ is still not practically feasible, construction of the local problems of equation 2.10 is still required. $\bar{A}$ uses the values in A, and the computed $\bar{A}^\dagger$ is put back to the corresponding positions in $A^\dagger$. $A^\dagger$ is also a sparse matrix.

If a better interpolation function such as Kaiser-Bessel kernel is applied instead of the original truncated *sinc*, the encoding operation in BURS is expressed as

$$AFPx = b \tag{3.17}$$

and

$$E = AFP \tag{3.18}$$

where P is a compensation operator as in gridding to compensate the effect of Kaiser-Bessel kernel.

Using similar iterative algorithm as in ref. [45], the overall parallel reconstruction problem using BURS becomes

$$\sum_{i=1}^{n_c}(C_i^H PF^H A^\dagger AFPC_i)x = \sum_{i=1}^{n_c}(C_i^H PF^H A^\dagger b_i) \tag{3.19}$$

Considering equation 3.15, the difference in equation 3.13 and 3.19 is that $TD = A^H D$ being replaced by $A^\dagger = (A^H A)^{-1}A^H$. As mentioned before, gridding uses diagonal matrix D to approximate the more generalized compensation matrix $A(A^H A)^{-2}A^H$, which involves matrix inversion and is typically numerically unstable as the problem is often ill-conditioned [31]. Regularization method such as truncated SVD (TSVD) or Tikhonov regularization is applied in BURS to stabilize the computation [21, 54].

3.3.3 NUFFT

NUFFT contains two general steps: a regular FFT operation on the image x, which results in Cartesian grid k-space samples, and an interpolation of these grid

data onto the non-Cartesian trajectory b.

$$AFPx = b \tag{3.20}$$

where A denotes interpolation coefficient matrix, which is again sparse, performing interpolation from Cartesian grid to non-Cartesian samples. P is a scaling factor to pre-compensate for imperfections in later interpolation, which may be complex-valued [19]. P can be considered to be similar to post-compensation for interpolation kernel.

Reconstruction using NUFFT is to solve the following least square problem

$$P^H F^H A^H AFPx = P^H F^H A^H b \tag{3.21}$$

Reconstruction using NUFFT is typically implemented by iteratively solving equation 3.21 using least square method [19].

For parallel imaging, NUFFT defines an encoding operation from the image to k-space samples as

$$E = AFPC_i \tag{3.22}$$

The overall parallel reconstruction problem using NUFFT is

$$\sum_{i=1}^{n_c} (C_i^H P^H F^H A^H AFSC_i)x = \sum_{i=1}^{n_c} (C_i^H P^H F^H A^H b_i) \tag{3.23}$$

Comparing equation 3.23 and 3.13, although they are defined using two different methods, they have a very similar form. For non-parallel reconstructions, gridding is simply one-time interpolation from k-space samples to Cartesian grid. In parallel SENSE reconstruction, however, it adopts an iterative encoding/decoding procedure

with feedbacks from image to k-space. The idea is similar to NUFFT reconstruction. The main difference is that gridding has a density compensation matrix which acts as a weighting factor.

3.4   Implementation

In this section reconstructions using the methods discussed above from both 2D and 3D data set are performed.

3.4.1   Simulation

In computer simulations, a four channel phased array coil (surface coils) with rectangular elements surrounding the phantom without overlapping was simulated, as shown in figure 3.3.
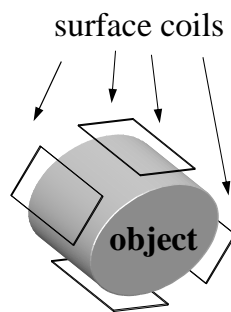

Figure 3.3: Coil arrangement for parallel imaging.

A 2D modified Shepp-Logan phantom was used as a standard image [56]. Coil sensitivity maps were computed based on the Biot-Savart Law [57,58]. The k-space spiral sampling trajectory contains 32 interleaves, with 2048 points on each interleaf.

Reduced sample data sets used 16 equally spaced interleaves to simulate a reduction factor of 2. Figure 3.4 illustrates one spiral interleaf, modified Shepp-Logan phantom and the aliased image obtained by computing the sum of square of image from each coil with reduced data. The contrast of the sum of square image was adjusted to illustrate the alias artifact. Image resolution was set to 256×256. In gridding reconstruction, the convolution kernel was a Kaiser-Bessel window with width 4, and β was chosen according to ref.[15]. The density compensation in equation 3.13 was pre-computed using the Voronoi method [24]. The min-max interpolation kernel using 4 points was used for NUFFT [19]. The interpolation kernel in BURS was Kaiser-Bessel with the same parameters as in gridding. Block size was set to 8, $\Delta k = 4$, $\delta\kappa = 3$, TSVD threshold was 0.01.

Figure 3.4: Left: 2D Spiral trajectory. Middle: Phantom image. Right sum of square image from each coil.

A 3D modified Shepp-Logan phantom was used for 3D simulations, as shown
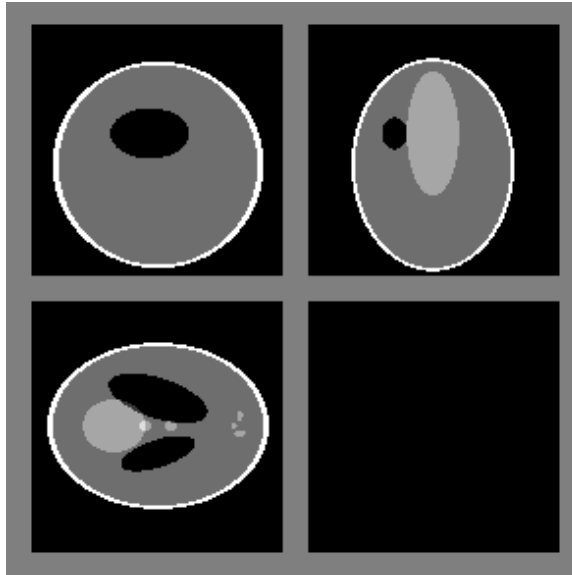
Figure 3.5: 3D modified Shepp-Logan phantom. The 3 sub-images are x-y, x-z and y-z section images.

in figure 3.5. Two sampling patterns were used, stack of spiral and projection reconstruction (radial) trajectories, as illustrated in figure 3.6. The spiral set contained 8 stacks, one per k_z phase encoding location. There were 8 interleaves per stack, with 2048 points on each interleaf. Image resolution was $128 \times 128 \times 8$. Again a reduction factor of 2 was simulated by using 4 interleaves on each stack, which means no alias along z direction. The reconstruction parameters along k_x and k_y were the same as in 2D. The width of the interpolation kernel along k_z direction was set to 2. DCF in gridding was computed using the 2D Voronoi method for each slice, neglecting the interference of points on neighboring slices. Block size along k_z in BURS was set to 1, $\Delta k_z = \delta \kappa_z = 1$.

The k-space samples along the 3D projection reconstruction (radial) trajectory

(a) Stack of spiral   (b) Projection   reconstruction (radial)
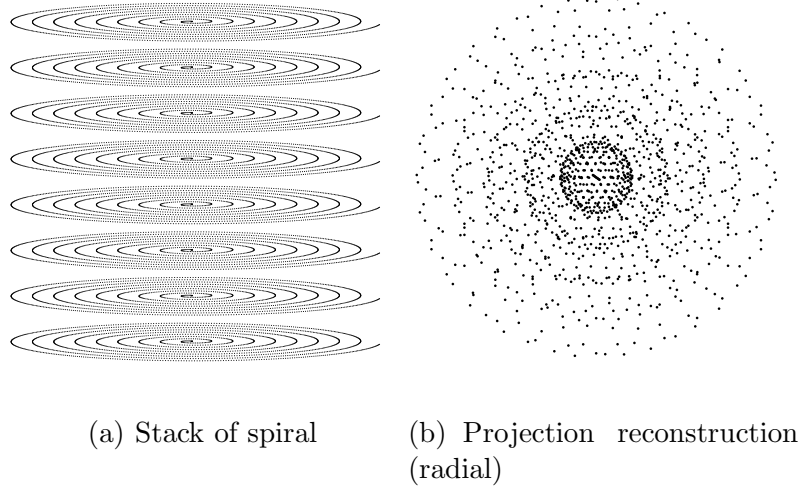
Figure 3.6: 3D trajectories.

consists of 13106 radial half-lines with 32 samples apiece for a $128 \times 128 \times 128$ element volume. The maximum sample spacing was the same in all directions, as well as the spacing along the outermost sphere, corresponding to an isotropic FOV. The reconstructed image resolution was $128 \times 128 \times 128$. A reduction factor of 2 was achieved by removing half of the radial lines evenly distributed through 3D k-space. So in this case the alias appears in all dimensions. Kernel width was set to 2 in all dimensions for all the methods. In BURS, the block size is set to 2, $\Delta k = \delta \kappa = 2$, TSVD threshold was 0.01. Accurate DCF using 3D Voronoi tessellation method is too computationally demanding. A simpler version which computes the square of the distance to the origin was used [59].

The performance of the methods were evaluated in the sense of root mean square error (RMSE), which was computed as

$$\epsilon = \sqrt{\frac{\sum\limits_{i} \left(x(i) - p(i)\right)^2}{N}} \tag{3.24}$$

where p is the phantom image and x is the reconstructed image, N denotes the total number of pixels.

3.4.2   MR data Reconstruction

Phantom and *in vivo* images were acquired on a GE 1.5T LX scanner using a four channel phased array coil. The coil arrangement was similar to the simulations. The same 2D and 3D sampling trajectories as in the simulations were used. The reconstruction parameters were also the same as in the simulation section.

For 2D images, the 256×256 image covered a FOV of 20×20 cm^2 with in-plane resolution of $0.8mm$. A reduction factor of 2 was achieved by acquiring 16 interleave of spirals out of 32. Low resolution fully sampled body coil and phased array coil reference images were used to compute coil sensitivity maps. The reference image was 1/4 of the full resolution.

For the 3D stack of spiral acquisitions, the FOV was $28 \times 28 \times 2.7$ cm^3 , with image resolution of $128 \times 128 \times 8$. Again a reduction factor of 2 was applied by acquiring 4 interleaves out of 8 on each stack. Fully sampled body coil and phased array coil images were used as references to compute the 3D coil sensitivity maps. In clinical application this kind of reference data acquisition will counteract the merit of parallel imaging. But here in experiment step it is only used to obtain the coil sensitivity map, which will not significantly affect the final reconstruction.

The 3D projection reconstruction samples covers a FOV of $24 \times 24 \times 24$ cm^3. Half of the radial line were removed to achieve a reduction factor of 2. Again full

resolution projection reconstruction acquisitions of both body coil and phased array coil images were used as references to compute 3D coil sensitivity maps. The reconstructed image resolution was $128 \times 128 \times 128$.

A zero image was used as the starting image of the iterations, and the reconstruction was terminated after a predefined number of iterations. All three reconstruction methods (SENSE with gridding, BURS, and NUFFT) were implemented in MATLAB (Mathworks, Natick, MA). The programs were tested on a Linux computer with Intel P4/3.2G CPU and 2GB of memory.

3.5   Results
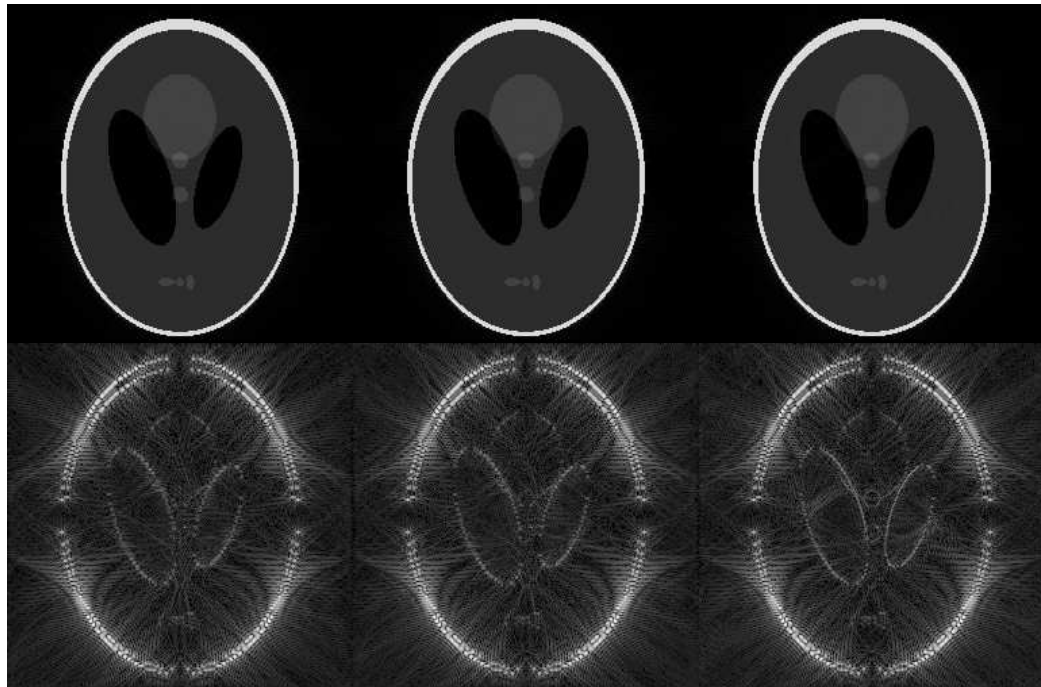
Figure 3.7: Reconstructed 2D images and difference with phantom. Left column: gridding. Middle column: BURS. Right column: NUFFT.
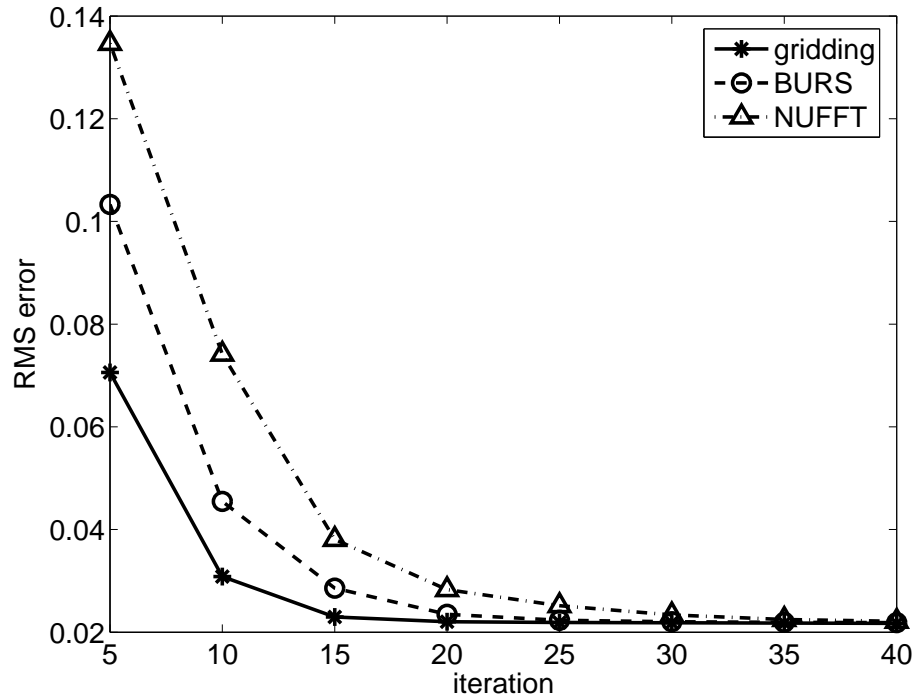
Figure 3.8: RMSE of 2D simulations.

Figure 3.7 shows the reconstruction of 2D simulations using gridding, BURS and NUFFT methods after 40 iterations. The difference images compared with the standard phantom were also shown. The convergence of RMS errors were compared in figure 3.8. Gridding has the fastest convergence rate. The final RMS error values after 40 iterations are very close to each other, which is 0.0217 for gridding, 0.0219 for BURS, and 0.0221 for NUFFT.

2D MR data reconstruction results and body coil reference image and sum of square of aliased images from each coil are shown in figure 3.9. 40 iterations were performed for the phantom image in the top row. TSVD threshold in BURS was 0.01. For the *in vivo* image in the bottom row, a total of 15 iterations were
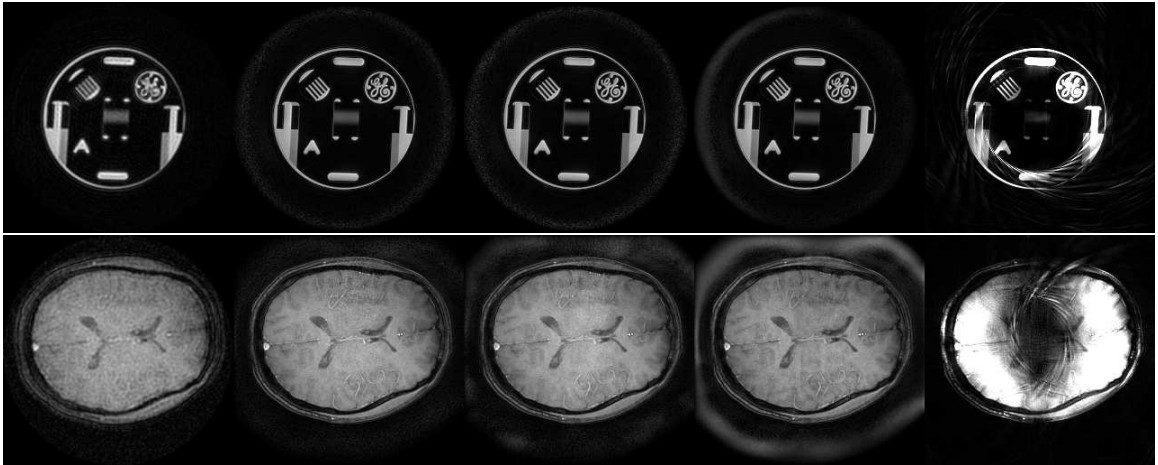
Figure 3.9: Reconstruction from 2D MR data. Top row: GE cylinder phantom image. Bottom row: *in vivo* brain image. Images from left to right: full resolution body coil reference image, gridding reconstruction, BURS, NUFFT, sum of square image from each coil. The contrast of the sum of square images were adjusted to clearly show the alias.

performed. TSVD threshold in BURS was 0.1. The image qualities at locations in the object are similar. But in all the methods there are some kind of background noise amplification. In BURS and NUFFT this phenomenon is more obvious. The computation time for each iteration is around 1.4 second for all three methods.
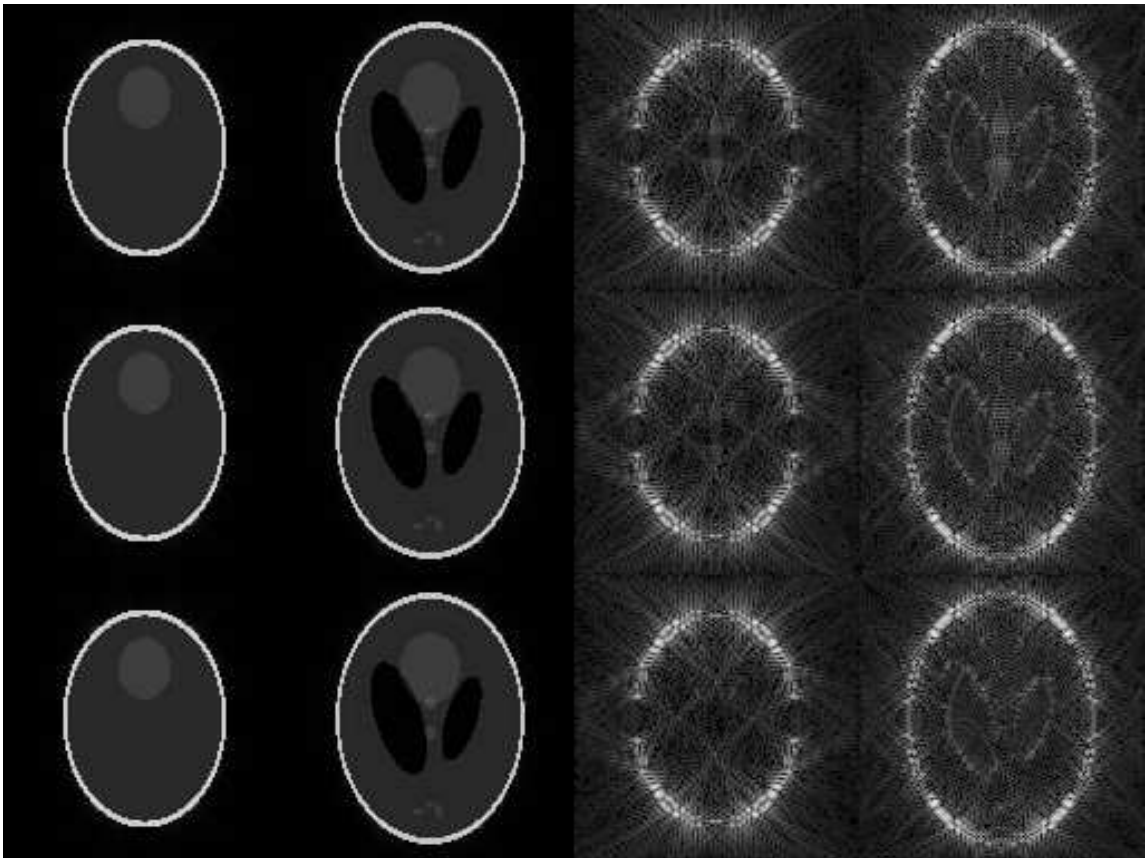
Figure 3.10: Reconstructed images and difference with 3D stack of spiral simulation. Left two columns: two slices of reconstructed images. Right two columns: corresponding difference images. Top row: gridding reconstruction. Middle row: BURS. Bottom row: NUFFT.

Figure 3.11: RMSE of 3D simulations with stack of spiral trajectory.

Figure 3.10 shows the reconstruction of 3D simulations with stack of spiral sampling pattern. A modified 3D Sheep-Logan phantom was used [60]. Two of the eight slices and the corresponding difference images after 40 iterations are shown. Both the reconstructed images and the difference images of the three methods look similar to each other. RMS error convergence are shown in figure 3.11. The final RMS error value is 0.0261 for all three methods. Gridding still shows the fastest convergence speed relative to the number of iterations. The computation time for each iteration is 4.9 seconds for gridding, 4.5 seconds for BURS and 5.4 seconds for NUFFT.

Reconstruction from 3D simulations with radial trajectory is shown in fig-
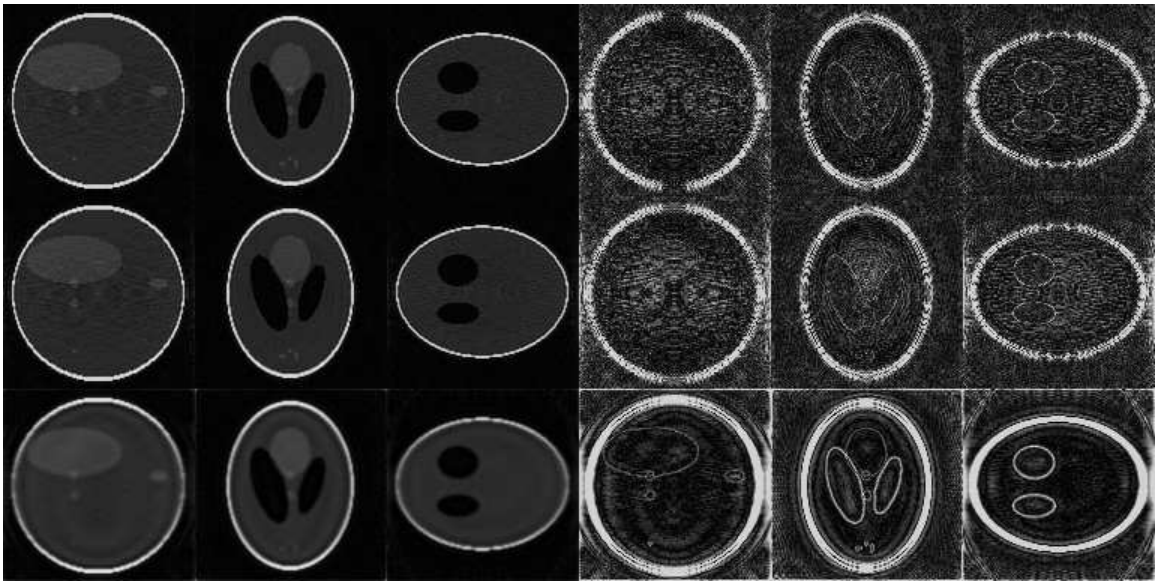
Figure 3.12: Reconstructed images and difference with 3D radial trajectory simulation. Left three columns: x-z,x-y and y-z slices of reconstructed images. Right three columns: corresponding difference images. Top row: gridding reconstruction. Middle row: BURS. Bottom row: NUFFT.
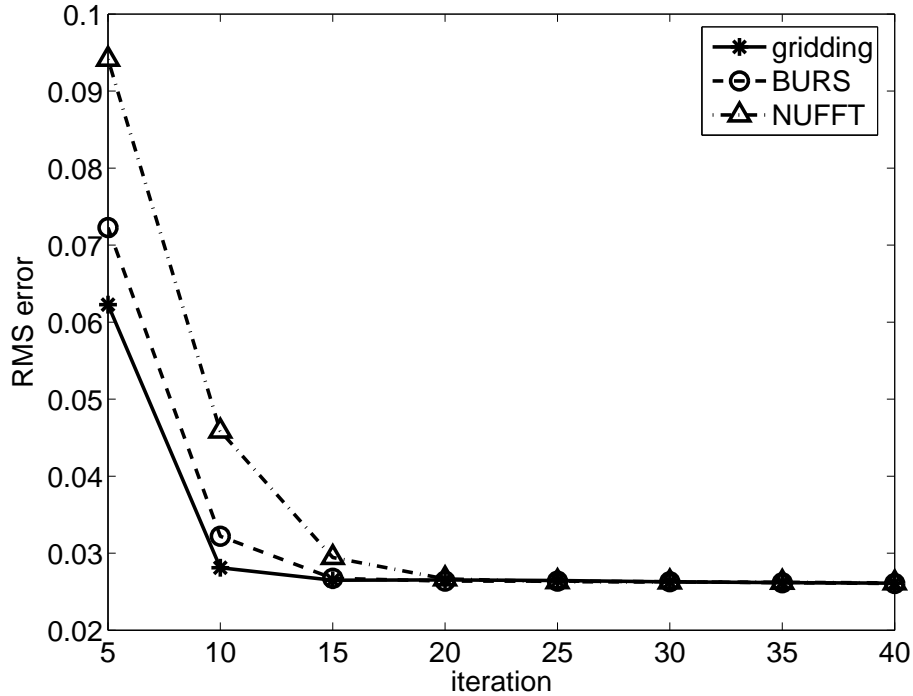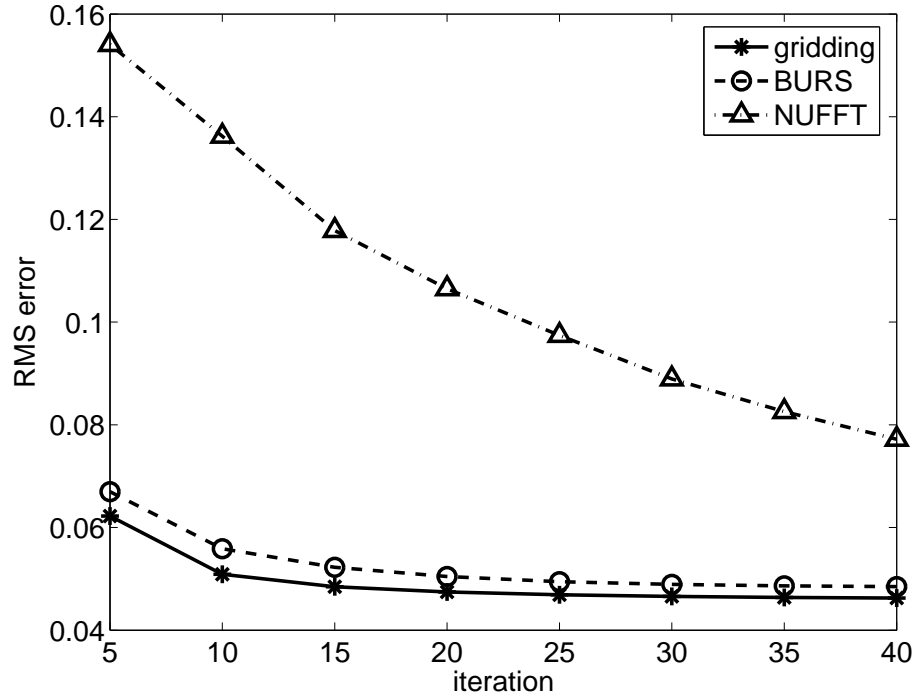
Figure 3.13: RMSE of 3D simulations with radial trajectory.

ure 3.12. The image resolution is $128 \times 128 \times 128$. Reconstructed and difference images from x-y, y-z and x-z planes are shown. For this large data set, the slow convergence of NUFFT results in a blurred reconstruction after 40 iterations. This is also revealed in the RMS error convergence plot in figure 3.13. The NUFFT reconstruction has a larger RMS error compared with the other two methods. The final value after 40 iterations is 0.0417 for gridding, 0.0458 for BURS, and 0.0690 for NUFFT. The computation time for each iteration is 58 seconds for gridding, 51 seconds for BURS and 48 seconds for NUFFT. Note from the plot that RMSE curve of NUFFT is continuously decreasing. With enough number of iterations, it is possible to converge to the same RMSE level as gridding and BURS as in the 2D and 3D stack of spiral

cases.
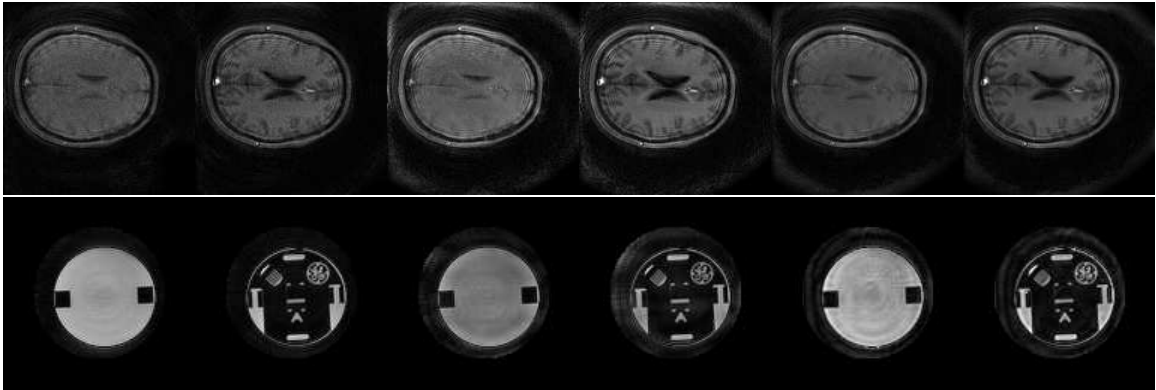
Figure 3.14: Reconstruction from 3D MR data. Top row: reconstruction from 3D stack of spiral samples. Bottom row: reconstruction from radial samples. Left two columns: gridding reconstruction. Middle two columns: BURS reconstruction. Right two columns: NUFFT reconstruction.

3D reconstruction from MR data were shown in figure 3.14. In the stack of spiral case, the image qualities are similar. There are still obvious background noise amplifications in BURS and NUFFT. In the radial sampling case, there are noise amplification beyond the object support in all the three methods. The images shown were post-processed by applying a circle mask around the object to suppress the background noise. NUFFT reconstruction is blurred compared with gridding, which is consistent with the simulation case. The BURS reconstruction contains larger errors inside of the object. The TSVD threshold was set to 0.1. A better threshold

value in TSVD may improve the BURS image quality. But the optimal value is not easy to obtain.

3.6   Discussion

Reconstruction of parallel MR imaging using the iterative SENSE algorithm can be achieved by a variety of methods. Gridding, BURS and NUFFT can all be incorporated. The system equations share a similar form.

The interpolation coefficient matrix T in gridding and A in BURS are the transpose of each other. The matrix A in min-max NUFFT has the same non-zero elements as in gridding and BURS, but it is complex-valued. So the storage requirement is doubled. Computation of density compensation D in gridding can be achieved in a variety of ways, the computation can be very simple by using ADF, or complex by the Voronoi method. The pseudoinverse matrix $A^{\dagger}$ in BURS is computed using SVD, which in general is a computation demanding step. NUFFT does not require any other pre-computations besides A.

The computations in each iteration for all the methods includes FFT, IFFT and some matrix-vector multiplications. These multiplications are A, diagonal matrix D, and A^{H} in gridding, A and $A^{\dagger}$ in BURS, and A and A^{H} in NUFFT. In BURS $A^{\dagger}$ is also sparse. The number of non-zero elements depends on the values of Δk and $\delta\kappa$, but is similar to that in A. So the total number of such multiplications are similar in the above three methods. But because NUFFT has complex valued A, the computations are doubled. These comparisons are summarized in table 3.1.

	gridding	BURS	NUFFT
Interpolation matrix	$T(=A^H)$	A	A with complex values
Other pre-computation	D	$A^\dagger$	none
Computations	FFT, IFFT, $A^H D A$	FFT, IFFT, $A^\dagger A$	FFT, IFFT, $A^H A$

Table 3.1: Comparison of gridding, BURS and NUFFT in SENSE.

In summary, gridding, BURS and NUFFT can all be applied in SENSE. Gridding has the fast convergence speed and relatively smaller RMS errors and background noise. The rest of this thesis will focus on the reconstruction using gridding and SENSE.

CHAPTER 4
REGULARIZATION, GRID SIZE, AND INTERPLATION COEFFICIENT

In this chapter, methods that improve reconstruction quality and reduce the computation and storage burden for parallel MRI reconstructions are proposed and evaluated via computer simulations.

4.1   Method

4.1.1   Edge Preserving Regularization

As mentioned in the previous chapter, the measured sample data b and the original image x can be related in a linear model as

$$b = Ex + n \tag{4.1}$$

where n is white Gaussian noise and E is the encoding matrix which is a linear operator. In the framework of least-square or maximum *a posteriori* (MAP), the estimated image $\hat{x}$ is given by

$$\hat{x} = arg\,\min_{x}(\psi(x)) \tag{4.2}$$

where ψ is an objective function to be minimized. Typically

$$\psi(x) = ||b - Ex||^2 \tag{4.3}$$

The problem of reconstruction is often an ill-posed problem [61–63]. Many different images can be obtained from data b. *A priori* information is thus necessary to

be imposed on the image reconstruction to regularize the result. It is often expressed as an additional regularization term in the objective function.

$$\psi(x) = \psi_1(x) + \lambda\psi_2(x) \tag{4.4}$$

where ψ_1 is a term that measures the faithfulness of the result to the data, such as in equation 4.3. ψ_2 is the regularization function, or penalty function, which is also called as a potential function in the Markov random field approach [62, 64]. λ is a positive penalty coefficient that balances the two terms.

A more generalized version of objective function is a penalized weighted least-square (PWLS) function [65]. The form is as follows

$$\psi(x) = \frac{1}{2}(b - Ex)^H \Sigma^{-1}(b - Ex) + \lambda\psi_2(x) \tag{4.5}$$

where Σ is a diagonal matrix with weighting factors on its main diagonal.

The penalty term ψ_2 can be chosen from a variety of forms, or the combination of many different penalty functions

$$\psi_2(x) = \lambda_1\psi_{21}(x) + \lambda_2\psi_{22}(x) + \cdots + \lambda_n\psi_{2n}(x) \tag{4.6}$$

There are some assumptions about the property of the image. One assumption is that the image is globally smooth. A quadratic potential function can be imposed on the image as a roughness penalty. However, this penalty tends to yield an over-smoothed image [66]. A more realistic assumption is that the image contains piecewise smooth regions separated by edges, which is called edge-preserving roughness penalty, or edge-preserving regularization [64, 66]. A non-quadratic potential function ψ_2 is needed in this circumstance.

ψ_2 can be defined in many ways to achieve different edge-preserving requirements. It is, in general, the sum of the functions of a derivative of the image. Charbonnier *et al.* proposed several conditions for the potential function based on the assumption that a large value in the gradient corresponds to an edge while a small one is due to noise [62]. Table 4.1 shows several forms of ψ_2 [62, 66, 67]:

quadratic	$\psi(x) = x^2/2$
hyperbola	$\psi(x) = \sqrt{\delta^2 + x^2} - \delta^2$
Huber function	$\psi(x) = \begin{cases} x^2/2 & |x| \leq \delta \\ \delta|x| - \delta^2/2 & |x| > \delta \end{cases}$
broken parabola	$\psi(x) = min\{x^2, \delta^2\}$

Table 4.1: Penalty functions.

The δ is a regularization parameter depending on the noise level. Figure 4.1 illustrates the shape of these functions.

Geman *et al.* [68] introduced a set of functions $D_C^k, k = 1, 2, 3$ for the k-th order derivative on a clique C to measure the priori smoothness constraint. The clique C is defined as any pair of horizontal, vertical or other adjacent pixels. In 2D, for the first order case, two adjacent pixels (s, t) are considered. Their relationship is shown in figure 4.2. $D_C^1 X$ is in fact the intensity difference of the two pixels. This nearest neighbor model does not consider the diagonal adjacent pixel, so it will introduce
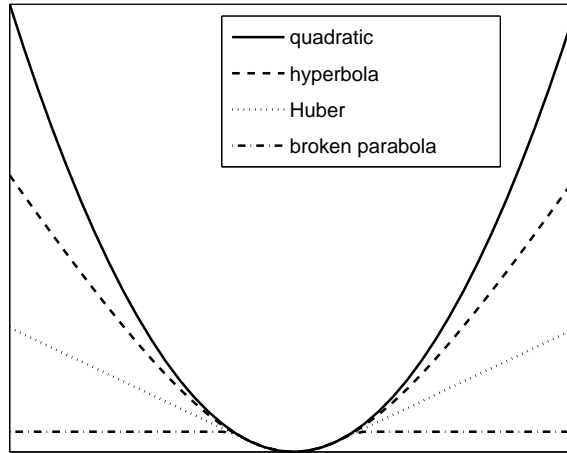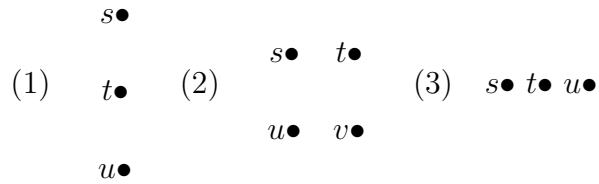
Figure 4.1: Potential functions.

(1) $\quad s\bullet$

$\quad\quad t\bullet$

(2) $\quad s\bullet\ t\bullet$

$$D_C^1(X) = X_s - X_t, C = (s, t)$$

Figure 4.2: First order clique.

$$
\begin{array}{llll}
& s\bullet & & \\
(1) \quad t\bullet & (2) \quad \begin{array}{cc} s\bullet & t\bullet \\ u\bullet & v\bullet \end{array} & (3) \quad s\bullet \ t\bullet \ u\bullet \\
& u\bullet & &
\end{array}
$$

$$
D_C^2(X) = \begin{cases} X_s - 2X_t + X_u & \text{if } C \text{ is of type (1) or (3)} \\ X_s - X_t - X_u + X_v & \text{if } C \text{ is of type (2)} \end{cases}
$$

Figure 4.3: Second order clique.

a bias towards the vertical and horizontal edges [68]. For the second order case, the second differences are considered, i.e. the differences between components of the gradient at adjacent pixels. There are three types of cliques as shown in figure 4.3. Here $D_C^2(X)$ corresponds to the discrete approximation to the difference between elements of the gradient vector [68].

First and second order schemes are most useful in practical applications. Third and higher orders are too complex and are thus rarely used [63]. In 2D cases, the first order for the nearest four pixels and second order for the nearest eight pixels are the most studied neighbors. In most 3D problems, the cross slice distance is typically larger than that on the same slice. The neighbor points in the third dimension can be limited to the first order only, i.e. one pixel at the corresponding position on the upper slice and one on the lower slice. Villain *et al* proposed a fast implementation using only two elements cliques to limit the computational cost [63]. The gradient D
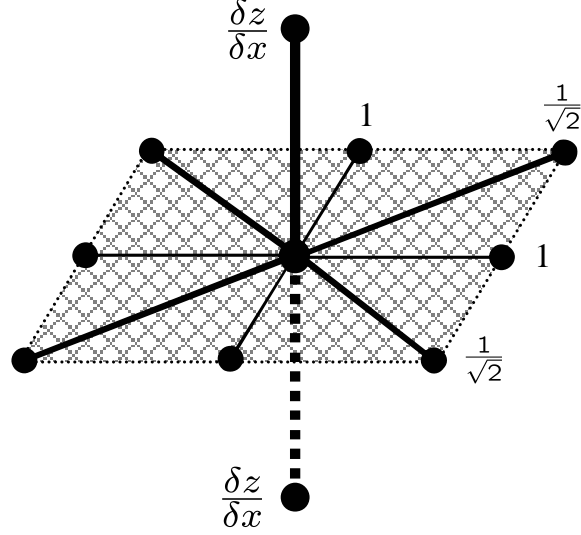
Figure 4.4: 3D neighbor points and weighting coefficients.

is defined as

$$D = \frac{\Delta I}{d} \tag{4.7}$$

where ΔI is the intensity difference of the two elements and d is the weighting factor. For neighbors in the same slice, d is 1 for horizontal and vertical neighbors and $1/\sqrt{2}$ for diagonal neighbors. For cross slice neighbors above or below the current element, $d = \delta z/\delta x$ which is the ratio of cross-slice and in-slice distance [63, 65]. Figure 4.4 demonstrates the neighbor points scheme and their corresponding weights.

As an example, the cost function for the simplest quadratic penalty is [65]

$$\psi_x(x) = \frac{1}{2}x^T R x = \frac{1}{2}\sum_j \sum_{k \in C} w_{jk}\frac{1}{2}(x_j - x_k)^2 \tag{4.8}$$

where C is the clique of adjacent pixels. For other penalty term such as Huber function, the $(x_j - x_k)^2$ in equation 4.8 is replaced by the corresponding functions as described in table 4.1.

4.1.2   Iterative Method To Calculate

Penalty Coefficient

The penalty coefficient has great impact on the reconstruction. Small values typically results in little improvement. While large values tends to yield over-regularization with strong alias artifact and large RMSE [65]. In MRI image reconstruction, empirical coefficient values are often used [19, 69, 70]. Other methods include testing the penalty function on simulated data of the same size among varies of parameters. Then chose the one with best performance for *in vivo* applications [71]. The limitation of these methods is that the derived coefficient form one data does not always suitable for other MR data.

This thesis uses an iterative penalty coefficient estimation method. It follows similar logic as in the trust region or restricted step optimization method [72]. Varying penalty coefficient is applied during iterative reconstruction. A threshold is applied on the change of each step. A step-ratio is defined as the ratio of the metric from current iteration over that from the previous iteration. The assumption is that the change in steps becomes smaller when the search function approaches the solution.

In implementation, the first several iteration steps are excluded from the step-ratio thresholding to avoid the impact from the starting value. While after many iterations when the search function is close to solution, the search step becomes relatively small. Due to the existence of noise in data and non-accuracy of system encoding matrix calculation, it may fluctuate around the solution. So the step-ratio limitation is applied to the intermediate iterations which excludes the starting and

ending steps.

The penalty coefficient starts from a small value, which corresponds to very little constraint. With each iteration, this coefficient increases by a predefined factor (for example, 10). The new search step is calculated with the impact of current penalty coefficient. If the ratio between the new and old search step is smaller than the step-ratio threshold, this coefficient value is accepted. Then in the next step the coefficient continue to increase. If the ratio between steps is larger than the step-ratio threshold, it denotes the penalty coefficient puts too much constraint on the solution. The coefficient is decreased. Then the search step is re-calculated. The iterations continue until the a certain iteration number is reached. The penalty coefficient at the last step is the one to be used in the penalty function. The steps are illustrated in figure 4.5.

4.1.3   Object Support Regularization

Besides the general piecewise smooth assumption, other *a priori* information can be included. Object support constraint is proposed in POCSENSE (Projection onto Convex Sets SENSE) method [51], which helps to reduce background noise outside of the object to be imaged.

The SENSE methods calculates coil sensitivity maps explicitly, either using reference images or deriving from self-calibrated samples. The sensitivity information is accurate on image part by comparing reference images. But in background area the values are computed based on the interpolation-extrapolation method [13]. As shown
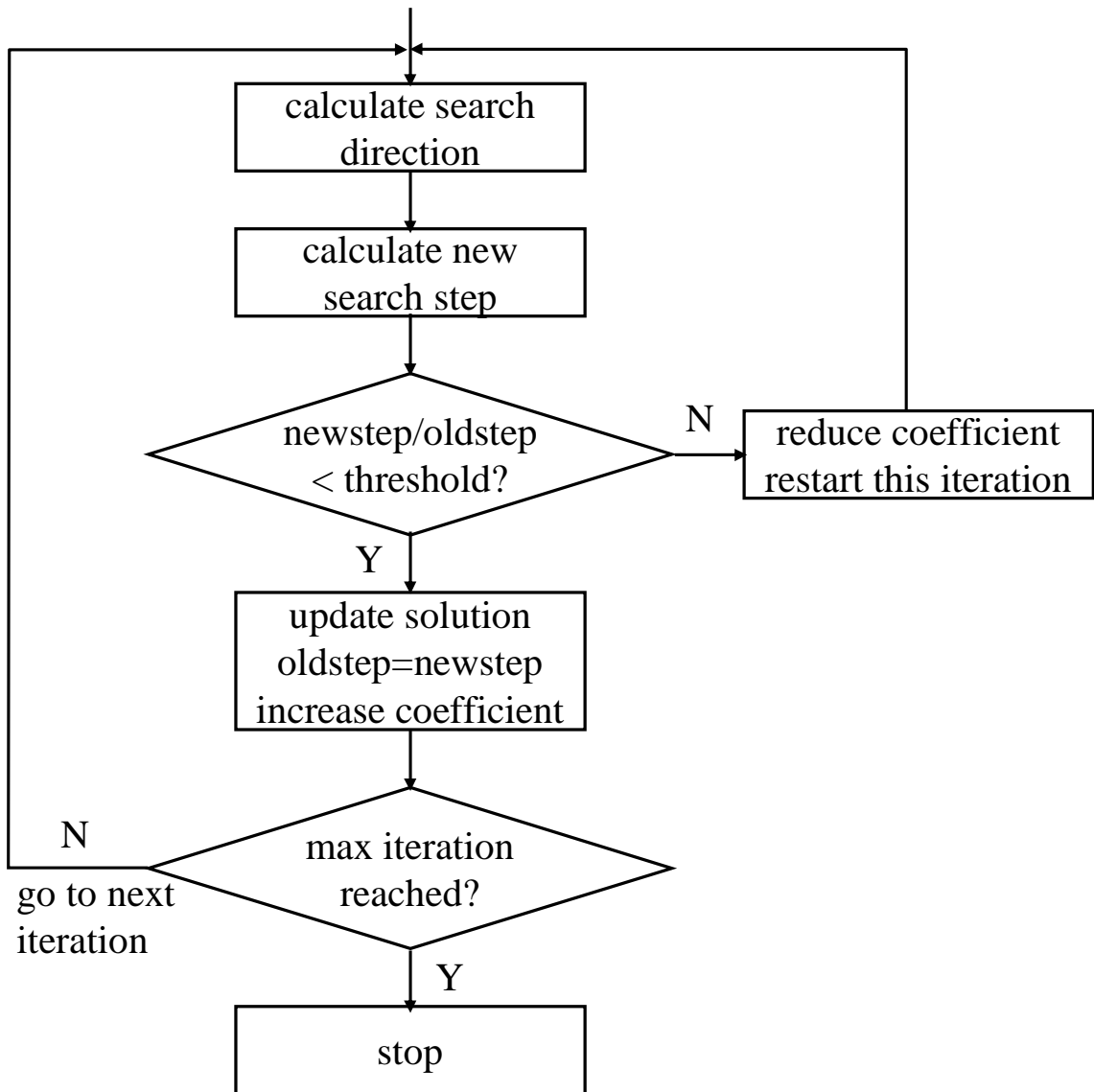
Figure 4.5: Step-ratio method flow chart.

in figure 4.6, the sensitivity in the background are different compared with the true values, which may cause the amplification of background noise. This is illustrated in figure 4.7(a)-(c).
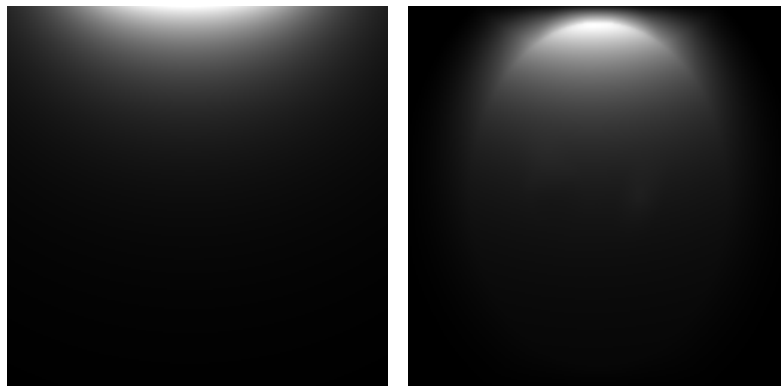
(a) Simulated sensitivity map (b) Computed sensitivity map

Figure 4.6: Ideal simulated coil sensitivity map and computed sensitivity map.

Object support constraint can help to suppress background noise. The object support S is defined as an logical matrix with 1 represents an pixel in object and 0 for background.

$$\psi_2(x) = xRx \tag{4.9}$$

$$R_{ii} = 1 - S(i) \tag{4.10}$$

where x is the image vector, R is a diagonal matrix with $1 - S(i)$ on its main diagonal. $\psi_2(x)$ is a measure of the background noise. Minimizing $\psi_2(x)$ results in minimization of background noise. The effect of object support constraint was illustrated in 4.7(d)-(f).

(a)　　　　　　　　　(b)　　　　　　　　　(c)

(d)　　　　　　　　　(e)　　　　　　　　　(f)

Figure 4.7: Image reconstruction with and without object support constraint. Top row: reconstruction without object support constraint. Bottom row: reconstruction with object support constraint. Left column: simulation, noise $\sigma = 0.02$. Middle column: simulation, noise $\sigma = 0.05$. Right column: *in vivo* reconstruction. The contrast of the images are adjusted to show the background noise.
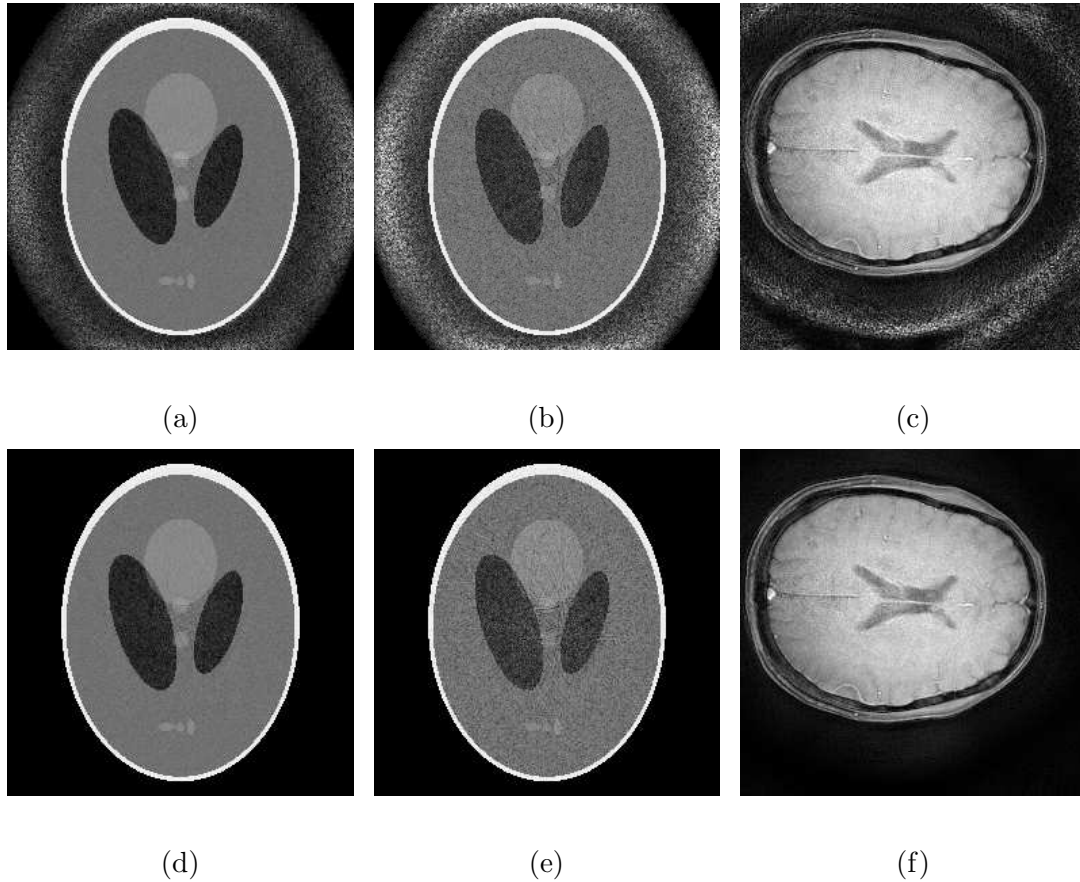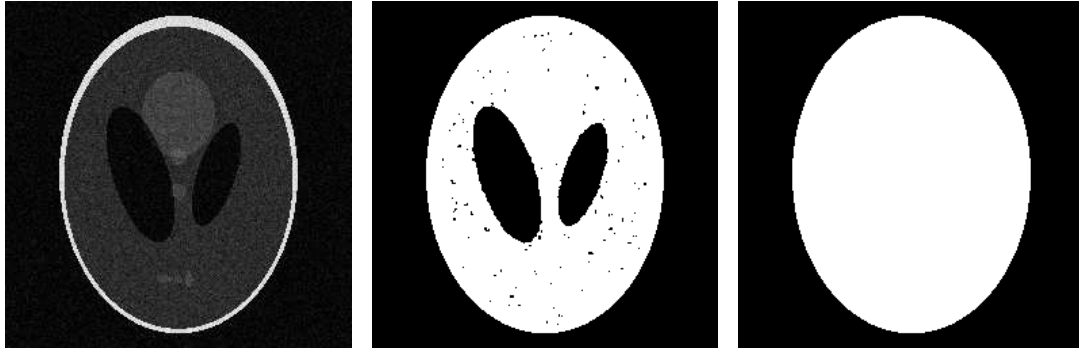
(a) Noisy image   (b) Raw object support   (c) final object support

Figure 4.8: Computation of object support.

The object support is computed as follows. First the noise level in image is estimated to obtain a threshold value. Each $x - y$ plane image is smoothed by a 3×3 Gaussian window. The mean μ and standard deviation σ of the difference with the original image is then computed. This is supposed to be the noise mean and standard deviation. The threshold is defined as $\mu + n\sigma$ where n is an adjustable small value (for example, 3). A raw support is then computed by thresholding the image and converting to a binary mask. Then a dilation-erosion operation is performed to obtain a final support with holes in image filled. An example of these images were shown in figure 4.8. There are two difference compared with POCSENSE: the object support is updated during iteration; an user defined penalty coefficient controls the strength of suppression during iteration instead of setting everything outside the object support to zero.

4.1.4   Smaller Oversampling Ratio

For large 3D problems, such as in the radial trajectory case, the computation burden and computer memory and storage requirement are also practical factors for the implementation. The previous sections focused on methods to improve image quality. Those methods introduce more computation complexity to the reconstruction. In the following sections, methods that help reduce the computation and memory requirement are analyzed.

Image alias has been discussed in previous chapters. Examples of alias patterns are shown in figure 4.9. Figure 4.9(a) shows the case of Cartesian sampling pattern, where the alias is simply periodic replica of images. As long as the Nyquist sampling theory is satisfied in k-space, the alias will not affect the center image. However, for non-Cartesian sampling patterns, the alias is highly irregular. The alias for spirals samples, for example, are shown in figure 4.9(b)-(e). Part of the alias will enter into the image, causing reconstruction errors. To minimize the alias effect, in practice a larger grid size in k-space is often used during reconstruction. Oversampling ratio of 2 (2x grid) is widely accepted [15,19,20]. As shown in figure 4.9(b), which is spiral image with 2x grid, the center part is a good reconstruction. If smaller oversampling ratio is used, alias may appear in the center part of the image, as shown in figure 4.9(c)-(e) with oversampling ratio of 1.5, 1.25 and 1 respectively. Typically larger oversampling ratio will provide better images. But due to extra computation cost, values larger than 2 are rarely used [19].

The oversampling ratio of 2 increases the computation burden as well as mem-
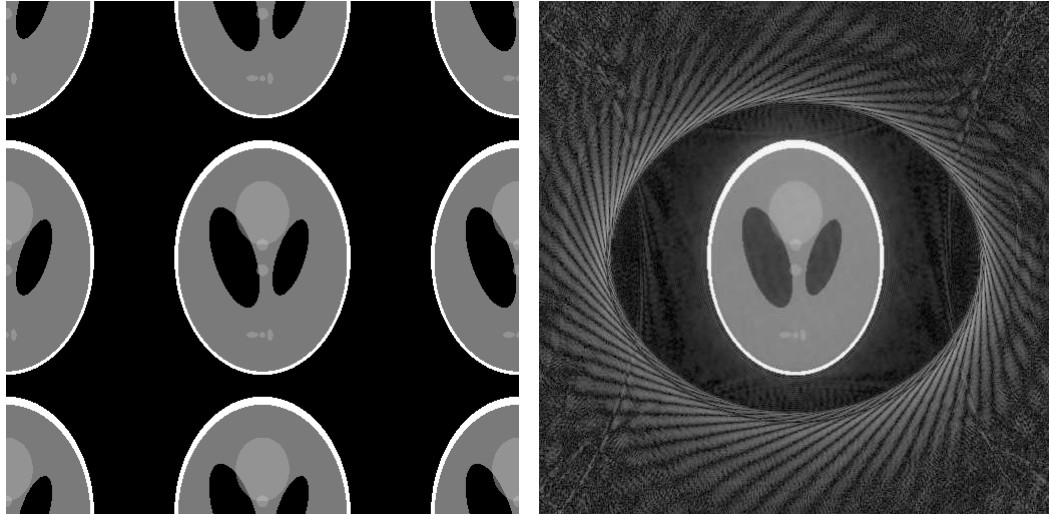
(a) Cartesian aliasing   (b) spiral 2x grid
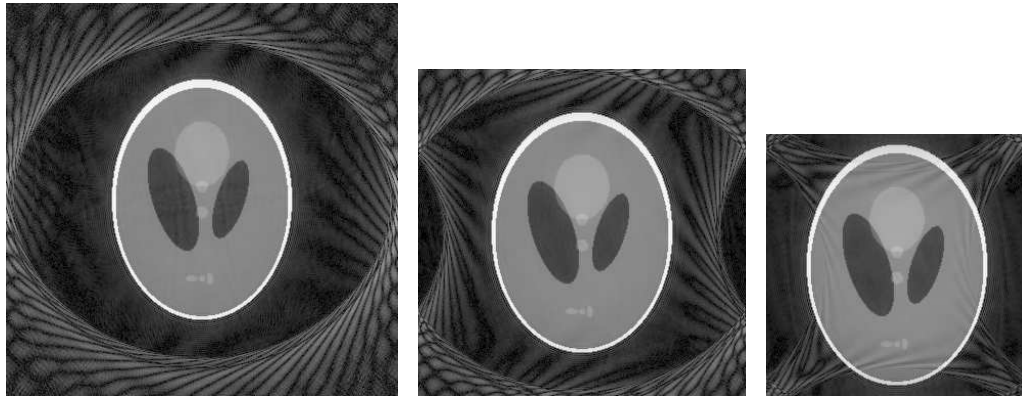
(c) spiral 1.5x grid (d) spiral 1.25x grid (e) spiral 1x grid

Figure 4.9: Oversampling ratio and alias artifact. The spiral images were reconstructed using gridding with Kaiser-Bessel kernel with width=2 and $\beta = 4.2054$. The contrast of the images are adjusted.

ory requirement to store the enlarged image. For example, a 3D image will require 8 times memory for intermediate images, and the computation time of FFT will also be more than 8 times. Recently gridding with oversampling ratio smaller than 2 was proposed by Beatty *et al.* [26]. Minimal oversampling ratio of 1.125 and 1.375 were applied with gridding to obtain accurate images in the sense of aliasing amplitude remained in the image. Different set of optimal parameter for the Kaiser-Bessel kernel were provided for different oversampling ratios [15, 26]. Parallel MRI reconstruction could use these new parameters with smaller oversampling ratio too. It needs further evaluation due to data noise, and additional impact from coil sensitivity maps. Experiments on this factor are shown in the following sections.

4.1.5 Compressing Interpolation
Coefficient Matrix

Data compression essentially eliminates less important data from the computation to make large size data computation feasible. For example, a recent study by Buehrer *et al.* showed that it is possible to compress a 32-channel MR data into 4-channel to alleviate the computation speed and memory constraints [73]. Similarly, it is possible to compress the gridding interpolation coefficient matrix.

The total number of interpolation coefficients in the interpolation coefficient matrix T in equation 3.10 is $J \times M$, where J is the number of neighbors in the interpolation and M is the total number of k-space samples. The optimal interpolation kernel used in gridding is Kaiser-Bessel function [15]. Figure 4.10 shows the plot of

one and two dimensional Kaiser-Bessel functions.
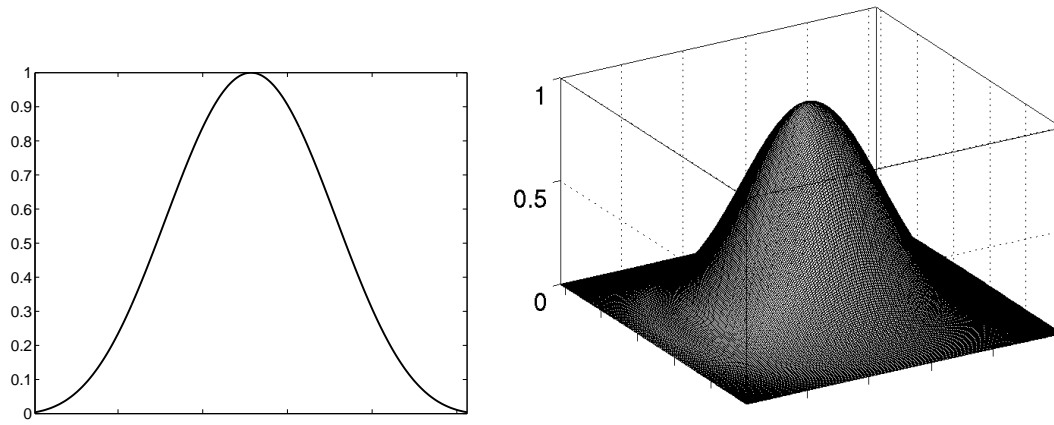
(a) 1D Kaiser-Bessel kernel
(b) 2D Kaiser-Bessel kernel

Figure 4.10: Kaiser-Bessel interpolation kernel. $\beta = 7.4302$.

The value of interpolation coefficients decrease with the distance. Figure 4.11 shows an example of all the sorted coefficients in T. It can be seen from this specific example that with maximum coefficient value as 1, there are about 20% of the values are smaller than 0.01.

Larger kernel width J can improve the reconstructed image quality [15, 19]. But it also increases the number of non-zero coefficients JM. However, there are small coefficients values, as shown in figure 4.11, which have small impact on the interpolation. It is possible to eliminate these small coefficients without large sacrifice on the image quality. Figure 4.12 shows reconstructed 2D image with kernel width 4 and 2. The image size is 256×256. The total number of k-space samples is 32768.
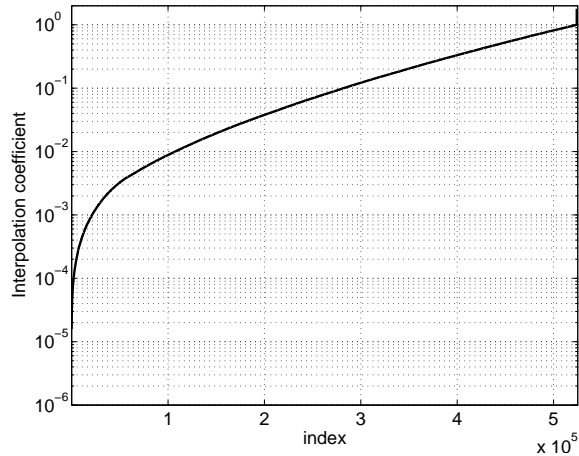
Figure 4.11: Interpolation coefficients.

With width 4 along x and y dimension, the total non-zero interpolation coefficients is 524288. For width 2 this number is 131072. The RMS error of the reconstructed images after 40 iterations are 0.0218 and 0.0241, respectively. If eliminating 36% of the coefficients with small values, the RMSE changes to 0.0220, which is only 1% more compared with the case of no elimination.

4.2 Implementation

The methods proposed in the previous sections were tested using computer simulations. Three type of sampling trajectories were used. Stack of spiral (SS) and radial (RAD) are the same as in chapter 3. The third sampling pattern is stack of spiral with variable rotations (SSv). It is similar to the stack of spiral trajectory. But the number of spirals on each stack is different. From bottom to top the numbers are 4 6 8 8 8 8 6 4. This trajectory already reduces some samples at high frequency locations in k-space. The corresponding image resolution is also $128 \times 128 \times 8$.

(a)   (b)   (c)

(d)   (e)   (f)
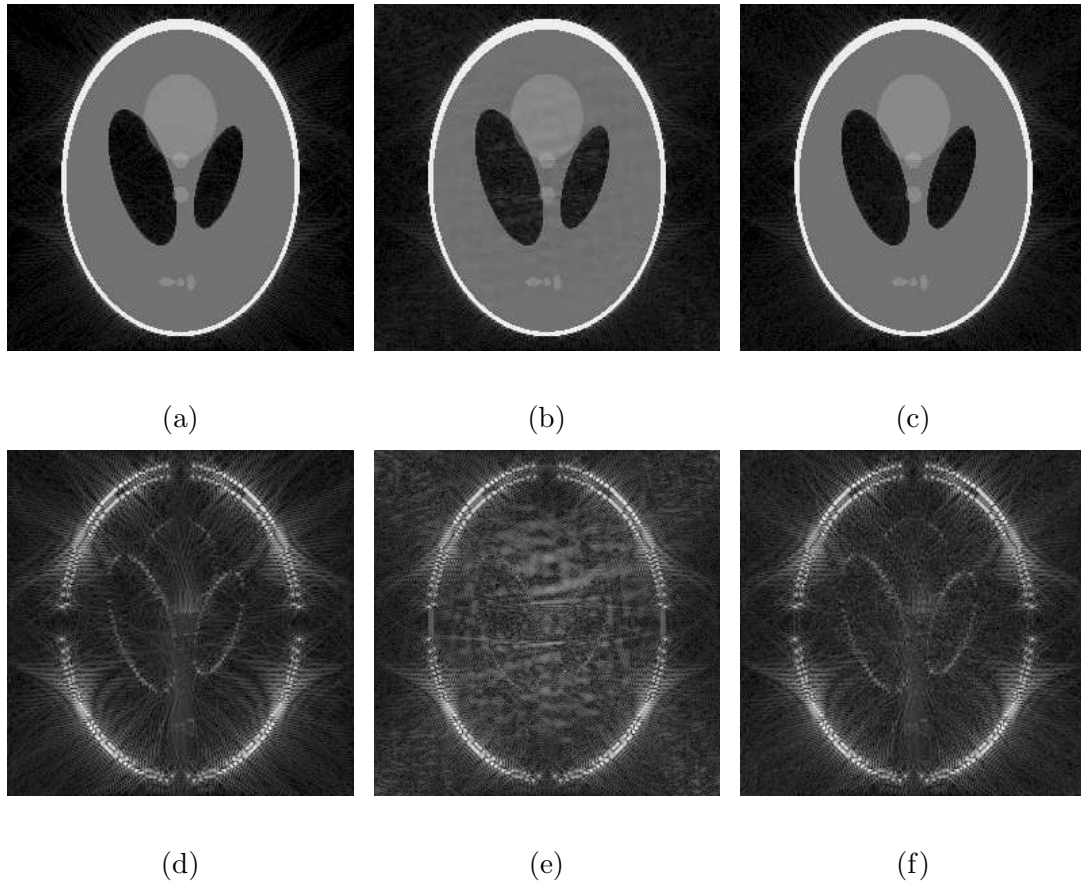
Figure 4.12: Reconstructed image and the difference with phantom using different interpolations. Left column: Kaiser-Bessel kernel with width 4. Middle column: Kaiser-Bessel kernel with width 2. Right column: Kaiser-Bessel kernel with width 4, 36% small values are eliminated. The contrast of the images were adjusted.
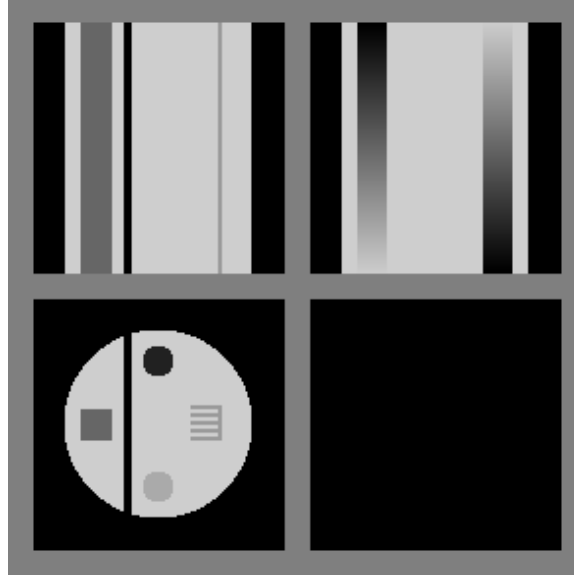
Figure 4.13: 3D cylinder phantom. The 3 sub-images are x-y, x-z and y-z section images.

Two numerical phantom were generated for simulation: a 3D modified Shepp-Logan phantom [56] as used in the previous chapter, and a 3D cylinder phantom with circle, square, line, comb shapes as shown in figure 4.13. Gaussian noise with $\sigma = 0.03$ and $\sigma = 0.06$ were added to the phantoms.

Each of the methods mentioned in previous sections were tested separately. RMSE between the reconstructed image and noise free phantom was used to evaluate the performance. It was compared with that from conventional iterative SENSE plus gridding reconstruction. Step-ratio method was used to the estimate penalty coefficient for edge-preserving penalty and object constraint penalty. To evaluate the performance of step-ratio, the result was compared with reconstructions using a wide range of manually selected penalty coefficients.

Three oversampling ratio values $1.75, 1.5, 1.25$ were used along all x, y and z dimensions for the two spiral patterns. For radial pattern, 1.125 and 1.0625 were also evaluated. Interpolation kernel is still Kaiser-Bessel. The β value was chosen from reference [26] for the corresponding oversampling ratios.

Interpolation coefficient matrix compression ratio from 0.1 to 0.7 were evaluated, which means removing 10% to 70% of samll coefficients.

Starting point of the iterations was chosen as zero-image [74]. Stop criteria was a pre-defined number of iterations [75]. For this simulation, a number 40 was used. This is manually verified to yield a reconstruction with no obvious alias or artifact.

A four channel coil and an eight channel coil were simulated. Reduction factor was 2 for the 4-coil configuration, and 4, 6 and 8 for the 8-coil. Coil sensitivity profile was re-calculated using the interpolation-extrapolation method to simulate the real MR data reconstruction case.

In the implementation of calculating edge-preserving penalty, the step-ratio was applied from the 10th iteration with a starting coefficient 0.01 till the 40th iteration. For object support coefficient calculation, it was applied at the 3rd iteration. The step-ratio threshold value was set to 1 in all three sampling trajectory simulations.

(a) SS Shepp-Logan phantom

(b) SS cylinder phantom

(c) SSv Shepp-Logan phantom

(d) SSv cylinder phantom
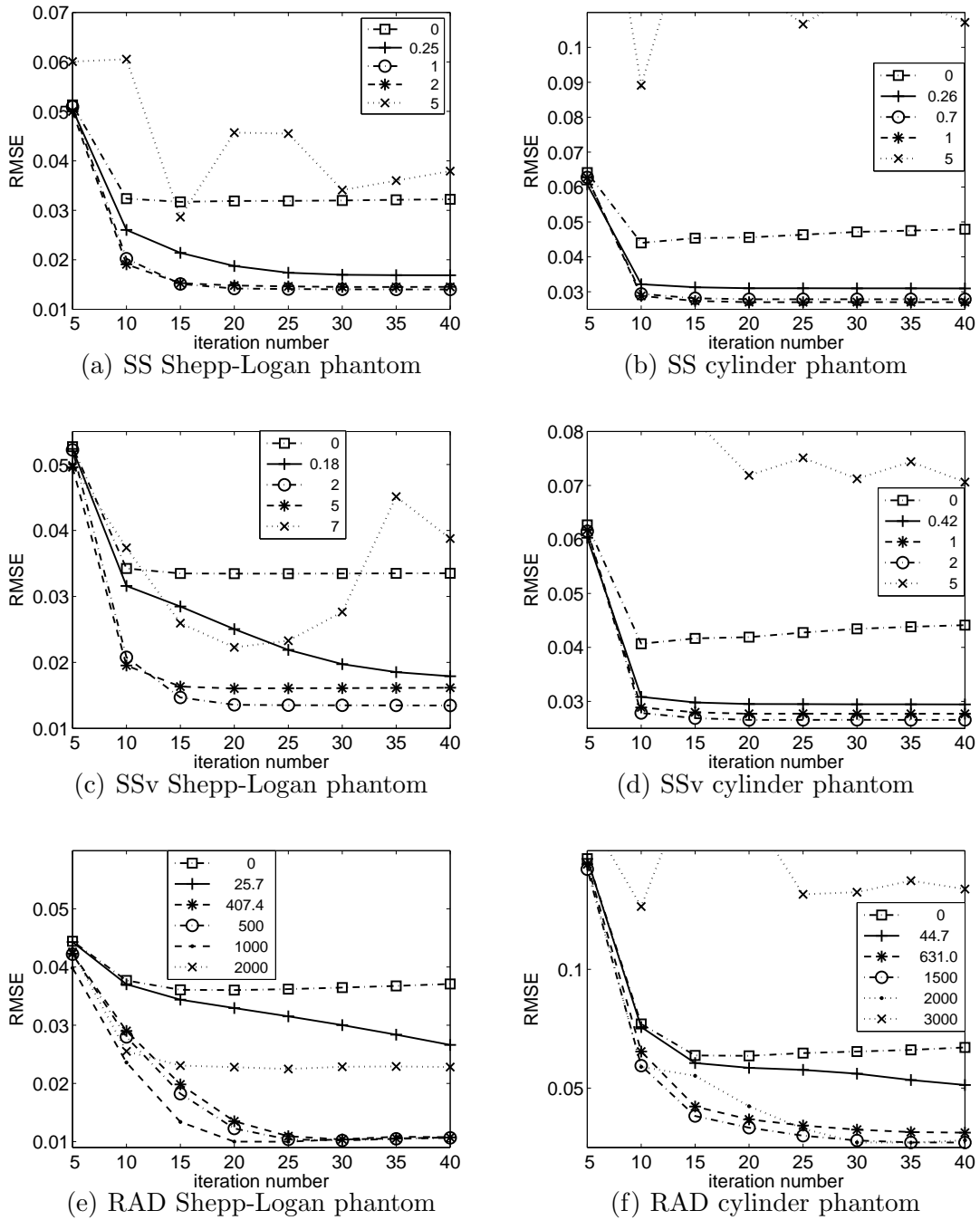
(e) RAD Shepp-Logan phantom

(f) RAD cylinder phantom

Figure 4.14: RMSE of gridding with and without edge penalty. The solid line with '+' marker is the one calculated with step-ratio value 1. For radial trajectories, step-ratio 2 estimated coefficient is display as dashed line with '*' shaped markers.

4.3   Results

Figure 4.14 shows the RMSE value of the edge preserving penalty reconstructions. An image mask was applied in RMSE calculation to use only those voxels on image, not in background. The image mask was manually calculate by thresholding the phantom image followed by hole fillings. An example is shown in figure 4.15(a). Each curve in the image corresponds to one regularization coefficient. Coefficient 0 denotes no regularization. Note that RMSE improves with the increase of coefficient starting from 0. Then after a certain value, when the coefficient increases, RMSE degrades, which can be even worse than the no regularization case. This is due to over-smoothing. Note that for the SSv data (middle row), penalty coefficient value 5 on the Shepp-Logan phantom (left) yields good RMSE results compared with no penalty, while on the cylinder phantom (right) the RMSE is much larger, denoting over-smoothing. This demonstrates that penalty coefficients obtained from one data or one simulation is not always suitable for other data. The calculated coefficient yields good RMSE value for all the simulations. For radial trajectories, the RMSE improvement from penalty coefficient using step-ratio threshold value 1 is not too much. The RMSE curve is not converged yet at 40 iterations. The performance using coefficient from step-ratio threshold value 2 is also shown in the figures. In this case the RMSE improvement is much better, with close performance to the best manually selected coefficient. Note that for the un-penalized case (with coefficient 0), the RMSE value slightly increases after certain iterations. For example, in figure 4.14(f), minimum RMSE occurs at iteration 15. Iteration 20 and later have larger RMSEs.

For the two stack of spiral cases, the neighbor points is set to 4 in $x - y$ plane, and 0 along z because slice distance along z dimension is much larger than the point distance in $x - y$ plane. For the radial sampling data, neighbor points are set to 4 for $x - y$ and 2 for z. Huber potential function was used to compute the penalty.

The effect of object support is evaluated using image RMSE and background RMSE. The background mask is defined as the difference of FOV mask and the image mask. An example is shown in figure 4.15(b).

(a) Image mask   (b) Background mask

Figure 4.15: Image mask and background mask for evaluating object support penalty. Pixels in the white area are used in RMSE calculation.

Figure 4.16 shows the RMSE value of the image part and background part using object support penalty on 3D simulated image reconstructions. For the two spiral patterns, RMSE was calculated at the 15th iterations. The number 15 was chosen based on the fact that the reconstruction converges to a reasonable result for
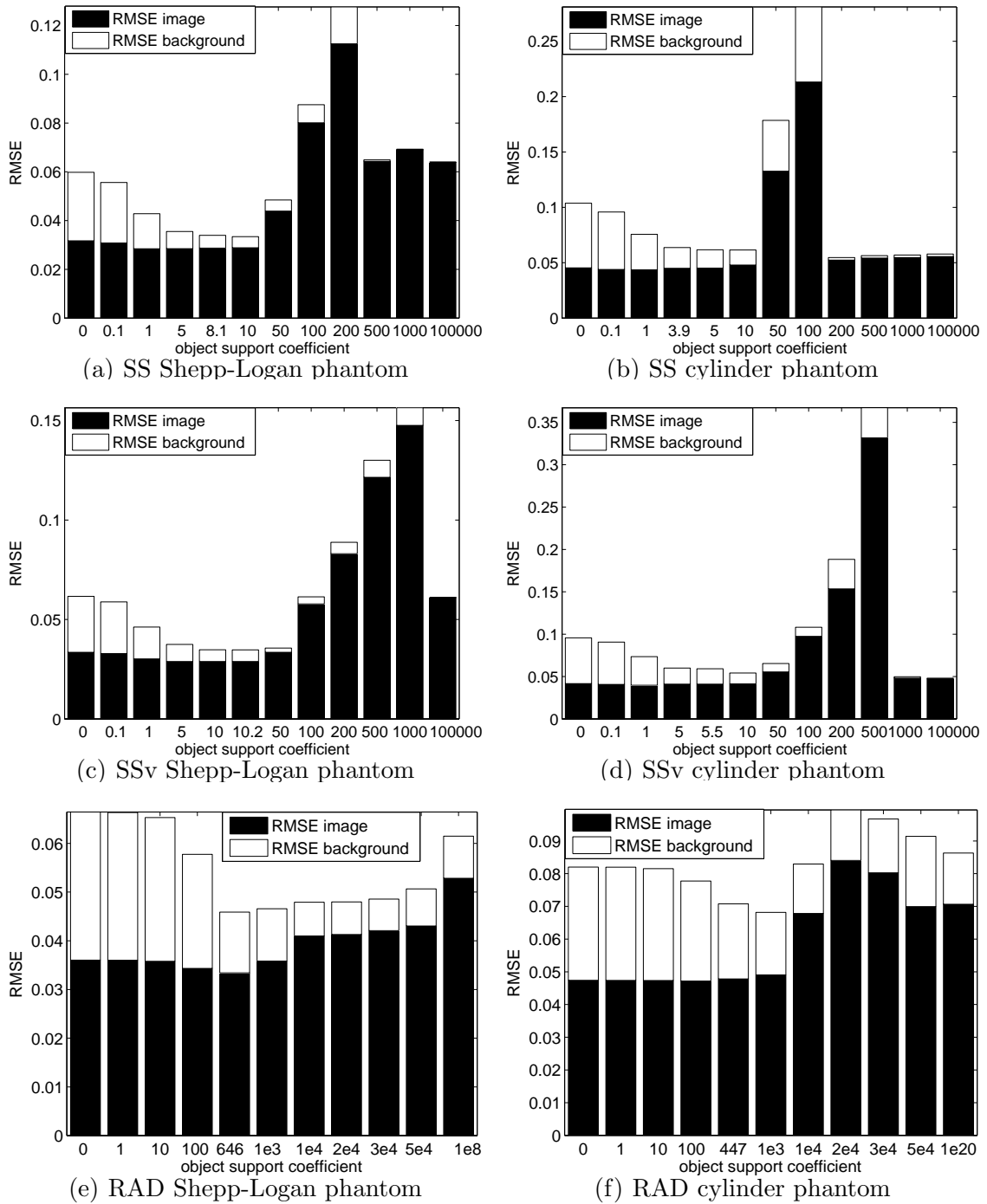
Figure 4.16: RMSE of image part and background part using object support. The calculated coefficients for each case are: (a) 8.1. (b) 3.9. (c) 10.2. (d) 5.5. (e) 646. (f) 447.

the unpenalized case. RMSE began to increase after this iteration. For radial data, RMSE was calculated at the 20th iteration. The image part RMSE was calculated on all voxels inside of image mask, which is obtained by manually thresholding the phantoms followed by hole filling operation. Background RMSE was calculated on all voxels in background, which contained all voxels inside of FOV but outside of image mask. Step-ratio threshold was set to 1.

The figure shows that without object support penalty (coefficient equals 0), there are certain image and background RMSE values for each case. For the spiral data, with the coefficient increases, the trend of background RMSE first is decreasing, increasing, and then decreasing again. With very large coefficient (for example, 100000), the background RMSE drops to nearly 0, which denotes clean background without noise. This is similar to the operation to set every voxel outside of object mask to 0. Although it yields noise free background, the image has a sharp truncation around the object mask. The image part RMSE may also be higher than the case without using object support penalty (figure 4.16(a) and 4.16(c)). For the radial data, extremely large coefficient does not completely eliminate background noise. The remaining RMSE is caused by the difference between the calculated object mask and the manually segmented image mask. Note for the radial data, image part RMSE are larger even with extremely large coefficient. Using the calculated coefficient from the step-ratio method, the background RMSE is reduced with comparable or smaller image part RMSE.

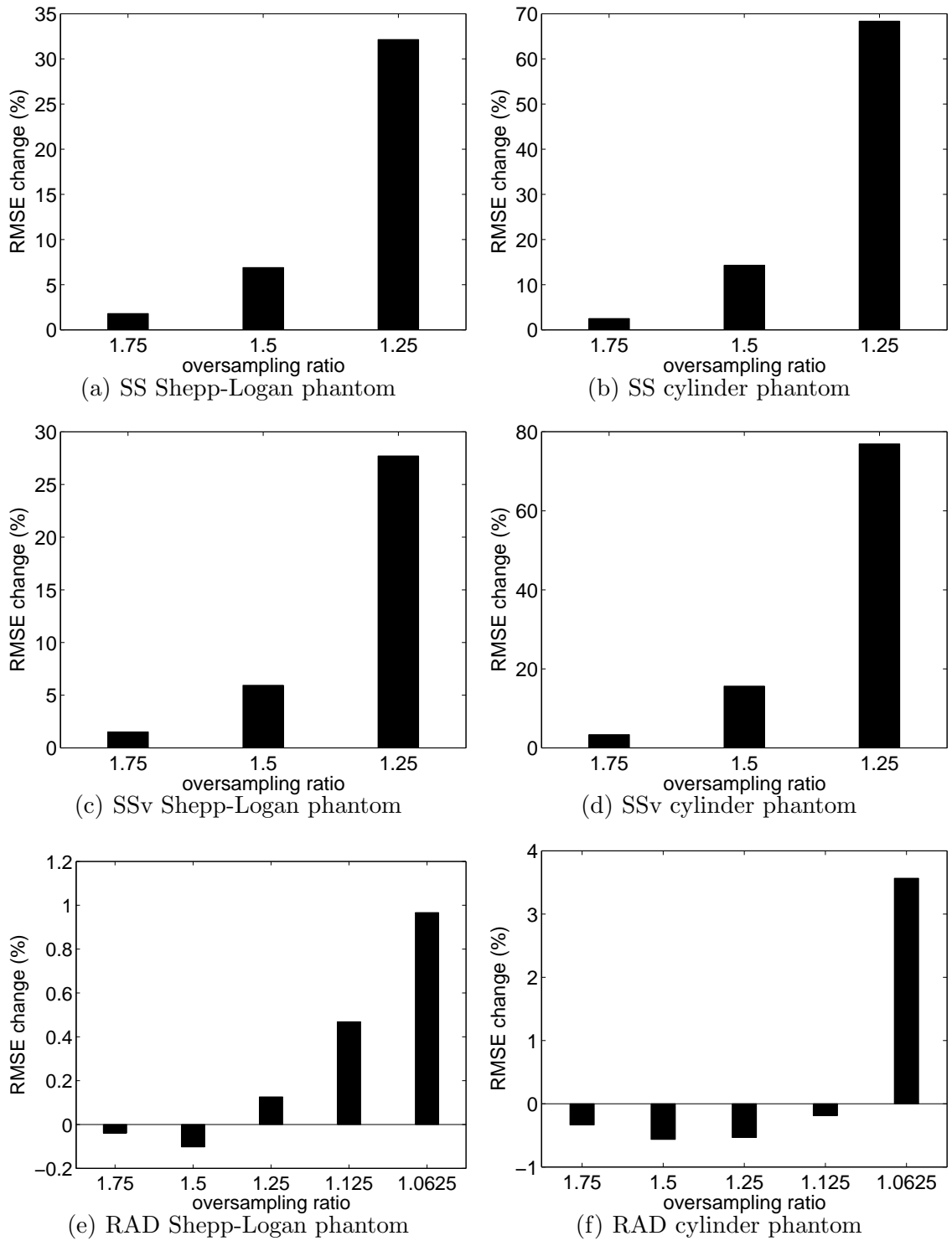Figure 4.17 shows RMSE changes (percent) of different oversampling ratio

Figure 4.17: RMSE of different reconstruction grid size. Relative to RMSE from 2x grid.

relative to 2x grid at the iteration with minimal RMSE. The corresponding iteration for each oversampling ratio is summarized in table 4.2. Manually calculated image mask was also applied so that background noise does not affect RMSE values.

For the two stack of spiral trajectories, 1.75x grid size already yields RMSE increase of $1\% - 4\%$ compared to 2x grid. For radial samples, however, smaller grid size yields reduced RMSE at 1.5x. Even at 1.125x, the RMSE increase is leas than 0.5%. Note that smaller oversampling ratio typically requires more iterations to converge in the sense of minimal RMSE.

	2x	1.75x	1.5x	1.25x	1.125x	1.0625x
SS Shepp-Logan phantom	15	15	20	35		
SS cylinder phantom	10	10	15	25		
SSv Shepp-Logan phantom	20	25	30	25		
SSv cylinder phantom	10	10	10	15		
RAD Shepp-Logan phantom	20	20	20	30	45	75
RAD cylinder phantom	20	20	20	30	45	60

Table 4.2: Iteration number for each oversampling ratio.

Figure 4.18 shows the RMSE change of different compressing ratio of interpolation coefficient matrix on 3D simulated image reconstructions. The bars are relative RMSE change relative to that from uncompressed coefficient matrix. The RMSE val-
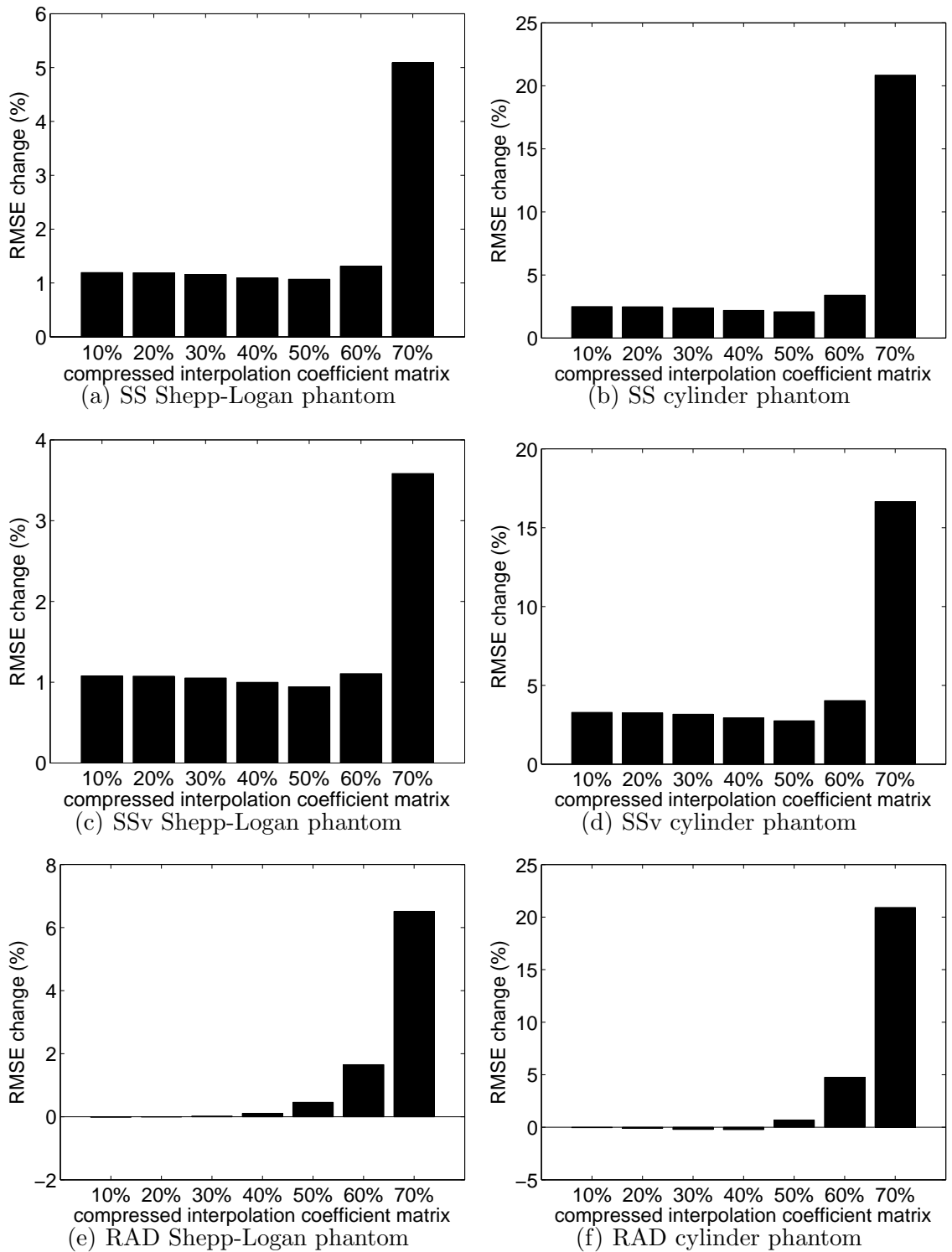
Figure 4.18: RMSE of different interpolation coefficient matrix compression. Relative to RMSE without compression.

ues were compared at 15 and 20 iterations for spiral and radial data, respectively. Compressing the interpolation coefficient matrix does not affect the convergence of iterations.

It is shown from the figures that the effect of compressing the coefficient is also data dependent. For the two stack of spiral trajectories, compression of up to 50% causes RMSE to increase about $1-3\%$. For radial trajectories, compressing 50% only increase RMSE by less than 1%. At 60% compression, the RMSE is increased by $2-5\%$.

An eight channel phased array coil was simulated to test the performance of larger reduction factor cases. The 8 coils were evenly distributed around the object parallel to z direction. Figure 4.19 shows the sensitivity profile in one $x-y$ plane. The sensitivity profile was recalculated using the extrapolation-interpolation method [13].

With eight coils, the reduction factor can be as large as 8 in theory [13]. This section focuses on higher values of 4, 6 and 8. 3D modified Shepp-Logan phantom with added noise was used. Simulations using two types of sampling patterns were performed: stack of spiral and radial trajectory as in the previous section.

For stack of spiral trajectory, reduction factor of 8 is not practically applicable. Strong aliasing artifacts remained in the reconstructed image. So only the results from reduction of 4 are shown, which is archived by keeping 2 spiral rotations from each z level. The reduction was done as follows: for the first z level, keep the first and fifth spiral rotation; for the second level, keep the second and the sixth rotations, and so on.
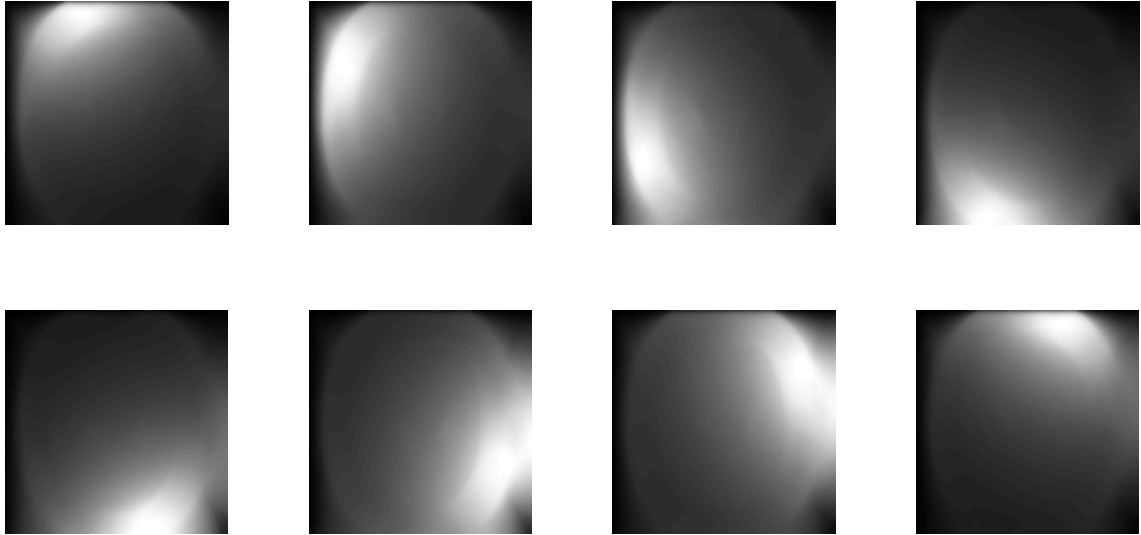
Figure 4.19: Simulated sensitivity profile in $x - y$ plane of of an eight channel phased array coil. Each sub image represents one coil.

For radial trajectory, reduction factor of 4, 6 and 8 were simulated by keeping one of every four, six and eight half radial lines.

Figure 4.20 illustrates the RMSE of reconstructions with different edge preserving penalty coefficients. Similar to the 4 coil case, this penalty reduces RMSE. The performance of coefficient calculated using the step-ratio method is close to the best RMSE.

Figure 4.21 is the RMSE of image part and background part with different object support penalty coefficients. Step-ratio threshold was set to 1. Penalties were applied from the third iteration for the stack of spiral data and radial data with reduction factor of 4 and 6. For radial data with reduction factor of 8, penalty was applied from the 5th iteration to skip a large step change between iteration 4 and
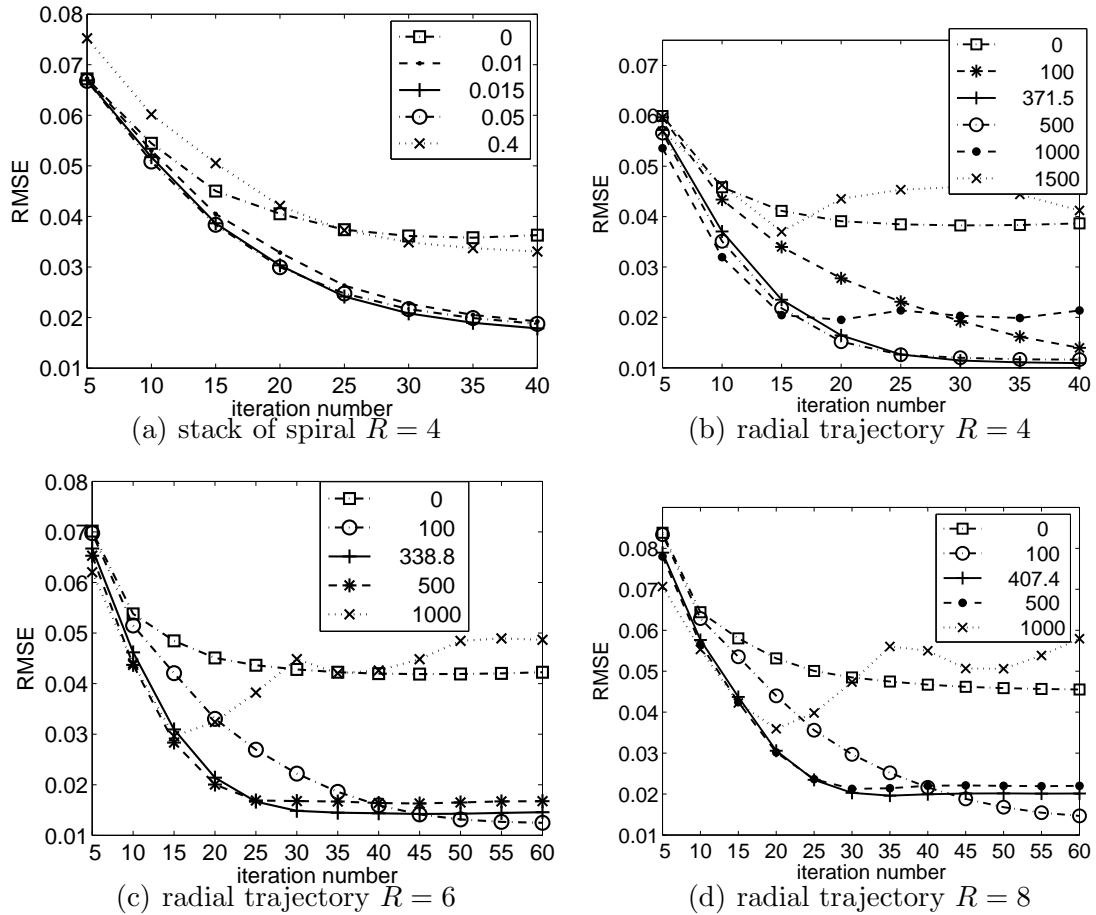
Figure 4.20: RMSE of reconstructions with and without edge penalty. The solid line with "'+'" marker is the result using smoothing penalty with calculated coefficient, where step-ratio threshold is set to 1 for stack of spiral, and 2 for radial pattern.

(a) stack of spiral $R = 4$

(b) radial trajectory $R = 4$

(c) radial trajectory $R = 6$

(d) radial trajectory $R = 8$

Figure 4.21: RMSE of image part and background part using object support. The iterations and calculated coefficients for each case are: (a) iteration = 40, coefficient = 0.49. (b) iteration = 30, coefficient = 339. (c) iteration = 50, coefficient = 234. (d) iteration = 80, coefficient = 63.

5. The number of iterations were chosen based on the rule of no visible alias in the unpenalized reconstructions. The figure shows similar trend as in the 4 channel coil case. For stack of spiral data, very large coefficient results in zero background noise with comparable image RMSE. For the three radial data at different reduction factors, large coefficient does not completely remove background noise. This is also caused by the difference of calculate object mask and the manually segmented image mask. In all cases, the coefficients calculated using the step-ratio method reduced background RMSE with comparable image RMSE.

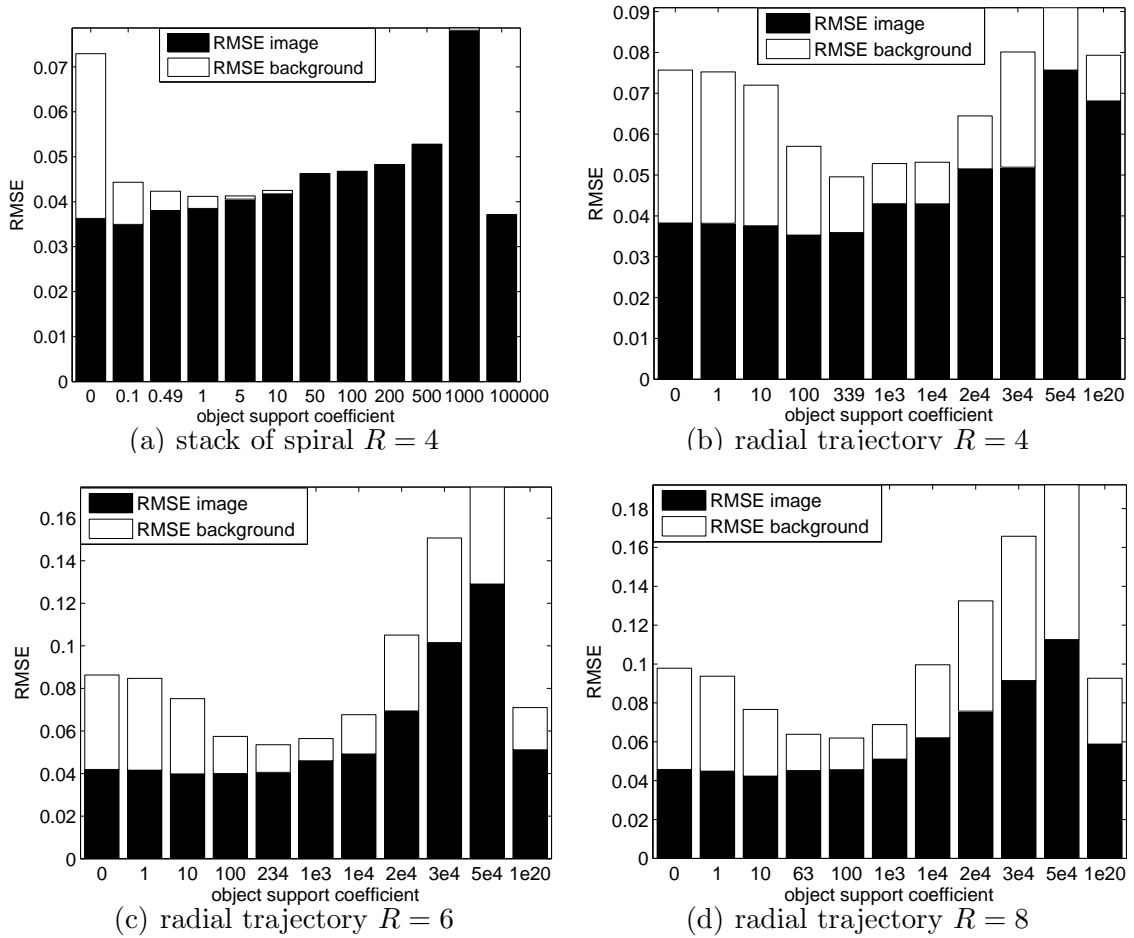RMSE with different oversampling ratios are shown in figure 4.22. Similar to the four coil case, stack of spiral data always have larger RMSE values at smaller oversampling ratios. While in the radial data, using 1.125x oversampling ratio increases less than 1% of RMSE comparing to the case of 2x. The number of iterations at each oversampling ratio are summarized in table 4.3.

	2x	1.75x	1.5x	1.25x	1.125x	1.0625x
stack of spiral $R = 4$	35	35	40	40		
radial $R = 4$	30	35	35	40	75	80
radial $R = 6$	45	50	55	60	105	120
radial $R = 8$	65	65	70	80	120	120

Table 4.3: Iteration number for each oversampling ratio.

(a) stack of spiral $R = 4$

(b) radial trajectory $R = 4$

(c) radial trajectory $R = 6$

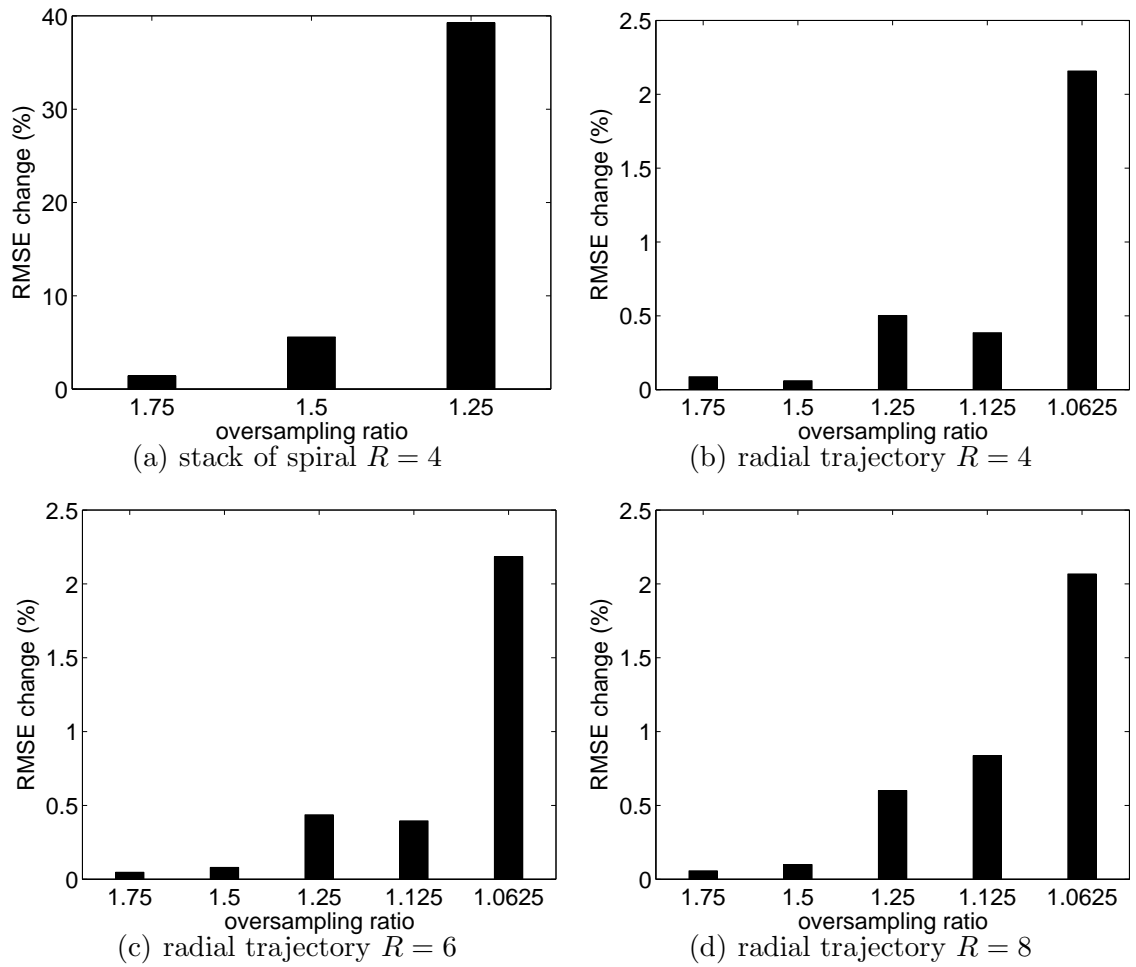(d) radial trajectory $R = 8$

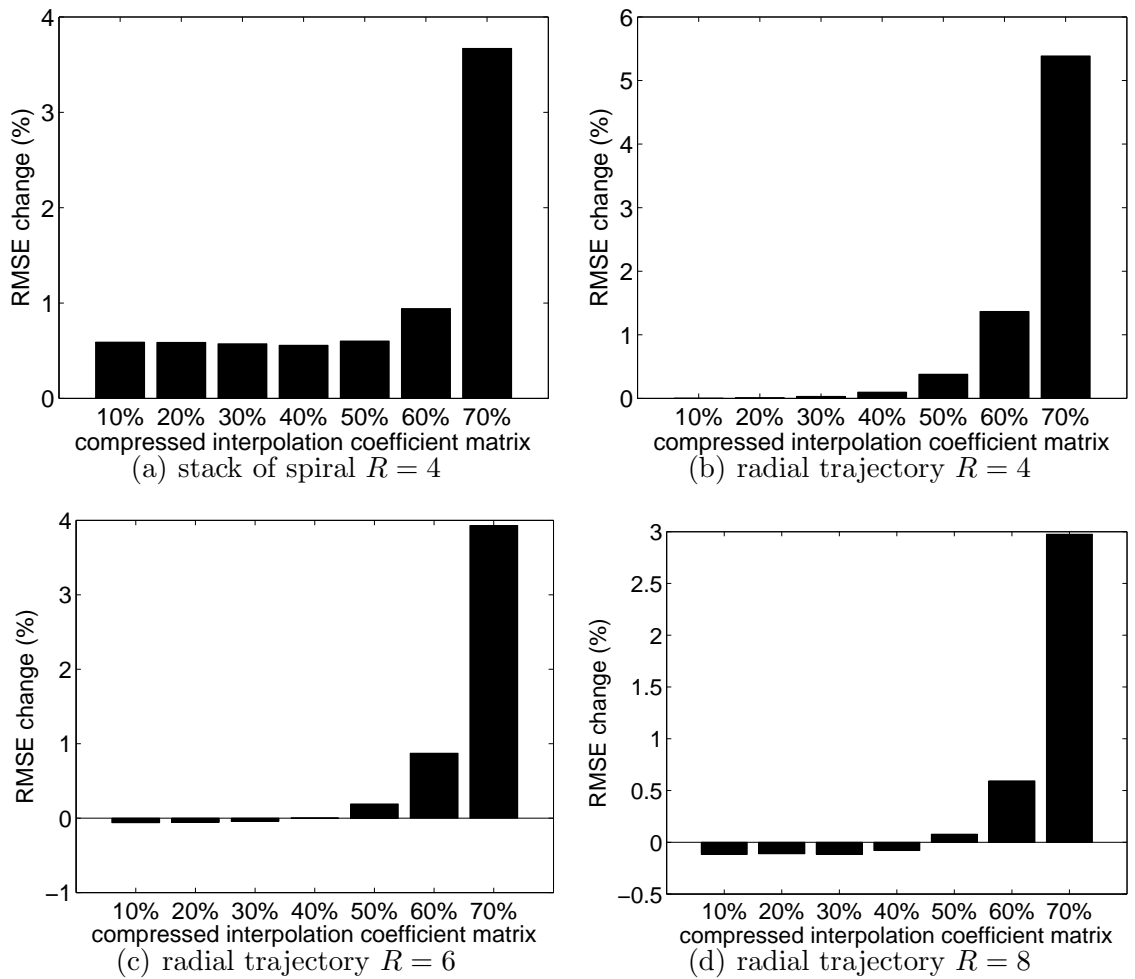Figure 4.22: RMSE of different oversampling ratio.

Figure 4.23: RMSE of different interpolation coefficient matrix compression.

The results of compressing the interpolation coefficient matrix are shown in figure 4.23. For all four cases, removing 50 percent of small coefficient only increase RMSE by less than 1 percent.

4.4 Discussion

Edge preserving penalty helps to smooth the reconstruction with smaller image RMSE relative to the phantom. Object support helps to reduce background noise. The penalty coefficients calculated using the step-ratio method yield good reconstruction in the sense of RMSE for edge-preserving and object support penalty. The value 1 is suitable for the two stack of spiral trajectories. Value 1 and 2 are suitable for radial trajectories. Larger step-ratio threshold tends to yield larger penalty coefficient values.

Using smaller oversampling ratio and interpolation kernel parameters from reference [26] in radial trajectory reduces RMSE. Considering 1.125x only increases the RMSE values of the reconstruction by less than 1%, while using it on 3D data can reduce the computation and memory requirement to less than 1/5 compared to the 2x case. This factor is chosen for radial trajectories. For the two stack of spirals, because smaller oversampling ratio increases RMSE, and the data size is not too big, original 2x oversampling ratio will be used.

In the case of compressing the interpolation coefficient, with 50% compression corresponds to RMSE increase of about 1%−2%. The interpolation coefficient mattrix is ofen pre-computed and stored on disk to be used later for the same sampling

trajectory and image grid size. So 50% compression is used for all sampling patterns. The little RMSE increase could be compensated by the edge-perserving smoothing penalty and object constraint penalty.

CHAPTER 5
NON-CARTESIAN PARALLEL MRI RECONSTRUCTION METHOD

5.1   Method

5.1.1   Objective Function

Based on the analysis and computer simulations from the previous chapters, the reconstruction of three-dimensional non-Cartesian parallel MRI problem is to solve the following objective function

$$\psi(x) = ||b - Ex||^2 + \lambda_1 \frac{1}{2} \sum_j \sum_{k \in C} w_{jk} \psi_{huber}(x_j - x_k, \delta) + \lambda_2 x(I - diag(S))x \quad (5.1)$$

where E is encoding matrix defined in equation 3.12 with smaller values removed. Huber function ψ_{huber} is defined in table 4.1. δ is a Huber function parameter related to noise level in image. S is the object mask. I denotes Identity matrix. λ_1 and λ_2 are two penalty coefficients obtained using the step-ratio method introduced in section 4.1.2.

5.1.2   Image Quality Evaluation

The image quality of the reconstructed image is an important factor to evaluate reconstruction methods. The reconstruction from non-Cartesian samples introduces aliasing artifacts, for both parallel and non-parallel imaging, a poor reconstruction will have the alias, blurring or noisy regions remained in the final image. A direct image quality comparison method is to display all reconstruction images side by side to the human reviewer for visual comparison [13, 47, 55, 75–85]. The region of

interest (ROI) on the images are often enlarged for better visualization. It is efficient to identify the "bad" images among all reconstructions that contain large alias or strong noise amplification. However, this is not a quantitative criterion. Different inspectors may have different opinions among the reconstructions. This is also used when determining the number of iterations to select the smallest iteration that has no visible alias artifact.

Numerical comparisons are quantitative evaluation method. It can be separated into two main groups depending on the data source: computer simulation and *in vivo* data.

For computer simulations, the original numerical phantom image is available and is used to calculate simulated k-space data. So it is used as the standard to compare with the reconstructed images. RMSE calculated between the images is a widely used criterion [51, 54, 55, 77, 80, 85–89].

For *in vivo* MR data reconstructions, however, there is no one method to be accepted as the gold standard. Varies criteria are proposed and investigated in recent literatures [13, 69, 74, 75, 83, 84, 89–93].

5.1.2.1 Aliased Energy

Jackson *et al* [15] calculated aliased energy in the image based on the reconstruction method as an error term to denote image quality. Betty *et al* [26] adopted similar method. In both cases quantitative equations are derived such that accurate error terms can be obtained. This error term focuses on the impact of interpolation

kernel. There is not such quantitative equations for parallel imaging yet, which needs to take into account the impact of data noise and coil sensitivity maps.

5.1.2.2 RMSE

RMSE is also a widely used criterion in evaluating MR data reconstruction. The definition is shown in equation 3.24. However, in MR reconstruction, the true image is not available. An acceptable substitution is the body coil reference image [84, 93, 94]. Since this reference image also contains noise and other imperfections, the RMSE may not show the true image errors.

5.1.2.3 Similarity Measurement

These metrics evaluate the quality of the reconstructed image in terms of similarity with the reference image, for example, reference scan from body coil. Two terms in this category are joint entropy (JE, less is better) and normalized mutual information (NMI, more is better) [93]. The terms are calculated as follows:

Joint entropy

$$H(X,Y) = -\sum_{x,y} p(x,y) \log_2(p(x,y)) \tag{5.2}$$

where X and Y are two images, $p(x,y)$ is joint probability.

Mutual information

$$I(X;Y) = \sum_{y \in Y} \sum_{x \in X} p(x,y) \log \left(\frac{p(x,y)}{p_1(x)\, p_2(y)} \right) \tag{5.3}$$

where p_1 and p_2 are marginal probability.

5.1.2.4   ROI SNR

The ROI SNR is calculated from manually selected ROIs from the reconstructed image [89, 90], which is useful to evaluate noise amplifications. Several (2-5) small ROIs at relatively smooth regions in the image are manually defined. The mean and standard deviation are used to represent signal and noise. Larger ROI SNR denotes better image quality in the sense of less noise amplification. The disadvantage is that the value is dependent on the location of ROIs.

5.1.2.5   SNR from Two Scans

Another quantitative criterion for evaluating the reconstructed image quality is to compute image SNR from two separate scans of the same object [69, 91, 92, 95]. The signal from the object are assumed to remain the same, while the random noise content in the signal varies from scan to scan. Using the same reconstruction method can obtain two separate images. The sum and difference of these two images are then calculated, which are used to determine the "signal" and "noise" in the images. Specifically, the signal of a local voxel is calculated by averaging the neighboring voxels in the sum image. A 5×5 windows is used by Raj *et al*, which produces acceptable results [69]. The standard deviation of noise is obtained using the voxels in the difference image between the same local window. Then the SNR is defined as

$$SNR = \frac{mean(I_{sum})}{\sqrt{(2)}std(I_{diff})} \qquad (5.4)$$

where I_{sum} and I_{diff} are the sum and difference of the two images over a local window. This result is comparable across different reconstruction methods [69, 96].

To obtain the two data set, Reeder *et al* acquired two independent scans. This guarantees independent noise source. But may be erroneous because of object motion or other physiological effects change [92]. Raj *et al* used only one single scan and then manually added random noise in the k-space output to obtain the second data set. This may achieve the same noise purpose as the two scans does, the result may be affected by the intensity of the artificially added noise.

In this work a similar "two data" is used, where the two data come from one full sampled data by manually separating into under-sampled subsets. Each subset has the same noise statistics property, but different noise values. Object motion will not affect the two subsets. The windows size is chosen to be $5 \times 5 \times 1$ for the two spiral data, and $5 \times 5 \times 5$ for radial data. The mean SNR in the same ROIs defined in the ROI SNR method is used to represent the image SNR.

5.1.2.6   Summary

Based on the discussions above, visual inspection of the reconstruction is the fist step to check visible artifact or other errors. Th metrics that are used in evaluating the performance of the proposed method in later sections are: ROI SNR, two data SNR, background noise, RMSE, NMI and JE. The last three terms are calculated relative to body coil reference images. FOV mask and image mask are used to minimize the impact of background noise.

5.2   Implementation

All 25 parallel MR data in this section were acquired on a GE 1.5T LX scanner with a four channel phased array coil. A body coil reference data using the same sampling trajectory is also acquired for coil sensitivity map calculation.

5.2.1   Stack of Spiral Trajectory

There are a total of 5 stack of spiral trajectory data. All of the data contain 8 stacks along z direction.

SS 1 data were acquired on a watermelon object with FOV $28cm$ along x and y, $8cm$ along z, slice thickness $1cm$ and spacing 0. SS 2 were acquired on the same watermelon. The difference is that the FOV along z changed to $2.667cm$. Thus slice thickness is also reduced to 0.333. SS 3 were on a cantaloupe object, with FOV $28cm \times 28cm \times 8cm$, slice thickness $0.5cm$ and spacing $0.5cm$. SS 4 were on a watermelon object. The $x-y$ image is on the cross section. FOV is $28cm \times 28cm \times 4cm$, slice thickness is $0.5cm$ and spacing is 0. SS 5 were collected on a GE plastic cylinder phantom. FOV is $20cm \times 20cm \times 6.4cm$, Slice thickness $0.8cm$ and spacing 0.

The data are summarized in table 5.1.

5.2.2   Stack of Spiral Trajectory with
Variable Number of Rotations

This trajectory were used to obtain a total of 7 data set.

SSv 1 data were acquired on the ankle of a human volunteer. FOV is $20cm$ along x and y, and $4cm$ along z. Slice thickness is $0.5cm$ and spacing is 0. SSv 2

data	object	rotations	FOV x-y (cm)	FOV z (cm)	thickness (cm)	spacing (cm)
SS 1	watermelon	8	28	8	1	0
SS 2	watermelon	8	28	2.667	0.333	0
SS 3	cantaloupe	8	28	8	0.5	0.5
SS 4	water melon	8	28	4	0.5	0
SS 5	GE phantom	8	20	6.4	0.8	0

Table 5.1: Stack of spiral data set

were again on the GE phantom, with FOV $20cm \times 20cm \times 4cm$. Slice thickness is 0.5cm. Spacing is 0. SSv 3 and 4 were two scans with identical parameters collected on a human volunteer knee. FOV is $20cm \times 20cm \times 4cm$. Slice thickness is 0.5cm and spacing is 0. SSv 5 are the average of SSv 4 and 5. The average has the advantage of reducing noise, thus enhancing signal SNR and in turn enhancing reconstruction image quality. SSv 6 were also acquired at the same time as SSv 4 and 5. It was an independent scan with reduced number of spirals. The number of spiral rotations, from bottom slice to top, are 1, 3, 5, 5, 5, 5, 3 and 1, respectively. This is achieved by reducing 3 spiral rotations on each z level. The remaining rotations on each z level are evenly space. The effective reduction factor is 1.85. This data contain 2 under-sampled scans with the same parameters. This is a true two data scan. No further reduction is needed. SSv 7 were on a human volunteer brain. FOV is $24cm \times 24cm \times 4cm$. Slice thickness is 0.5cm and spacing is 0.

data	object	rotations	FOV x-y (cm)	FOV z (cm)	thickness (cm)	spacing (cm)
SSv 1	ankle	4,6,8,8,8,8,6,4	20	4	0.5	0
SSv 2	GE phantom	4,6,8,8,8,8,6,4	20	4	0.5	0
SSv 3	knee	4,6,8,8,8,8,6,4	20	4	0.5	0
SSv 4	knee	4,6,8,8,8,6,4	20	4	0.5	0
SSv 5	ave of 4 and 5	4,6,8,8,8,6,4	20	4	0.5	0
SSv 6	knee	1,3,5,5,5,5,3,1	20	4	0.5	0
SSv 7	brain	4,6,8,8,8,6,4	24	4	0.5	0

Table 5.2: Stack of spiral with variable number of rotations data set

The data are summarized in table 5.2.

5.2.3   Radial Trajectory

There are a total of 13 radial trajectory sampling data. The radial trajectory contains a total of 13106 radial lines evenly spaced to cover the entire 3D k-space. There are 128 valid points on each half radial line. The points have a spacing in k-space of $2.083m^{-1}$, which corresponds to a field of view of 48 cm. The 128 points on each half radial line corresponds to image size of 256 on each dimension. However, the true images occupies smaller number of points. To ease the computation burden, the image size is chosen to be 160 and 192.

Radial 1 was collected on the GE phantom object. Radial 2-6 were obtained

from the same GE phantom object, which contains 4 independent phased array coil scans. These scans were collected one by one without moving the object. The data are arranged as follows: Radial 2: phased array coil scan 1. Radial 3: phased array coil scan 2. Radial 4: phased array coil scan 3. Radial 5: phased array coil scan 4. Radial 6: use average of phased array coil 1 to 4 as phased array scan. Radial 7-13 were collected on a watermelon object. This data acquisition contained 2 independent body coil scans and 4 independent phased array coil scans. By averaging 2 and 4 of the phased array data, smoother data can be obtained to evaluate the performance of less noisy data. Radial 7: body coil reference scan 1 with phased array coil scan 1. Radial 8: body coil reference scan 1 with phased array coil scan 2. Radial 9: body coil reference scan 2 phased array coil scan 3. Radial 10: body coil reference scan 2 phased array coil scan 4. Radial 11: body coil reference scan 1 with odd numbered radial lines of phased array coil scan 1 and 2. Radial 12: body coil reference scan 2 with odd numbered radial lines of phased array coil scan 3 and 4. radial 13: use average of body coil reference scan 1 and 2 as body reference scan, and average of phased array coil 1 to 4 as phased array scan.

The data are summarized in table 5.3.

5.2.4   MR Data Pre-processing

Because both the body coil and phased array coil reference data acquired using non-Cartesian sampling trajectories, the reference images contain alias artifact outside the FOV. Typically the FOV size is large enough so that the images show no

data	object	comment
Radial 1	GE phantom	
Radial 2	GE phantom	array scan 1
Radial 3	GE phantom	array scan 2
Radial 4	GE phantom	array scan 3
Radial 5	GE phantom	array scan 4
Radial 6	GE phantom	average of array scan 1,2,3 and 4
Radial 7	water melon	body scan 1, array scan 1
Radial 8	water melon	body scan 1, array scan 2
Radial 9	water melon	body scan 2, array scan 3
Radial 10	water melon	body scan 2, array scan 4
Radial 11	water melon	body scan 1, average of array scan 1 and 2
Radial 12	water melon	body scan 2, average of array scan 3 and 4
Radial 13	water melon	average of body scan 1 and 2, average of array scan 1,2,3 and 4

Table 5.3: Radial trajectory data set

visible alias. For some of the data, the object size is very close to that of FOV. In other data the object is not in the center of FOV. Thus circular streak shaped alias exists in the reconstructed reference images around the object, which makes it difficult to calculate coil sensitivity map values because the alias will also be included in the calculation. A preprocessing step on the reference images to manually eliminate the alias is required. A cylinder shaped mask, i.e. stack of circles, is pre-calculated for the two spiral data. A sphere shaped mask is pre-calculated for the radial data.

<div align="center">5.2.5   Under Sampled Data and</div>

<div align="center">Reference Images</div>

The data acquired from MR scanners contain trajectories of full FOV, full resolutions scans (except data SSv 6). To achieve reduction factor of 2, each data set is split into 2 uncorrelated subset which are essentially acquired with the same object parameter but different noise values [85, 88].

For stack of spiral trajectories with 8 rotations on all z-level, the odd numbered 1,3,5,7 rotations of each level are assigned to subset 1, and even numbered 2,4,6,8 rotations are in subset 2. For stack of spiral trajectories with variable rotations of 4, 6 or 8, the corresponding odd numbered rotations, 1,3, 1,3,5 or 1,3,5,7 are assigned to subset 1. The corresponding even numbered rotations are assigned to subset 2. Both subsets have effective reduction factor of 2. One exception is SSv data 6, which is under-sampled with reduction factor of 1.85. For radial sampling trajectory data the radial lines are partitioned using a similar odd-even method. All the 4 array coil

dataset are split into two subsets to evaluate the reconstruction method performance. Each subset of data is reconstructed independently. The two subsets are used as the "two scans" SNR comparison.

Full resolution body reference image is reconstructed and used in RMSE, NMI and JE calculation.

5.2.6   Implementation Environment

Program in this section was implemented in Matlab version 7.7 (Mathworks, Natick, MA). Code was executed on a SuSE Linux version 11.3 server with an eight core Intel Xeon X5450 CPU at 3.00GHz. System memory is 16GB.

5.3   Results

The 25 data set mentioned in section 5.2 were reconstructed using the proposed method. Corresponding image quality metrics were calculated. For the two spiral data, the number of iterations for both conventional method and proposed method were set to 40. For radial data, 40 iterations were used for conventional method, while 80 were used for the proposed method due to the impact of smaller oversampling ratio as mentioned in the previous chapter.

Figure 5.1 shows reconstructed images from some of the MR data set, one from each sampling patterns. Reconstructions from the proposed method has smaller background noise due to object support penalty. Figure 5.1(b) and 5.1(c) also show that reconstructions from the proposed method are smoother while still preserves edges in image.
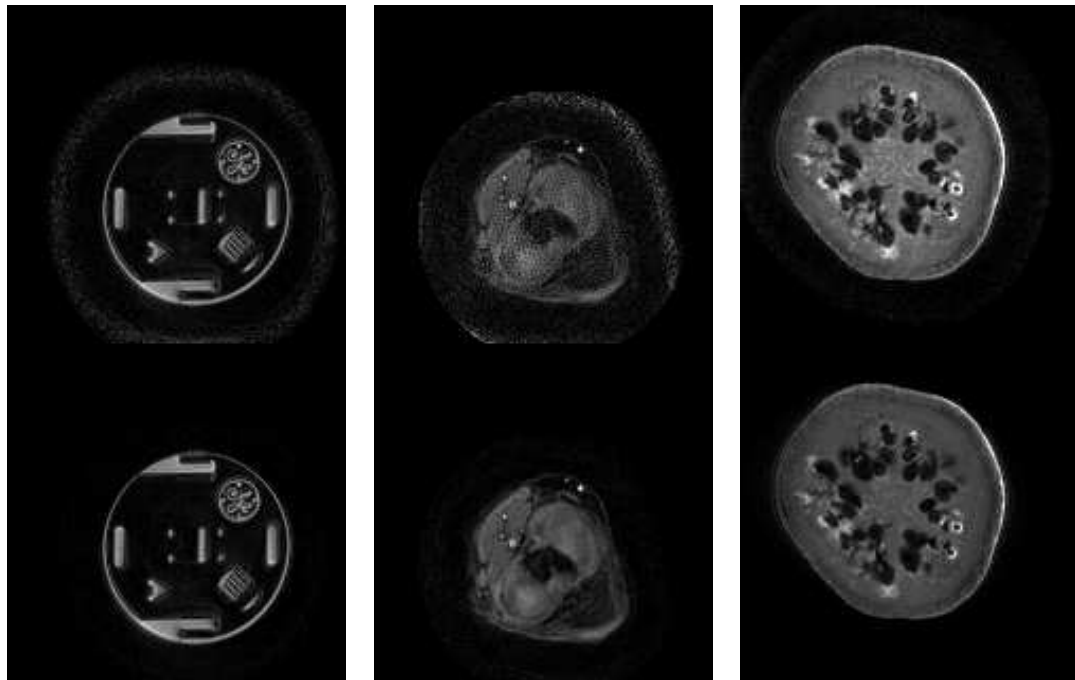
(a) SS 5   (b) SSv 3   (c) Rad 3

Figure 5.1: Reconstructed images. Top row: conventional method. Bottom row: proposed method with edge preserving penalty, object penalty, smaller oversampling ratio for radial data and compressed interpolation cooefficient matrix.

Figure 5.2 shows the RMSE of the proposed and conventional method. RMSE was calculated between reconstructed image and body coil reference image. Each data contains two subsets. A manually calculated image mask that only covers the true object with holes in object filled were applied to avoid the impact on background noise.

Since the body coil reference image is an approximation to the true image, the RMSE values are for qualitative performance evaluation only. The figures show that with edge preserving penalty, smaller oversampling ration and compressed interpolation coefficients, the RMSE of the proposed method are comparable to the conventional method.

Figure 5.3 and 5.4 are the NMI and JE metrics relative to body coil reference image. The proposed method show comparable results as the conventional method.

Figure 5.5 illustrates the ROI SNR results. The values are SNR change of the proposed method relative to conventional method. The two bars of each data represents the two subsets. It is shown in the figure that ROI SNR is greatly improved in the proposed method. This metric does not rely on reference image. But it is dependent on the ROI locations. Examples of some of the ROI definitions are shown in figure 5.6.

Figure 5.7 is the relative SNR derived using the two data mode. This SNR term from the proposed method is also greatly improved on all data set. Same ROI definitions as the ROI SNR case are used here to location SNR values.

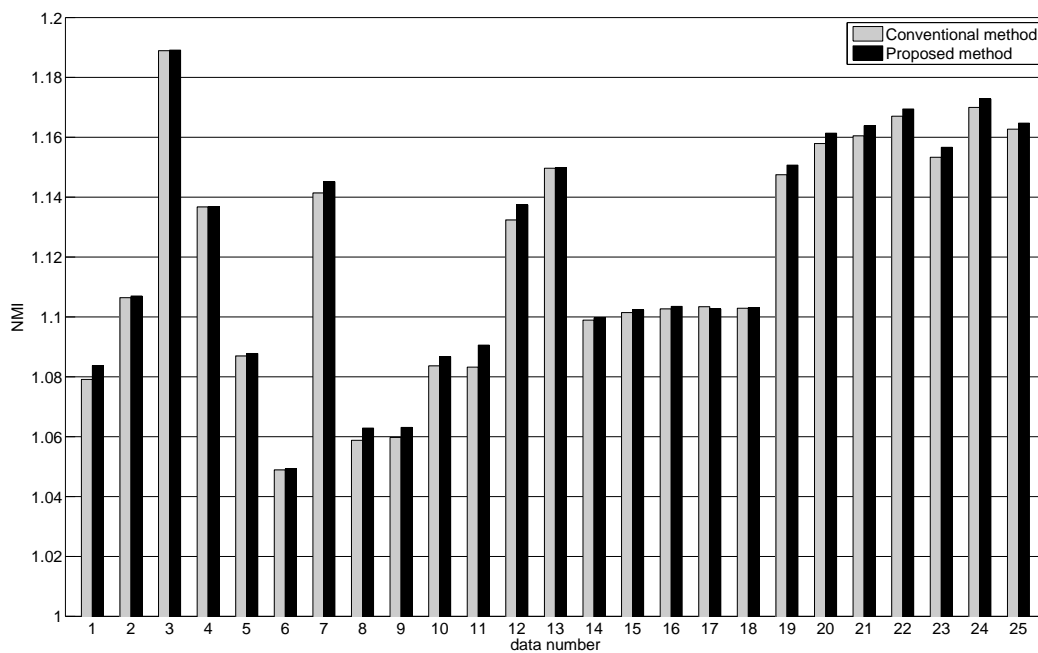Background noise from the proposed method and conventional method are
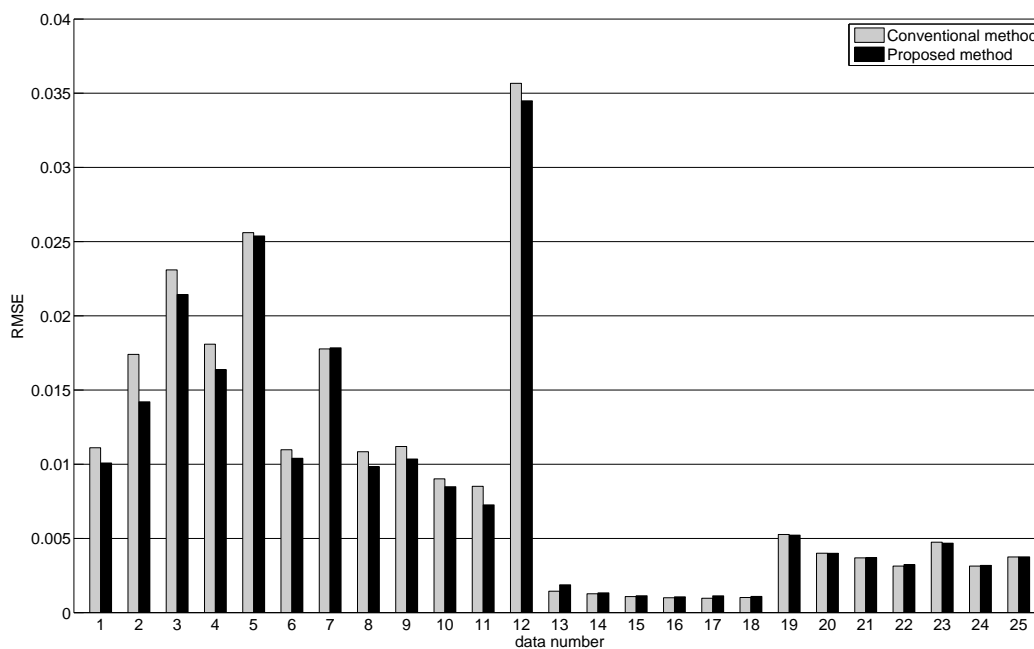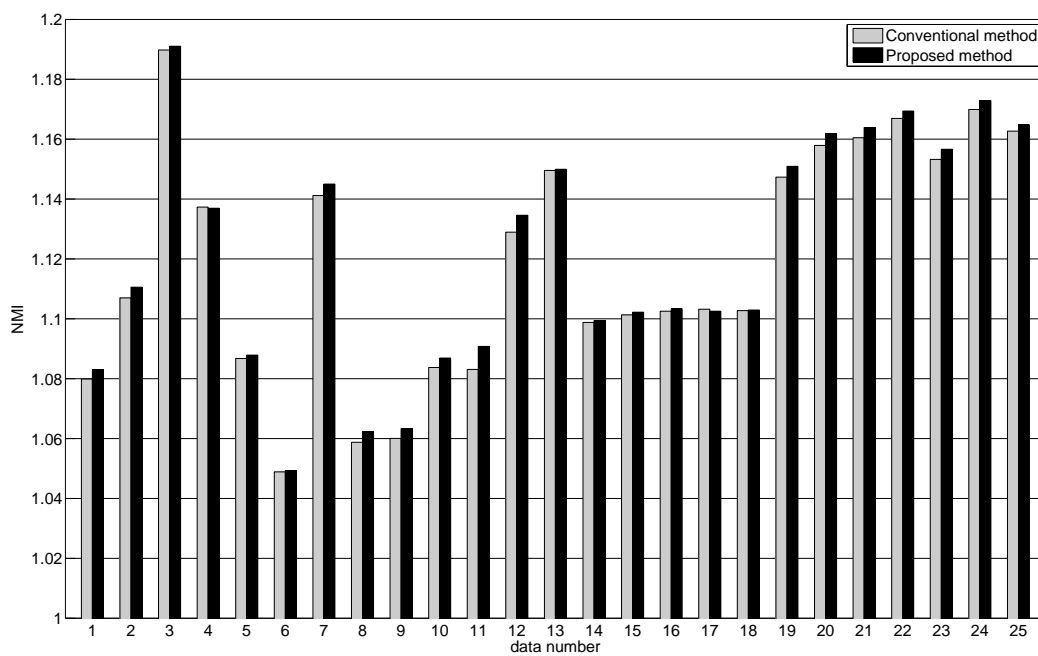
(a) RMSE Subset 1
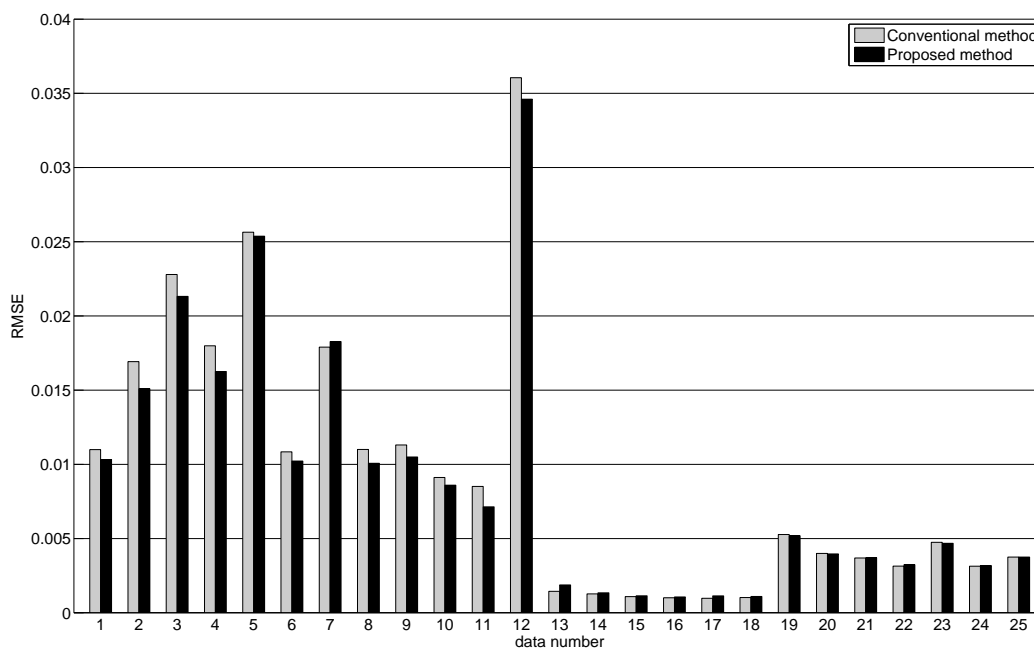
(b) RMSE Subset 2

Figure 5.2: RMSE relative to body coil reference image. x axis is the sequence of all MR data. The orders are SS, SSv and radial. y axis is the RMSE value.
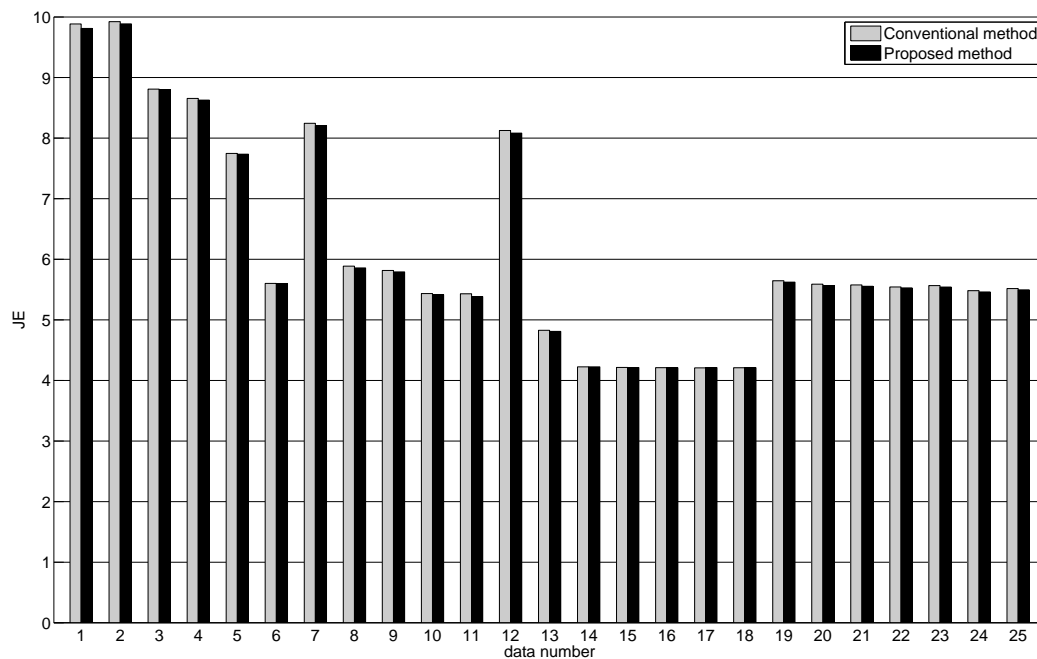
(a) NMI Subset 1

(b) NMI Subset 2

Figure 5.3: Normalized mutual information relative to body coil reference image. x axis is the sequence of all MR data.

(a) JE Subset 1
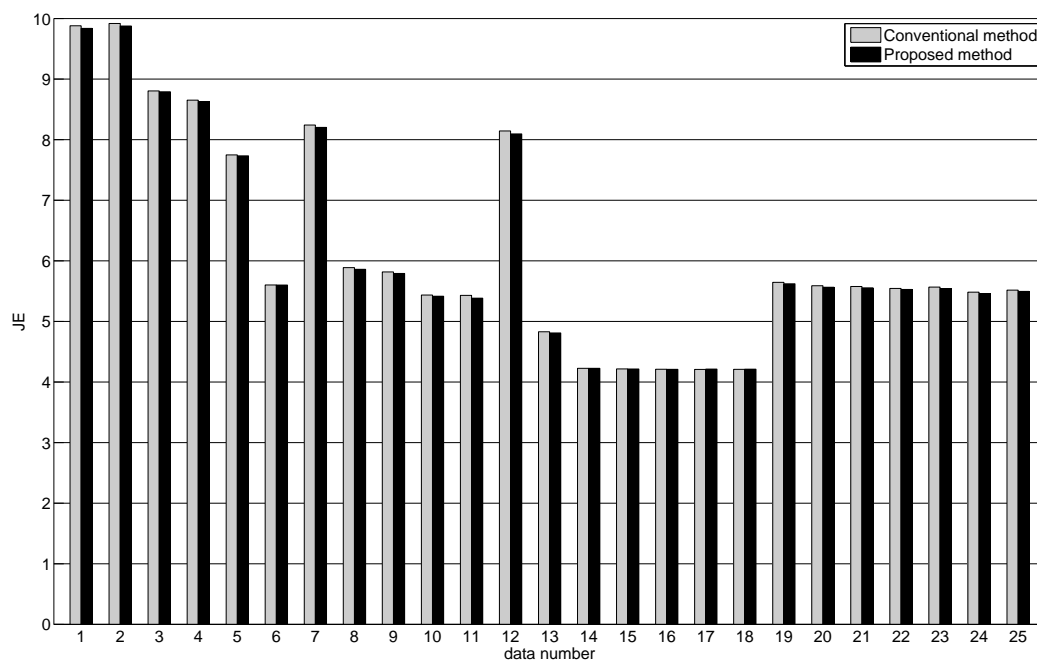
(b) JE Subset 2

Figure 5.4: Joint entropy relative to body coil reference image. x axis is the sequence of all MR data.
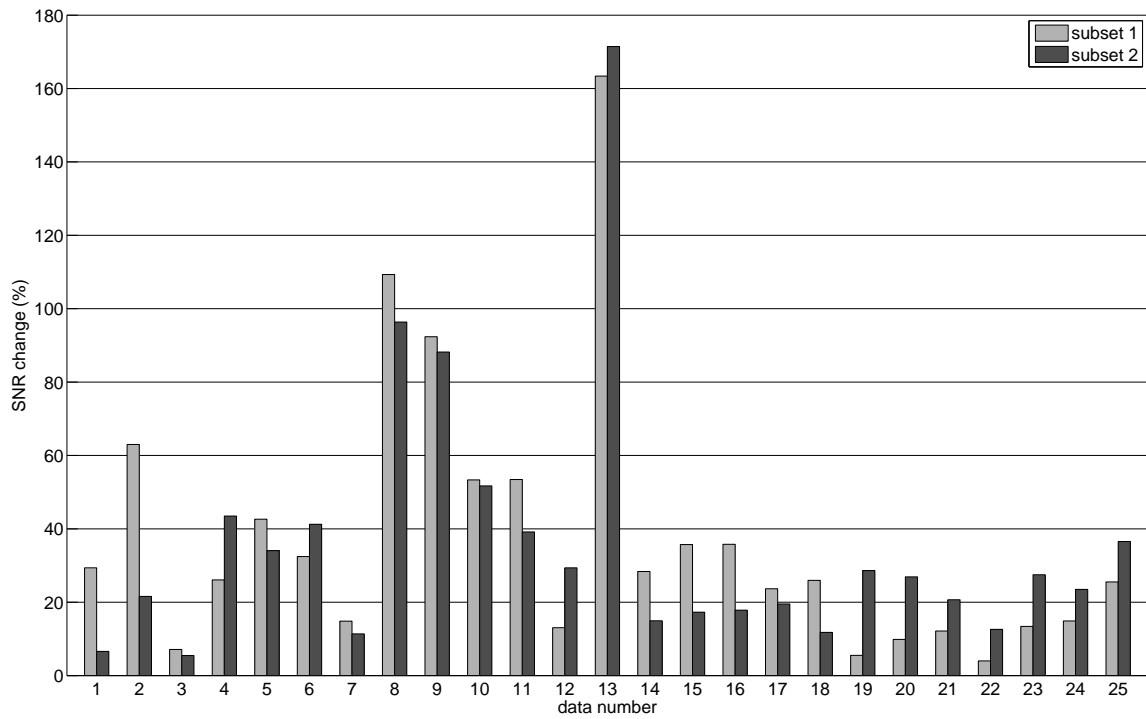
Figure 5.5: ROI SNR. y axis is the percentage of ROI SNR change of proposed method over conventional method. Positive values means higher SNR in those ROIs.

(a) Data SS 5 signal and noise ROI

(b) Data SSv 3 signal and noise ROI

(c) Data rad 3 signal ROI

(d) Data rad 3 noise ROI

Figure 5.6: The white square in the images denote the ROI definition. It is a noise ROI if it is in the empty region, or a signal ROI if it is in a high intensity region.

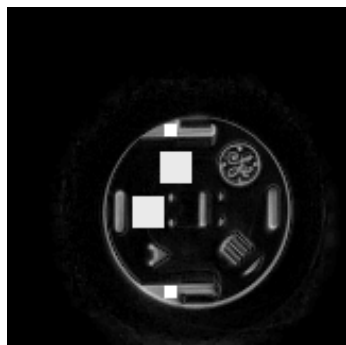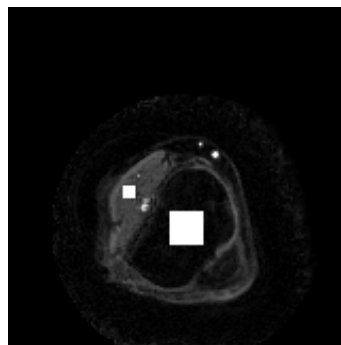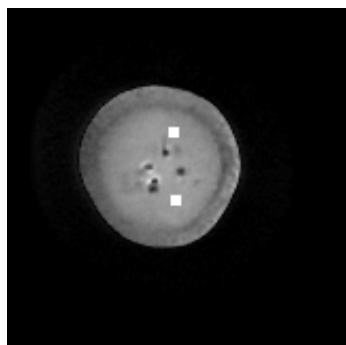Figure 5.7: Change of SNR calculated from two data. y axis is the percentage of SNR change of proposed method over conventional method. Positive values denotes higher SNR.

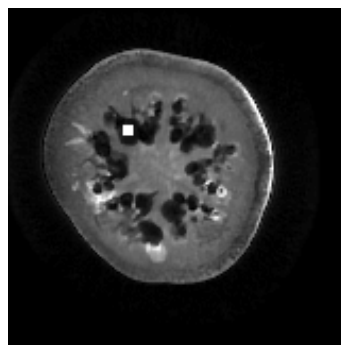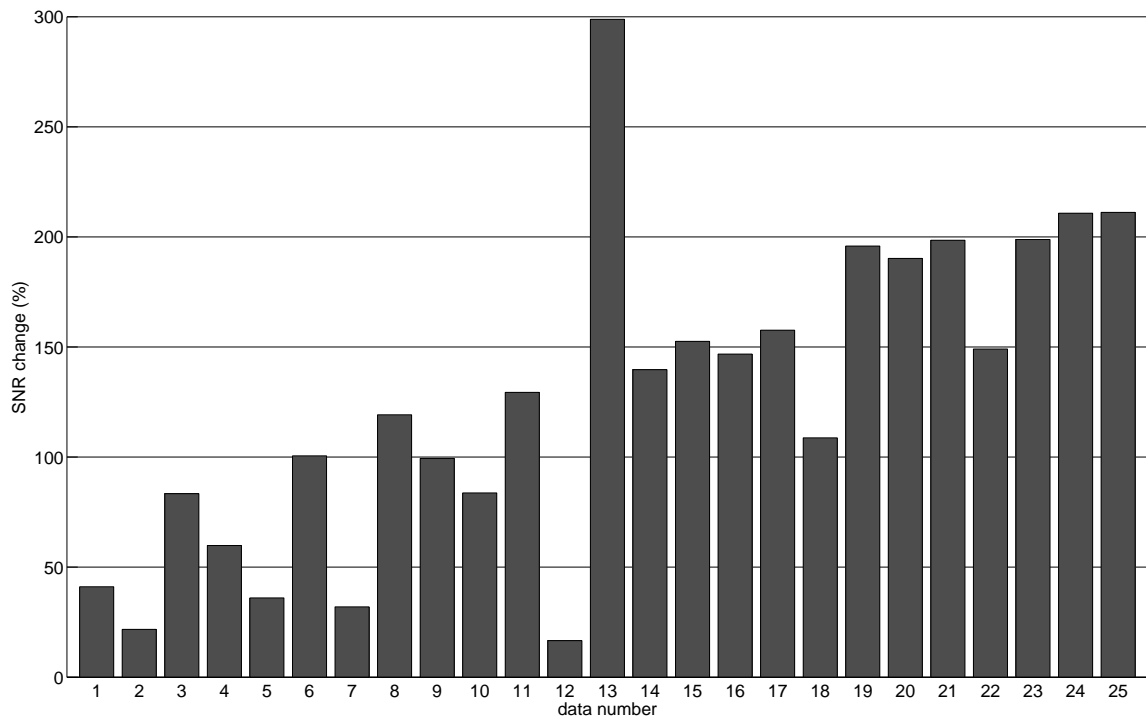shown in figure 5.8. Background is defined as those voxels inside of FOV mask but outside of the manually calculate image mask. Noise mean is represented by the bars. Noise standard deviation is represented by the error bar. Note that the object support coefficient calculated using the step-ration method does not completely set the background to 0 to reduce the impact on foreground image quality. The figures show that the proposed method reduced background noise mean and standard deviation in all data.

The interpolation coefficient is stored in sparse matrix format. The size depends on the number of k-space samples and interpolation kernel window length. A 50% compression results in savings of half the size. The reconstruction computation time is impacted by the image size, oversampling ratio, interpolation coefficients, and penalty term evaluation. For the 3D radial data with 192 point on each dimension, for example, the per iteration time in Matlab for conventionsl method using 2x grid and no coefficient compression is about 106 seconds. Using oversampling ratio of 1.125 and 50% coefficient compression, the per iteration time reduces to about 33 seconds. The Matlab code is not fully optimized. So the time here serves for referece purpose only. But it clearly shows that in each iteration the computation is reduced. Note that the proposed method requires more iterations and also extra steps for penalty coefficient calculation.
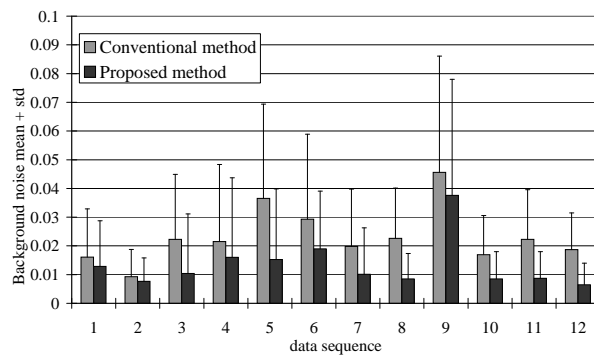
(a) SS and SSv subset 1
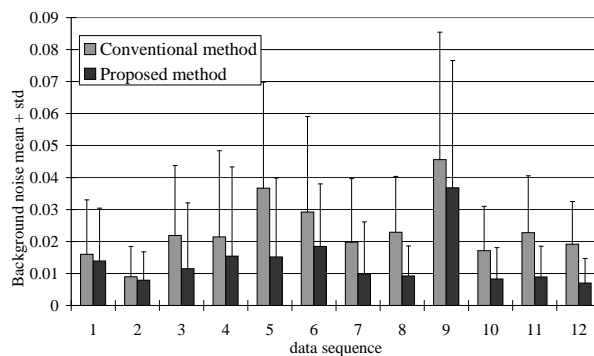
(b) SS and SSv subset 2
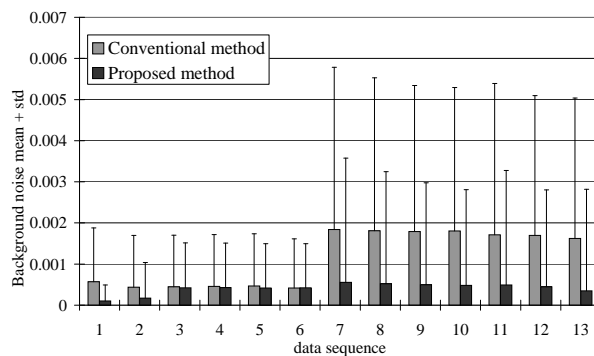
(c) Radial subset 1
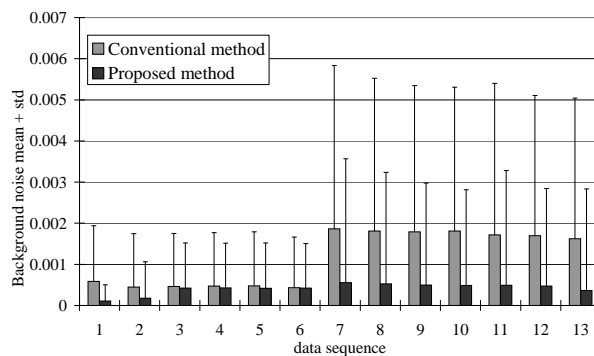
(d) Radial subset 2

Figure 5.8: Background noise mean and standard deviation.

5.4   Discussion

There is no widely accepted standard to evaluate reconstructed MRI images. Each image quality metrics has its own advantages and disadvantages. RMSE, NMI and JE all depends on the reference images. For the proposed method, image smoothing and background noise suppression operation is applied to achieve user desired effects. So the reconstruction is expected to be different from the image directly from MR scanner, which contains image noise and background noise. ROI SNR and two data SNR does not rely on reference images. But the values depends on the selection of ROI blocks. Background noise analysis depends on the definition of FOV mask and image mask. Using a combination of metrics to evaluate MRI data reconstruction is thus better than any single term.

The results in this chapter illustrate that the proposed method generates better quality reconstructions over conventional method in the sense of higher SNR and lower background noise, at reduced computer resource requirement, while still have comparable similarity measurement relative to the reference images.

CHAPTER 6
CONCLUSION

An iterative method for three dimensional non-Cartesian parallel MRI reconstruction was proposed in this work. The method was implemented based on SENSE and gridding following the evaluation of different reconstruction method including gridding, BURS and NUFFT. Solution was solved iteratively with edge preserving penalty and object support penalty to enhance image quality. These two penalty terms are compensate to each other. The former one smooths noise in image while preserves strong edges. The latter one reduces background noise but has no constraint on the foreground image. The combination of these two penalty terms improves the overall image quality. In both penalty terms, the regularization coefficient was calculated iteratively using a trust region based step-ratio method. Performance of the reconstruction using the calculated coefficients were close to the best RMSE.

The complexity of three dimensional reconstruction increases with the image size, number of samples and phased array coils. Larger data set require more computation power and computer memory and storage. On the other hand, redundant and less important information exist in the data. Using smaller gridding oversampling ratio with corresponding interpolation kernel parameters helped to alleviate the resource requirement. Compressing the pre-computed interpolation coefficient matrix by eliminating smaller coefficient also helped reducing the memory and storage requirement.

Each of the proposed method was validated using computer simulations. Two

numerical phantom images with added noise were generated. Three type of 3D non-Cartesian sampling patterns were used: stack of spiral (SS), stack of spiral with variable rotation (SSv) and radial pattern. Four and eight channel phased array coil configurations were simulated. Reduction factor values varied from 2 to 8. Comparison of the reconstructed image with the noise free numeric phantom in the sense of RMSE was performed. Results show that the edge preserving penalty enhances image quality with reduced image RMSE. Object support penalty reduces background noise without affecting foreground image quality. Using smaller oversampling ratio and compressing interpolation coefficient matrix have different impact on different sampling patterns. For smaller data such as the spiral sampling patterns (SS, SSV), relatively larger RMSEs occurred. For larger data using radial patterns, the impact on RMSE was very small. In some data the RMSE was even slightly reduced. Oversampling ratio of 1.125 was chosen for radial data.

The proposed method was applied on 25 three dimensional MR data from a GE MR scanner. A four channel phased array coil was used for data acquisition. All three sampling patterns were used. A variety of object were imaged: plastic phantom, fruit, and *in vivo* images from human volunteers. Edge preserving penalty, object support penalty and interpolation coefficient compression were applied on all data reconstruction. Smaller oversampling ratio was used for radial pattern data only.

Six image quality metrics were used to evaluate the performance of the proposed method: RMSE, NMI, JE, ROI SNR, two data SNR, and background noise. The first three metrics evaluate image quality relative to a reference image. A separate

full resolution body coil scan with the same type of non-Cartesian sampling pattern was used as the reference, which is an approximation to the true image. Manually calculated image mask was used to focus only on the errors of the image, not the background. The two SNR metrics measure SNR from the reconstructed images without references. ROIs were manually defined on each image data set and used to calculate SNR. The higher the SNR, the better the image quality. Background noise metric measures noise statistics from the background outside of the manually calculated image mask. For the 25 MR data, reconstructions from the proposed method were shown to have higher image SNR, less background noise, comparable similarity to reference image, at reduced resource requirement. The penalty coefficients calculated using the step-ratio method were validated for improved image quality.

The proposed method can be applied to other type of parallel MRI sampling patterns on different number of phased array coils. The impact of smaller oversampling ratio and interpolation coefficient matrix compression need to be re-evaluated for each application. Edge preserving penalty and object support penalty were demonstrated to enhance reconstruction quality on different applications with the calculated penalty coefficients. The trust region based step-ratio method for penalty coefficient calculation can be applied with other penalties.

REFERENCES

[1] Z.-P. Liang and P. C. Lantebur, *Principles of Magnetic Resonance Imaging - A Signal Processing Perspective.* New York, USA: Wiley-IEEE Press, October 1999.

[2] P. C. Lauterbur, "Image formation by induced local interactions: Examples employing nuclear magnetic resonance," *Nature*, vol. 242, pp. 190–191, 1973.

[3] J. Hennig, A. Nauerth, and H. Friedburg, "RARE imaging: A fast imaging method for clinical MR," *Magnetic Resonance in Medicine*, vol. 3, pp. 823–833, 1986.

[4] P. S. Melki, F. A. Jolesz, and R. V. Mulkern, "Partial RF echo planar imaging with the FAISE method. I. experimental and theoretical assessment of artifact," *Magnetic Resonance in Medicine*, vol. 26, pp. 328–341, 1992.

[5] P. S. Melki, F. A. Jolesz, and R. V. Mulkern, "Partial RF echo planar imaging with the FAISE method. II. contrast equivalencce with spin-echo sequences," *Magnetic Resonance in Medicine*, vol. 26, pp. 342–354, 1992.

[6] A. Haase, J. Frahm, D. Matthaei, W. Hänicke, and K.-D. Merboldt, " FLASH imaging: Rapid NMR imaging using low flip-angle pulses," *Journal of Magnetic Resonance*, vol. 67, pp. 258–266, 1986.

[7] P. Mansfield, "Multi-planar image formation using NMR spin echoes," *Journal of Physics*, vol. C10, pp. L55–L58, 1977.

[8] I. Pykett and R. Rzedzian, "Instant images of the body by magnetic resonance," *Magnetic Resonance in Medicine*, vol. 5, pp. 563–571, 1987.

[9] C. Ahn, J. Kim, and Z. Cho., "High-speed spiral-scan echo planar NMR imaging," *IEEE transactions on Medical Imaging*, vol. MI-5, pp. 2–7, 1986.

[10] C. Meyer, B. Hu, D. Nishimura, and A. Macovski, "Fast spiral coronary artery imaging," *Magnetic Resonance in Medicine*, vol. 28, pp. 202–213, 1992.

[11] G. H. Glover, "Simple analytic spiral k-space algorithm," *Magnetic Resonance in Medicine*, vol. 42, pp. 412–415, Aug 1999.

[12] D. K. Sodickson and W. J. Manning, "Simultaneous acquisition of spatial harmonics (SMASH): fast imaging with radiofrequency coil arrays," *Magnetic Resonance in Medicine*, vol. 38, pp. 591–603, 1997.

[13] K. P. Pruessmann, M. Weiger, M. B. Scheidegger, and P. Boesiger, "SENSE: Sensitivity encoding for fast MRI," *Magnetic Resonance in Medicine*, vol. 42, pp. 952 – 962, 1999.

[14] J. O'Sullivan, "A fast sinc function gridding algorithm for Fourier inversion in computer tomography," *IEEE transactions on Medical Imaging*, vol. 4, pp. 200–207, 1985.

[15] J. Jackson, C. Meyer, D. Nishimura, and A. Macovski, "Selection of a convolution function for Fourier inversion using gridding," *IEEE transactions on Medical Imaging*, vol. 10, pp. 473–478, 1991.

[16] A. Dutt and V. Rokhlin, "Fast Fourier trasforms for nonequispaced data," *SIAM Journal on Scientific Computing*, vol. 14, pp. 1368–1393, November 1993.

[17] A. Dutt and V. Rokhlin, "Fast Fourier transforms for nonequispaced data. II," *Appl. Comput. Harmon. Anal.*, vol. 2, no. 1, pp. 85–100, 1995.

[18] N. Nguyen and Q. H. Liu, "The regular Fourier matrices and nonuniform fast Fourier transforms," *SIAM Journal on Scientific Computing*, vol. 21, no. 1, pp. 283–293, 1999.

[19] J. Fessler and B. Sutton, "Nonuniform fast Fourier transforms using min-max interpolation," *IEEE Transactions on Signal Processing*, vol. 51, no. 2, pp. 560–574, 2003.

[20] D. Rosenfeld, "An optimal and efficient new gridding algorithm using singular value decomposition," *Magnetic Resonance in Medicine*, vol. 40, pp. 14–23, 1998.

[21] D. Rosenfeld, "New approach to gridding using regularization and estimation theory," *Magnetic Resonance in Medicine*, vol. 48, pp. 193–202, 2002.

[22] J. Pipe and P. Menon, "Sampling density compensation in MRI: Rationale and an iterative numerical solution," *Magnetic Resonance in Medicine*, vol. 41, no. 1, pp. 179–186, 1999.

[23] R. Hoge, R. Kwan, and G. Pike, "Density compensation functions for spiral MRI," *Magnetic Resonance in Medicine*, vol. 38, pp. 117–128, 1997.

[24] V. Rasche, R. Proska, R. Sinkus, P. Boernert, and H. Eggers, "Resampling of data between arbitrary grids using convolution interpolation," *IEEE Transactions on Image Processing*, vol. 18, no. 5, pp. 385–392, 1999.

[25] H. Moriguchi, M. Wendt, and J. L. Duerk, "Applying the uniform resampling (URS) algorithm to a Lissajous trajectory: Fast image reconstruction with optimal gridding," *Magnetic Resonance in Medicine*, vol. 44, pp. 766–781, 2000.

[26] P. Beatty, D. Nishimura, and J. Pauly, "Rapid gridding reconstruction with a minimal oversampling ratio," *IEEE Transactions on Medical Imaging*, vol. 24, pp. 799–808, June 2005.

[27] Y. M. Kadah, "New solution to the gridding problem," in *Proceedings of the SPIE Vol. 4684, Medical Imaging 2002: Image Processing*, 2002.

[28] A. V. Oppenheim and R. W. Schafer, *Discrete Time Signal Processing*. Englewood Cliffs, NJ: Prentice Hall, 1989.

[29] G. Golub and C. Van Loan, *Matrix Computations*. Baltimore, MD: Johns Hopkins University Press, 1996.

[30] X. Jiang and D. Thedens, "New iterative gridding algorithm using conjugate gradient method," in *Proceedings of the SPIE Medical Imaging 2004: Image Processing*, vol. 5370, pp. 1852–1861, 2004.

[31] H. Sedarat and D. Nishimura, "On the optimality of the gridding reconstruction algorithm," *IEEE transactions on Medical Imaging*, vol. 19, pp. 306 –317, 2000.

[32] A. N. Tikhonov and V. Y. Arsenin, *Solutions of ill-posed problems*. Washington, DC: W.H.Winston and Sons, 1977.

[33] M. Bertero and P. Boccacci, *Introduction to inverse problems in imaging*. Bristol: Institute of Physics Publishing, 1998.

[34] H. Moriguchi and J. L. Duerk, "Modified block uniform resampling (BURS) algorithm using truncated singular value decomposition: Fast accurate gridding with noise and artifact reduction," *Magnetic Resonance in Medicine*, vol. 46, pp. 1189–1201, 2001.

[35] G. Sarty, R. Bennett, and R. Cox, "Direct reconstruction of non-Cartesian k-space data using a non-uniform fast Fourier transform," *Magnetic Resonance in Medicine*, vol. 45, pp. 908–915, 2001.

[36] G. Beylkin, "On the fast Fourier transform of functions with singularities," *Appl. Comput. Harmon. Anal.*, vol. 2, no. 4, pp. 363–381, 1995.

[37] C. Anderson and M. Dahleh, "Rapid computation of the discrete Fourier transform," *SIAM Journal on Scientific Computing*, vol. 17, pp. 913–919, 1996.

[38] L. Sha, H. Guo, and A. Song, "An improved gridding method for spiral MRI using nonuniform fast fourier transform," *Journal of Magnetic Resonance*, vol. 162, pp. 250–258, June 2003.

[39] J. Shewchuk, *An Introduction to the Conjugate Gradient Method Without the Agonizing Pain.* School of Computer Science, Carnegie Mellon University, Pittsburgh, PA, USA: Internal Report, Aug 1994.

[40] B. Sutton, D. Noll, and J. Fessler, "Fast, iterative image reconstruction for MRI in the presence of field inhomogeneities," *IEEE Transactions on Medical Imaging*, vol. 22, pp. 178 – 188, Feb 2003.

[41] P. Jakob, M. Griswold, R. Edelman, and D. Sodickson, "AUTO-SMASH: a self-calibrating technique for SMASH imaging. SiMultaneous Acquisition of Spatial Harmonics," *MAGMA*, vol. 7, pp. 42–54, November 1998.

[42] R. Heidemann, M. Griswold, A. Haase, and P. Jakob, "VD-AUTO-SMASH imaging," *IEEE transactions on Medical Imaging*, vol. 45, pp. 1066–1074, June 2001.

[43] M. Griswold, P. Jakob, R. Heidemann, M. Nittka, V. Jellus, J. Wang, B. Kiefer, and A. Haase, "Generalized autocalibrating partially parallel acquisitions (grappa)," *Magnetic Resonance in Medicine*, vol. 47, pp. 1202–1210, June 2002.

[44] K. Heberlein, Y. M. Kadah, and X. Hu, "Segmented spiral parallel imaging using GRAPPA," in *Proc. ISMRM 12th Annual Meeting*, (Kyoto, Japan), p. 328, May 2004.

[45] K. P. Pruessmann, M. Weiger, P. Börnert, and P. Boesiger, "Advances in sensitivity encoding with arbitrary k-space trajectories," *Magnetic Resonance in Medicine*, vol. 46, no. 4, pp. 638–651, 2001.

[46] M. Weiger, K. P. Pruessmann, and P. Boesiger, "2D SENSE for faster 3D imaging," *MAGMA*, vol. 8, no. 1, p. 177, 1999.

[47] D. O. Walsh, A. F. Gmitro, and M. W. Marcellin, "Adaptive reconstruction of phased array MR imagery," *Magnetic Resonance in Medicine*, vol. 43, pp. 682–690, May 2000.

[48] Z.-P. Liang, R. Bammer, J. Ji, N. Pelc, and G. Glover, "Improved image reconstruction from sensitivity-encoded data by wavelet denoising and Tikhonov regularization," in *Proc. 2002 IEEE International Symposium on Biomedical Imaging*, (Washington DC), pp. 493–496, July 2002.

[49] J. Wang, T. Kluge, M. Nittka, V. Jellus, B. Kuehn, and B. Kiefer, "Parallel acquisition techniques with modified sense reconstruction: msense," in *Proceedings of the First Wurzburg Workshop on Parallel Imaging: Basics and Clinical Applications*, p. 92, 2001.

[50] B. Zhang, K. Zhong, J. Wang, and Y. Zhuo, "LS_NUFFT Based SENSE Reconstruction for Polar k-Space Trajectory," in *Proc. ISMRM 12th Scientific Meeting and Exhibition*, (Kyoto, Japan), p. 2415, May 2004.

[51] A. A. Samsonov, E. G. Kholmovski, D. L. Parker, and C. R. Johnson, "POC-SENSE: POCS-based reconstruction for sensitivity encoded magnetic resonance imaging," *Magnetic Resonance in Medicine*, vol. 52, pp. 1397–1406, December 2004.

[52] B. Madore and N. Pelc, "SMASH and SENSE: experimental and numerical comparisons," *Magnetic Resonance in Medicine*, vol. 45, pp. 1103–1111, 2001.

[53] M. Blaimer, F. Breuer, M. Mueller, R. M. Heidemann, M. A. Griswold, and P. M. Jakob, "Smash, sense, pils, grappa: How to choose the optimal method," *Topics in Magnetic Resonance Imaging*, vol. 15, pp. 223–236, August 2004.

[54] E. N. Yeh, C. A. McKenzie, M. A. Ohliger, and D. K. Sodickson, "3parallel magnetic resonance imaging with adaptive radius in k-space (pars): Constrained image reconstruction using k-space locality in radiofrequency coil encoded data," *Magnetic Resonance in Medicine*, vol. 53, pp. 1383–1392, June 2005.

[55] A. A. Samsonov and A. S. F. Walter F. Block, Arjun Arunachalam, "Advances in locally constrained k-space-based parallel mri," *Magnetic Resonance in Medicine*, vol. 55, pp. 431–438, February 2006.

[56] A. K. Jain, *Fundamentals of Digital Image Processing*. Englewood Cliffs, NJ: Prentice Hall, 1989. p. 439.

[57] D. J. Griffiths, *Introduction to Electrodynamics*. Prentice Hall, 3rd ed., 1998.

[58] S. Hellstrandh and D. Stenvall., "Implementation and evaluation of sense in 3d mri," Master's thesis, Linkopings universitet, Linkoping, Sweden, 2003.

[59] A. V. Barger, W. F. Block, Y. Toropov, T. M. Grist, and C. A. Mistretta, "Time-resolved contrast-enhanced imaging with isotropic resolution and broad coverage using an undersampled 3D projection trajectory," *Magnetic Resonance in Medicine*, vol. 48, pp. 297–305, August 2002.

[60] A. C. Kak and M. Slaney, *Principles of Computerized Tomographic Imaging*. SIAM, 2001.

[61] G. Demoment, "Image reconstruction and restoration: overview of common estimation structures and problems," *IEEE Transactions on Acoustics, Speech, and Signal Processing*, vol. 37, pp. 2024 – 2036, December 1989.

[62] P. Charbonnier, L. Blanc-Féraud, G. Aubert, and M. Barlaud, "Deterministic edge-preserving regularization in computed imaging," *IEEE Transactions on Image Processing*, vol. 6, pp. 298 – 311, Feb. 1997.

[63] N. Villain, Y. Goussard, J. Idier, and M. Allain, "Three-dimensional edge-preserving image enhancement for computed tomography," *IEEE transactions on Medical Imaging*, vol. 22, pp. 1275 – 1287, Oct. 2003.

[64] S. Geman and G. Geman, "Stochastic relaxation, Gibbs distributions and the Bayesian restoration of images," *IEEE Transactions on Pattern Analysis and Machine Intelligence*, vol. PAMI-6, pp. 721–741, June 1984.

[65] J. A. Fessler, "Penalized weighted least-squares image reconstruction for positron emission tomography," *IEEE transactions on Medical Imaging*, vol. 13, no. 2, pp. 290–300, 1994.

[66] D. Yu and J. Fessler, "Edge-preserving tomographic reconstruction with nonlocal regularization," *IEEE transactions on Medical Imaging*, vol. 21, pp. 159–73, February 2002.

[67] J. Idier, "Regularization tools and models in image and signal reconstruction," in *Third International Conference on Inverse Problems in Engineering*, June 1999.

[68] D. Geman and G. Reynolds, "Constrained restoration and the recovery of discontinuities," *IEEE Transactions on Pattern Analysis and Machine Intelligence*, vol. 14, pp. 367–383, March 1992.

[69] A. Raj, G. Singh, R. Zabih, B. Kressler, Y. Wang, N. Schuff, and M. Weiner, "Bayesian parallel imaging with edge-preserving priors," *Magnetic Resonance in Medicine*, vol. 57, no. 1, pp. 8–21, 2007.

[70] M. Lustig and J. M. Pauly, "Spirit: Iterative self-consistent parallel imaging reconstruction from arbitrary k-space," *Magnetic Resonance in Medicine*, vol. 64, pp. 457–471, 2010.

[71] J. Petr, J. Kybic, M. Bock, S. Muller, and V. Hlavac, "Parallel image reconstruction using B-spline approximation (PROBER)," *Magnetic Resonance in Medicine*, vol. 58, no. 3, pp. 582–591, 2007.

[72] M. R. Celis, J. E. Dennis, and R. A. Tapia, *A trust region strategy for nonlinear equality constrained optimization.* SIAM, 1985.

[73] M. Buehrer, K. P. Pruessmann, P. Boesiger, and S. Kozerke, "Array compression for mri with large coil arrays," *Magnetic Resonance in Medicine*, vol. 57, no. 6, pp. 1131–1139, 2007.

[74] L. Ying, B. Liu, M. C. Steckner, G. Wu, M. Wu, and S.-J. Li, "A statistical approach to sense regularization with arbitrary ¡i¿k¡/i¿-space trajectories," *Magnetic Resonance in Medicine*, vol. 60, no. 2, pp. 414–421, 2008.

[75] K. T. Block, M. Uecker, and J. Frahm, "Undersampled radial mri with multiple coils. iterative image reconstruction using a total variation constraint," *Magnetic Resonance in Medicine*, vol. 57, no. 6, pp. 1086–1098, 2007.

[76] W. E. Kyriakos, L. P. Panych, D. F. Kacher, C.-F. Westin, S. M. Bao, R. V. Mulkern, and F. A. Jolesz, "Sensitivity profiles from an array of coils for encoding and reconstruction in parallel (SPACE RIP)," *Magnetic Resonance in Medicine*, vol. 44, pp. 301–308, 2000.

[77] C. A. McKenzie, E. N. Yeh, M. A. Ohliger, M. D. Price, and D. K. Sodickson, "Self-calibrating parallel imaging with automatic coil sensitivity extraction," *Magnetic Resonance in Medicine*, vol. 47, pp. 529–538, March 2002.

[78] M. A. Griswold, S. Kannengiesser, R. M. Heidemann, J. Wang, and P. M. Jakob, "Field-of-view limitations in parallel imaging," *Magnetic Resonance in Medicine*, vol. 52, no. 5, pp. 1118–1126, 2004.

[79] F.-H. Lin, K. K. Kwong, J. W. Belliveau, and L. L. Wald, "Parallel imaging reconstruction using automatic regularization," *Magnetic Resonance in Medicine*, vol. 51, pp. 559–567, March 2004.

[80] Y. Qian, Z. Zhang, V. A. Stenger, and Y. Wang, "Self-calibrated spiral SENSE," *Magnetic Resonance in Medicine*, vol. 52, pp. 688–692, 2004.

[81] C. Liu, M. E. Moseley, and R. Bammer, "Simultaneous phase correction and sense reconstruction for navigated multi-shot dwi with non-cartesian k-space sampling," *Magnetic Resonance in Medicine*, vol. 54, pp. 1412–1422, December 2005.

[82] H. Cheng and F. Huang, "Magnetic resonance imaging image intensity correction with extrapolation and adaptive smoothing," *Magnetic Resonance in Medicine*, vol. 55, pp. 959–966, April 2006.

[83] F. A. Breuer, M. Blaimer, M. F. Mueller, N. Seiberlich, R. M. Heidemann, M. A. Griswold, and P. M. Jakob, "Controlled aliasing in volumetric parallel imaging (2D CAIPIRINHA)," *Magnetic Resonance in Medicine*, vol. 55, pp. 549–556, March 2006.

[84] M. Buehrer, M. E. Huber, F. Wiesinger, P. Boesiger, and S. Kozerke, "Coil setup optimization for 2D-SENSE whole-heart coronary imaging," *Magnetic Resonance in Medicine*, vol. 55, pp. 460–464, February 2006.

[85] A. C. Brau, P. J. Beatty, S. Skare, and R. Bammer, "Comparison of reconstruction accuracy and efficiency among autocalibrating data-driven parallel imaging methods," *Magnetic Resonance in Medicine*, vol. 59, no. 2, pp. 382–395, 2008.

[86] J. Sánchez-González, J. Tsao, U. Dydak, M. Desco, P. Boesiger, and K. P. Pruessmann, "Minimum-norm reconstruction for sensitivity-encoded magnetic resonance spectroscopic imaging," *Magnetic Resonance in Medicine*, vol. 55, pp. 287–295, February 2006.

[87] L. Ying and J. Sheng, "Joint image reconstruction and sensitivity estimation in SENSE (JSENSE)," *Magnetic Resonance in Medicine*, vol. 57, no. 6, pp. 1196–1202, 2007.

[88] F. Huang, Y. Li, S. Vijayakumar, S. Hertel, and G. R. Duensing, "High-pass grappa: An image support reduction technique for improved partially parallel imaging," *Magnetic Resonance in Medicine*, vol. 59, no. 3, pp. 642–649, 2008.

[89] Z. Xiao, W. S. Hoge, R. Mulkern, L. Zhao, G. Hu, and W. E. Kyriakos, "Comparison of parallel mri reconstruction methods for accelerated 3d fast spin-echo imaging," *Magnetic Resonance in Medicine*, vol. 60, no. 3, pp. 650–660, 2008.

[90] M. Schmitt, A. Potthast, D. E. Sosnovik, J. R. Polimeni, G. C. Wiggins, C. Triantafyllou, and L. L. Wald, "A 128-channel receive-only cardiac coil for highly accelerated cardiac mri at 3 tesla," *Magnetic Resonance in Medicine*, vol. 59, no. 6, pp. 1431–1439, 2008.

[91] M. J. Firbank, A. Coulthard, R. M. Harrison, and E. D. Williams, "A comparison of two methods for measuring the signal to noise ratio on mr images," *Physics in Medicine and Biology*, vol. 44, no. 12, pp. N261–N264, 1999.

[92] S. B. Reeder, B. J. Wintersperger, O. Dietrich, T. Lanz, A. Greiser, M. F. Reiser, G. M. Glazer, and S. O. Schoenberg, "Practical approaches to the evaluation of signal-to-noise ratio performance with parallel imaging: Application with cardiac imaging and a 32-channel cardiac coil," *Magnetic Resonance in Medicine*, vol. 54, no. 3, pp. 748–754, 2005.

[93] F. Odille, N. Cindea, D. Mandry, C. Pasquier, Pierre-Andr?Vuissoz, and J. Felblinger, "Generalized mri reconstruction including elastic physiological motion and coil sensitivity encoding," *Magnetic Resonance in Medicine*, vol. 59, no. 6, pp. 1401–1411, 2008.

[94] D. J. Larkman, P. G. Batchelor, D. Atkinson, D. Rueckert, and J. V. Hajnal, "Beyond the g-factor limit in sensitivity encoding using joint histogram entropy," *Magnetic Resonance in Medicine*, vol. 55, no. 1, pp. 153–160, 2006.

[95] M. Honal, S. Bauer, U. Ludwig, and J. Leupold, "Increasing efficiency of parallel imaging for 2d multislice acquisitions," *Magnetic Resonance in Medicine*, vol. 61, pp. 1459–1470, 2009.

[96] F. A. Breuer, M. Blaimer, R. M. Heidemann, M. F. Mueller, M. A. Griswold, and P. M. Jakob, "Controlled aliasing in parallel imaging results in higher acceleration (caipirinha) for multi-slice imaging," *Magnetic Resonance in Medicine*, vol. 53, no. 3, pp. 684–691, 2005.